

# Quantum Master Equation Approach to Nanoelectronics

Zur Erlangung des akademischen Grades eines  
DOKTORS DER NATURWISSENSCHAFTEN  
von der Fakultät für Physik des  
Karlsruher Instituts für Technologie (KIT)

genehmigte  
DISSERTATION  
von

Christian Karlewski

aus Mainz

Datum der mündlichen Prüfung: 29.04.2016  
Erstgutachter: Prof. Dr. Gerd Schön  
Zweitgutachter: Prof. Dr. Alexander Shnirman



The research work covered by this thesis was done between March 2013 and March 2016 at the *Institut für Theoretische Festkörperphysik* and the *Institute of Nanotechnology* at the *Karlsruhe Institute of Technology*. It contains the major part of my investigations as a PhD student and consists of three different topics which are related by their physics:

- The dynamics of single magnetic atoms on metallic surfaces. In particular, the theoretical investigation of holmium atoms on a platinum surface which showed exceptional long lifetimes in experimental measurements.
- Lasing produced in multi-level double quantum dot systems which are coupled to electronic leads and a phonon bath. The multi-level structure yields several possible resonance conditions with qualitative different transport characteristics.
- Properties of the quantum master equation. An expansion of the quantum master equation in the coupling strength and in the correlation time of the environment is derived. Using this method, we analyze the connection and justification of the well-known Born and Markov approximations.



# Acknowledgment

First of all, I want to thank Gerd Schön who agreed to supervise my external Master thesis and offered me the opportunity to continue my work as PhD student in his group. In addition, he helped me in all my scientific studies, intensively discussed with me various upcoming problems and is supporting my further career steps. I really appreciate the time working in his group.

Second, I want to thank Alexander Shnirman for being the second referee of this thesis.

Michael Marthaler was a great assistance during my Master thesis and also at the beginning of my PhD. I would like to thank him for his support.

Andreas Poenike is responsible for our IT-support in the group. He saved my work once when I thought I had lost everything and I will always be thankful, in addition to the great work he does everyday.

Special thanks go to the whole TFP working group. The friendly and funny work atmosphere lead to four amazing years in Karlsruhe, especially the non-university related projects. But additionally, the scientific help given to me and the numerous interesting discussions were important for the completion of this thesis. In particular, I want to thank Iris Schwenk, Daniel Mendler, Jan Reiner, Sebastian Zanker, Lingzhen Guo and the former members Andreas Heimes and Panagiotis Kotetes.

I also would like to thank Christian Robach for producing the beautiful cover picture and Fig. 3.3 which was in a similar way used in paper [III]. I received great appreciation which I hereby want to pass on to him.

But most of all I want to thank my family. They give me the emotional support and are my contact point for any problem. My parents, Rita and Thomas, supported me throughout my whole life, enabled my studies and taught me scientific reasoning since my birth. But the most important person in my life is my (in the near future) wife Marit who stands at my side at all times and is the basis for everything I am.

I thank the Nature Publishing Group, the American Physical Society and Elsevier for the permission to include different figures in my thesis. The specific permissions and copyrights are mentioned in the caption of each figure.

# List of Publications

- I. T. Miyamachi, T. Schuh, T. Märkl, C. Bresch, T. Balashov, A. Stöhr, C. Karlewski, S. André, M. Marthaler, M. Hoffmann, M. Geilhufe, S. Ostanin, W. Hergert, I. Mertig, G. Schön, A. Ernst, and W. Wulfhekel, *Stabilizing the magnetic moment of single holmium atoms by symmetry*, Nature **503**, 242 (2013).
- II. C. Karlewski and M. Marthaler, *Time-local master equation connecting the Born and Markov approximations*, Phys. Rev. B **90**, 104302 (2014).
- III. C. Karlewski, M. Marthaler, T. Märkl, T. Balashov, W. Wulfhekel, and G. Schön, *Magnetic adatoms as memory bits: A quantum master equation analysis*, Phys. Rev. B **91**, 245430 (2015).
- IV. J. Jin, C. Karlewski, and M. Marthaler, *Non-Markovian correlation functions for open quantum systems*, ArXiv e-prints (2015).
- V. C. Karlewski, A. Heimes, and G. Schön, *Lasing and transport in a multi-level double quantum dot system coupled to a microwave oscillator*, Phys. Rev. B **93**, 045314 (2016).





# Contents

<b>Abstract</b>	<b>I</b>
<b>Acknowledgment</b>	<b>III</b>
<b>List of Publications</b>	<b>V</b>
<b>1 Introduction</b>	<b>1</b>
<b>2 Theoretical Background</b>	<b>13</b>
2.1 Quantum Master Equation . . . . .	14
2.2 Time-Convolutionless Method . . . . .	17
2.3 Diagrammatic Expansion of the QME . . . . .	20
2.4 Environment-Induced Superselection . . . . .	25
<b>3 Single Magnetic Adatoms</b>	<b>29</b>
3.1 Stevens Operator Method . . . . .	30
3.2 Coupling of Adatoms to Electrons . . . . .	35
3.3 Holmium on Platinum (111) . . . . .	40
3.3.1 Pointer States of Ho on Pt(111) . . . . .	47
3.4 Relaxation Time $T_1$ . . . . .	54
3.4.1 Current through the Tip . . . . .	55
3.4.2 Voltage Dependency . . . . .	57
3.4.3 Experimental Issues . . . . .	62
3.5 Deviations from the Ideal Situation . . . . .	66
3.5.1 Scattering of Bulk Electrons . . . . .	66
3.5.2 Breaking the $C_{3v}$ -Symmetry . . . . .	68

3.5.3	Noise in the Circuit . . . . .	70
3.5.4	Magnetic Field Dependency . . . . .	73
3.5.5	Alternative Steven's Parameters . . . . .	75
3.6	Decoherence Time $T_2$ . . . . .	78
3.7	Initialization . . . . .	80
<b>4</b>	<b>Double Quantum Dots</b>	<b>85</b>
4.1	The DQD Hamiltonian and the QME . . . . .	86
4.1.1	DQD Coupled to a Microwave Oscillator . . . . .	86
4.1.2	Coupling to a Phonon Bath . . . . .	93
4.2	Lasing in the Multi-Level System . . . . .	95
4.2.1	Overview of Different Lasing Situations . . . . .	95
4.2.2	Detailed Analysis of the Cascade Lasing . . . . .	101
<b>5</b>	<b>Master Equation</b>	<b>107</b>
5.1	Expansion of the QME . . . . .	108
5.1.1	Time Local QME and Diagrammatic Expansion	108
5.1.2	Combined Expansion . . . . .	112
5.2	Spin-Boson Model . . . . .	115
5.2.1	Evaluation of the Self-Energy . . . . .	119
5.2.2	Comparing Different Orders . . . . .	124
5.3	Initial State Problem . . . . .	130
5.4	Two-Time Correlator . . . . .	132
<b>6</b>	<b>Conclusion</b>	<b>139</b>
<b>A</b>	<b>Appendix</b>	<b>145</b>
A.1	Implementation of the QME . . . . .	145
A.2	Higher Order Diagrams in the Spin-Boson Model . . . . .	150
	<b>References</b>	<b>153</b>

# 1 Chapter

---

## Introduction

The ongoing trend in miniaturization of electronics yields new perspectives but also challenges. The famous Moor's law stating that the number of transistors doubles roughly every 18 months is one popular example [1]. Computer performance is increasing rapidly and has led not only to a technological, but to a social revolution. Every modern smartphone has more computing power than the Apollo Guidance Computer used for the moon landing in 1969 [2]. Computer technology is highly integrated in our every day life and we often only recognize it when it is not working. Thus, the development of faster, smaller, more efficient and more reliable devices is interesting from an economic as well as a sociological point of view. Today, the smallest on-chip structures produced (Status: January 2016, announced by IBM [3]) are 7 nm in size, i.e., around 70 atoms in width. In this regime, quantum mechanical effects could begin to change the properties of the classical electronic circuits and have to

be taken into account in a growing number of circumstances. For example, if the insulating barrier between the conductors is too weak, quantum tunneling becomes important. Then, a proper usage of the device as expected from classical physics can no longer be guaranteed [4].

The shrinking of electronic devices goes hand in hand with the miniaturization of magnetic storage devices. These devices measure the magnetic moment of an area or domain pointing along an easy axis. On current hard disks (Status: January 2016) an area density of approximately  $150 \text{ Gbit/cm}^2$  can be achieved, which implies that around  $10^7$  surface atoms are needed to store one bit of information [5]. The question arises: What is the minimum number of atoms required for one memory bit? The main problem of the shrinking process is the decreasing magnetic anisotropy of the cluster of atoms as fewer atoms are used. The magnetic anisotropy is the tendency of the magnetic moment to align with a specific axis, thus the lower the magnetic anisotropy the weaker the stability. In parallel with the miniaturization, the magnetic moment decreases and thermal fluctuations become pronounced. The bit flips stochastically between its two states and the lifetime becomes too short to use the bit as a memory.

The field of laser physics is another example creating strong interest in producing tiny on-chip structures. In 1917, Albert Einstein explained theoretically the stimulated emission of photons [6], which was used in 1960 by Theodore H. Maiman to build the first laser with a size of around one meter. The shrinking of the laser eventually leads to lasing of single-atoms strongly coupled to an optical cav-

---

ity [7]. This concept could directly be transferred to solid state systems with superconducting quantum mechanical bits (qubits) [8–10]. Because the produced photons have frequencies in the GHz regime, which corresponds to microwave wavelengths (1 mm to 300 mm), the device is occasionally called “maser” instead of laser. The superconducting qubits in this setting serve as artificial atoms with a well controlled, tunable level structure which can be coupled to microwave resonators [11–15]. Thus, they behave according to models developed in the field of quantum optics, i.e., for atoms coupled to photons in optical cavities, but with a higher control over the system properties.

As mentioned, miniaturization has several negative effects such as unwanted tunneling or instability of the systems. But miniaturization towards the regime of quantum mechanics also leads to completely new applications and devices. The single-electron transistor is one example. It has been developed as an accurate current standard and finds application in laboratories for high precision measurements [16–20]. The device consists of a metallic, semiconducting or superconducting island coupled to two electron reservoirs. By adjusting the properties of the island via applied gate voltages, single electron transport through the device can be controlled. The device exploits the property of quantum mechanical objects to tunnel through classically impenetrable barriers. Other important features of quantum mechanics are the superposition principle, the coherent time evolution, as well as the properties of entangled states. A state is called coherent when the quantum mechanical phases are well defined during the time evolution, i.e., they change during the time evolution only in a deterministic way. This situation is used in qubits which are the

basic elements for quantum computing. The entanglement of several qubits leads to maximal parallel computing and for certain problems to an exponential speedup compared to classical computations. The most famous examples are the Shor algorithm for the factorization of large numbers [21] and the Grover algorithm for searching unsorted arrays [22]. For magnetic devices, quantum mechanics can be an advantage as well. Already in 1988 the giant-magnetoresistant (GMR) effect was discovered by Grünberg and Fert [23]. They investigated a system of alternating ferromagnetic and non-magnetic layers with a few nanometer thickness. The GMR effect relies on the differing resistance perpendicular to the layers for parallel and anti-parallel orientations of the magnetization of the ferromagnets. This is caused by the spin of the electrons which forces the electrons to scatter different in the parallel or anti-parallel configurations. Therefore, the state of such a memory bit can be read out through a current measurement. We will later see that the same effect is used to read out and manipulate the state of single magnetic atoms. The discovery of the giant-magnetoresistant effect lead only 9 years later to the first hard disk built by Parkin at IBM using this phenomenon. Worldwide, the information stored digitally raised from around 3% in 1993 to 94% in 2007 [24] - a technological revolution. In the future, nano-electronics and devices which use quantum mechanical principles will be part of our everyday life and have the potential to change again our standard of living.

A powerful theoretical tool to describe these quantum systems connected to their environment, e.g., the electronic leads, bulk phonons, electromagnetic background fields and so on, is provided by the quan-

---

tum master equation (QME) [25, 26]. This is the basis of our investigations in this thesis, however there exist other descriptions of quantum processes like, e.g., the scattering-matrix approach [27]. In almost all real systems the number of degrees of freedom in the environment is huge and it is impossible to solve the whole quantum mechanical system including the environment. Therefore, the environment is traced out and only the information about the system of interest is retained. The environment enters through correlation functions which depend on the coupling and effective spectrum of the environment seen by the quantum system. Despite these restrictions, the solution of the QME in its general form remains challenging and often intractable. The most common simplifications of this theory are the Born and Markov approximations. The Born approximation assumes that the coupling strength between the quantum system of interest and its environment is weak, allowing one to keep only lowest order coupling terms in the QME. The Markov approximation requires that the correlation time of the environment is much shorter than typical system timescales. Then, one can assume that the state of the system simply depends on its present state and not on its past. We will have a closer look at the master equation and its derivation in chapter 2, where also basic notations and concepts are introduced following the textbooks and established results.

In this thesis, we are interested in the description of single magnetic atoms on metallic surfaces in the frame of the QME. Up to a few years ago, a reduction of magnetic bits to single atoms seemed impossible, but in experiments of Gambardella *et al.* [28] giant magnetic anisotropies of single cobalt atoms have been observed raising

expectations of applications. However, the lifetimes reached only the order of tens of nanoseconds. In spite of the large magnetic anisotropy, quantum tunneling between the ground states is possible through the anisotropy barrier. Investigations of single iron atoms [29, 30] with spin-polarized scanning tunneling microscopes (STM) led to the same conclusion that quantum tunneling destroys the stability of single atom memory bits even when the magnetic anisotropy barrier is large. The spin-polarized STM was developed in the group of R. Wiesendanger to investigate the lifetimes of the two ground states with opposite magnetic moment. Due to the differing number of spin up and down electrons in the tunneling current between the tip and the bulk via the magnetic atom, the atom state can be measured through the current [31]. The smallest possible size of a single bit appeared to be an iron atom cluster of the size of five atoms, which was investigated in experiments in the group of A. Khajetoorians and turned out to be stable for times longer than  $10^3$  s at low temperatures of around 0.3 K [32].

But, in the year 2013 experiments performed in the group of W. Wulfhekel at KIT for single holmium (Ho) atoms on platinum (Pt) showed surprising lifetimes in the order of minutes. We have to mention at this point that the results are under dispute in the community, and investigations of Steinbrecher *et al.* [33] could not confirm the long lifetimes. We will nevertheless concentrate on the experiments of W. Wulfhekel reported in publication [I] of the publication list. The stability can be explained by various properties and symmetries of the system, which prevent transitions between the ground states by single electron scattering. In Fig. 1.1, the energy level structure



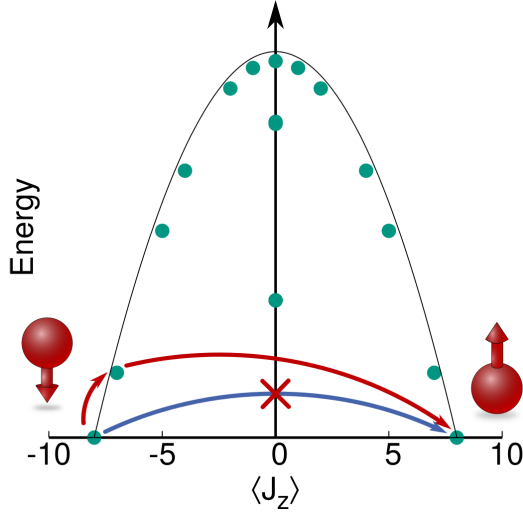


FIG. 1.1: Eigenenergies of the holmium atom on platinum vs. the expectation value of the z-projection  $J_z$  of the total angular momentum operator. A direct transition between the ground states by electron scattering is forbidden due to various properties and symmetries of the system.

is shown. In chapter 3, we develop first a theoretical description for general single magnetic atoms adsorbed on a metallic surface in contact with electronic reservoirs and derive in detail the corresponding QME. The transitions between the states of the single Ho atom on platinum are analyzed applying this theory. The different perturbations acting on the Ho atom and a comparison between experiment and theory are also presented in chapter 3. This was reported in publication [III].

In contrast to simpler theoretical approaches used to describe single magnetic adatoms [34–38], we solve the full QME instead of rate

equations for the populations. The solution of the full QME includes not only the populations, i.e., the diagonal elements of the density matrix, but also the coherences, i.e., the off-diagonal elements of the density matrix. Decoherence induced by the environment changes the properties of the system. It leads to a tradeoff between the coherent system dynamics and the dissipative environment. This results in a projection on to states, which are not the eigenstates of the system but of the full dissipative system. W. H. Zurek called this effect *environment-induced superselection* [39] and it is explained in more detail in Sec. 2.4.

Next, we investigate a solid-state lasing complex. In this context, we already mentioned superconducting qubits, which serve as artificial atoms. Another possibility is to use quantum dots. The energy level structure of the quantum dots can be efficiently tuned via capacitively coupled gates. Source and drain electrodes can be used to drive a current through the whole system. We will concentrate on quantum dots made up of nanoscale semiconducting islands, which are very well understood and controlled. The system of interest is a double quantum dot (DQD) coupled to a microwave oscillator which has been intensively investigated both in theory [40–45] as well as in experiments [46–52]. An analogous setting of the single-atom lasing can be realized with a single level in each of the dots as sketched in Fig. 1.2 a). Appropriate adjusting of the levels to resonance with the coupled microwave oscillator, combined with an applied bias voltage to produce a population inversion in the dots, lead to a lasing state in the oscillator [40–42]. In addition, the lasing situation has a clear signature in the transport properties of the DQD, which is

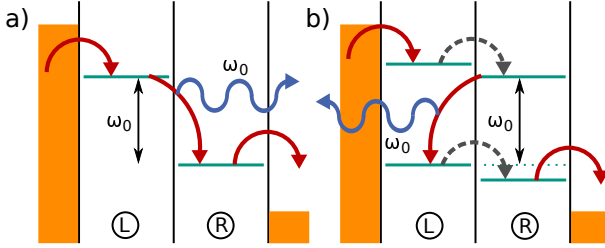


FIG. 1.2: a) Scheme of the lasing-type situation with a double quantum dot and one level in each dot. Tunneling processes of electrons and photons emitted to the microwave oscillator are illustrated by solid and wavy arrows, respectively. b) With two levels in each dot a cascade of transitions and various resonance situations leading to lasing can be achieved. In these cases also inelastic transitions mediated by phonons, indicated by dashed arrows, are important. Reprinted with permission of Ref. [V]. Copyright (2015) by the American Physical Society.

useful for verification in experiments. First verifications of the theoretical models were made in recent experiments of Liu *et al.* [48, 49]. The environmental effects on the DQD, i.e., relaxation and decoherence, lead to more complicated dynamics than in the ideal lasing scheme. Phonons have been identified as an important source of dissipation. At first sight, they produce further decoherence in the system which is usually unwanted for the proper operation of the device [43]. However, phonons also enhance transport through the DQD which increases the photon creation [44, 45, 51].

The situation becomes even more interesting and complex if multiple levels in each dot are involved in the transport through the DQD. This is described in chapter 4. The transition from the left to the right lead can involve several hopping processes in the DQD systems, which we call a cascade. Whenever the microwave oscillator is in res-

onance with one of the transitions, a lasing state may be induced. In Fig. 1.2 b) a specific situation is depicted in which four levels of the DQD system are required in the transition. The resonant tunneling process producing the photon in the microwave oscillator is associated with a charge transport in the opposite direction of the total current direction. The black dashed arrows represent incoherent transitions. They involve the emission of a phonon and are crucial for the performance of the lasing device. This is an example of a positive effect of the additional phonon coupling and deserve a proper theoretical study which is presented in chapter 4.

In both examples, the DQD and the single Ho atom, a QME with the Born-Markov approximation is used leading to a QME in Lindblad form. The connection and validity of the Born and Markov approximations are unclear from the derivation presented in chapter 2. The three important timescales of the problem are the one of the quantum system itself, the correlation time of the environment and the timescale associated with the coupling strength between environment and system. On the one hand, the Born approximation's validity depends on the coupling strength, on the other hand, the Markov approximation's validity depends on the correlation time. However, this distinction is unclear for higher orders beyond both approximations. Therefore, we develop in chapter 5 an exact expansion of the QME. It is important to know how to compute higher order terms and to estimate the time scales at which the Born and Markov approximation are valid. As an example how higher order terms in this expansion contribute to the solution we study the dynamics of the famous spin-boson model in Sec. 5.2. The spin-boson

---

model is a playground often used to investigate new concepts or ideas because of its simplicity, but nevertheless interesting dynamics. As in Ref. [53], we find the expected back flow of information from the bosonic environment to the spin for non-Markovian dynamics [54] and faster relaxation of the spin with higher order coupling terms.

Another question arises when excited initial states of the system are considered. If the dynamic behaves non-Markovian, i.e., it depends on its past, how can a simulation be started with a specific initial state? The system is in a non-Markovian simulation always entangled with the environment and can not be described as a product state, except for the equilibrium state [55]. With our expansion, the order of magnitude of this effect can be made as shown in Sec. 5.3.

The last problem we want to discuss in this framework in Sec. 5.4 are non-Markovian two-time correlators. In publication [IV], Jin *et al.* extended the formula for the evaluation of two-time correlators within the Markov approximation, known as the quantum regression theorem [25, 26, 56], to non-Markovian dynamics. However, in the derivation the Born approximation is used. In the frame of our expansion of the QME, we can estimate the timescale on which the formula is valid.



## Chapter

---

# 2 Theoretical Background

In this chapter we present the theoretical background required for the understanding of this thesis. Additionally, it gives the opportunity to use established results in the later calculations. First, the quantum master equation is derived in a textbook way, which has some major disadvantages. These are overcome with the time-convolutionless method developed by Breuer *et al.* [25, 53] and the diagrammatic expansion of the quantum master equation. In addition, an interpretation of the solutions of the quantum master equation is introduced, called environment-induced superselection. This is important if the influence of the environment on the system is strong.

## 2.1 Quantum Master Equation

The description of nano- or mesoscopic electronic systems is often based on the quantum master equation (QME). Here, we sketch the derivation from the textbook of Carmichael [26]. The description starts with dividing the system into three parts. First, the quantum system of interest with a small number of degrees of freedom is described by the Hamiltonian  $H_S(t)$  in the Hilbert space  $\mathcal{H}_S$ . The second part is the bath with many degrees of freedom with Hamiltonian  $H_B$  in the Hilbert space  $\mathcal{H}_B$ . And the third element is the coupling between them given by  $H_C(t)$ . Thus, the total Hamiltonian is given by three parts,

$$H(t) = H_S(t) + H_B + H_C(t). \quad (2.1)$$

A state of the total system in the Hilbert space  $\mathcal{H} = \mathcal{H}_S \otimes \mathcal{H}_B$  is determined by the density operator  $\rho_{SB}(t)$ . The focus in many problems is on the quantum system. Its state is represented by the reduced density matrix

$$\rho(t) = \text{Tr}_B \{ \rho_{SB}(t) \}. \quad (2.2)$$

$\text{Tr}_B\{\cdot\}$  symbolizes the trace over the bath degrees of freedom. We are interested in the dynamics of the reduced density matrix, but we start with the equation of motion for the total density operator  $\rho_{SB}$ . It is given by the Liouville-von Neumann equation ( $\hbar = 1$ )

$$\dot{\rho}_{SB}(t) = -i [H(t), \rho_{SB}(t)]. \quad (2.3)$$



In the interaction picture, an operator  $A$  is defined as

$$A_I(t) = U_0^\dagger(t_0, t) A U_0(t_0, t), \quad (2.4)$$

$$U_0(t_0, t) = \mathcal{T} e^{i \int_{t_0}^t dt' H_S(t')}, \quad (2.5)$$

where  $\mathcal{T}$  is the time-ordering operator. From now on the interaction picture is labeled by an index I. By tracing out the bath and using the above definition we obtain the QME in the interaction picture

$$\dot{\rho}_I(t) = - \int_{t_0}^t dt' \text{Tr}_B \{ [H_{C,I}(t), [H_{C,I}(t'), \rho_{SB,I}(t')]] \}. \quad (2.6)$$

In many textbooks, the following assumption is used

$$\rho_{SB,I}(t) = \rho_{S,I}(t) \rho_B^0 + \mathcal{O}(H_{C,I}(t)), \quad (2.7)$$

to further simplify Eq. (2.6) [26]. The idea behind the assumption is that the huge bath is not changed by the small quantum system and remains in its equilibrium state  $\rho_B^0$  in lowest order of the coupling. This is a non-systematic approach, e.g., it is not clear how to get the next order terms and we show in Sec. 2.3 the more accurate diagrammatic derivation of this equation. Nevertheless, the result is the master equation in the well-known Born approximation and reads

$$\dot{\rho}_I(t) = - \int_{t_0}^t dt' \text{Tr}_B \{ [H_{C,I}(t), [H_{C,I}(t'), \rho_{S,I}(t') \rho_B^0]] \}. \quad (2.8)$$

We choose the coupling term to be  $H_C(t) = g_C \sum_i s_i X_i$  with  $s_i$  as an

operator from the system Hilbert space and  $X_i$  as an operator from the bath Hilbert space. By explicitly computing the commutator and with the definition of the correlation functions

$$C_{ij}(t - t') = \text{Tr}_B \left\{ \rho_B^0 X_i(t) X_j(t') \right\}, \quad (2.9)$$

the QME can be written in the form

$$\begin{aligned} \dot{\rho}_I(t) = & - \sum_{ij} \int_{t_0}^t dt' [s_i(t) s_j(t') \rho_I(t') - s_j(t') \rho_I(t') s_i(t)] C_{ij}(t - t') \\ & + [\rho_I(t') s_j(t') s_i(t) - s_i(t) \rho_I(t') s_j(t')] C_{ji}(t' - t). \end{aligned} \quad (2.10)$$

The second common approximation is the Markov approximation. If the correlation functions  $C_{ij}(t)$  decay much faster than the typical time scales of the dynamics of the reduced density matrix  $\rho_I(t)$ , the dynamics only depend on the actual state of the system and not on the past. This implies the replacement of  $\rho_I(t')$  in the integrals by  $\rho_I(t)$  yielding the famous QME in Born-Markov approximation, used in a broad field of problems,

$$\begin{aligned} \dot{\rho}_I(t) = & - \sum_{ij} \int_{t_0}^t dt' [s_i(t) s_j(t') \rho_I(t) - s_j(t') \rho_I(t) s_i(t)] C_{ij}(t - t') \\ & + [\rho_I(t) s_j(t') s_i(t) - s_i(t) \rho_I(t) s_j(t')] C_{ji}(t' - t). \end{aligned} \quad (2.11)$$

The Lindblad-form of the QME is very similar to this equation and is often used in the field of quantum optics. It can be achieved by

transforming Eq. (2.11) back into the Schrödinger-picture [26]

$$\dot{\rho}(t) = i[\rho(t), H_S] + \sum_{i,j} \gamma_{ij} \left( 2L_i \rho(t) L_j^\dagger - \left( \rho(t) L_j^\dagger L_i + L_j^\dagger L_i \rho(t) \right) \right). \quad (2.12)$$

The Lindblad-operators  $L_{i/j}$  coincide with the operators  $s_{i/j}$ , and the transition rates  $\gamma_{ij}$  are connected to the correlation functions  $C_{ij}(t)$ . The Lindblad-form guarantees the semi-positive definiteness of the reduced density matrix during its time evolution [25]. We will use this simplified version of the QME during the investigations in chapters 3 and 4.

Both approximations, Born and Markov, are on one hand very restrictive and, on the other hand, in the way how they are introduced not very satisfying. For example, it is not clear what is the small expansion parameter for which these approximations are valid and what are the next order terms in the expansion. In chapter 5 we develop an accurate expansion of the QME with clearly defined higher order terms.

## 2.2 Time-Convolutionless Method

It is often useful to transform the general QME in a time local equation, meaning all the functions in the equation only depend on time  $t$ . Numerical simulations can be performed step by step without storing all the reduced density matrices of the past. For example, the QME with Born-Markov approximation or in Lindblad-form are time local. One possible way to get a time local QME beyond these approxima-

tions is to use the time-convolutionless (TCL) method developed by Breuer *et al.* [25, 53]. We will sketch briefly its derivation. It starts with introducing projection operators on the relevant part, the small quantum system,

$$\mathcal{P}\rho_{\text{SB}}(t) = \text{Tr}_{\text{B}} \{ \rho_{\text{SB}}(t) \} \otimes \rho_{\text{B}} = \rho(t) \otimes \rho_{\text{B}}, \quad (2.13)$$

and the irrelevant part, the bath,  $\mathcal{Q} = 1 - \mathcal{P}$ . From these definitions, the equations of motion can be derived again by the Liouville-von Neumann equation

$$\frac{d}{dt} \mathcal{P}\rho_{\text{SB}}(t) = \mathcal{P}\mathcal{L}(t)\mathcal{P}\rho_{\text{SB}}(t) + \mathcal{P}\mathcal{L}(t)\mathcal{Q}\rho_{\text{SB}}(t), \quad (2.14)$$

$$\frac{d}{dt} \mathcal{Q}\rho_{\text{SB}}(t) = \mathcal{Q}\mathcal{L}(t)\mathcal{P}\rho_{\text{SB}}(t) + \mathcal{Q}\mathcal{L}(t)\mathcal{Q}\rho_{\text{SB}}(t), \quad (2.15)$$

with the definition of the Liouvillian

$$\mathcal{L}(t)\cdot = -i[H_{\text{C,I}}(t), \cdot]. \quad (2.16)$$

These coupled equations of motion are formally solved by the Nakajima-Zwanzig generalized master equation which is exact in the relevant degrees of freedom of the reduced density matrix [25]

$$\begin{aligned} \frac{d}{dt} \mathcal{P}\rho_{\text{SB}}(t) &= \mathcal{P}\mathcal{L}(t)\mathcal{P}\rho_{\text{SB}}(t) + \mathcal{P}\mathcal{L}(t)\mathcal{G}(t, 0)\mathcal{Q}\rho_{\text{SB}}(0) \\ &\quad + \int_0^t dt' \mathcal{P}\mathcal{L}(t)\mathcal{G}(t, t')\mathcal{Q}\mathcal{L}(t')\mathcal{P}\rho_{\text{SB}}(t'), \end{aligned} \quad (2.17)$$

with  $\mathcal{G}(t, t')$  a chronological propagator, i.e., including the chronological time ordering operator  $\mathcal{T}$ . The second term  $\mathcal{P}\mathcal{L}(t)\mathcal{G}(t, 0)\mathcal{Q}\rho_{\text{SB}}(0)$

depends on the initial conditions and describes non-Markovian effects or entanglement between the system and the bath at  $t = 0$ . The chronological propagator is defined as

$$\mathcal{G}(t, t') = \mathcal{T} \exp \left( \int_{t'}^t dt'' \mathcal{Q}\mathcal{L}(t'') \right), \quad (2.18)$$

with  $\mathcal{T}$  the chronological time-ordering.

The TCL method gives a time local QME by introducing a backward propagator of the composite system

$$G(t, t') = \bar{\mathcal{T}} \exp \left( - \int_{t'}^t dt'' \mathcal{L}(t'') \right), \quad (2.19)$$

where  $\bar{\mathcal{T}}$  is the anti-chronological time ordering. Thus,  $G(t, t')$  can be interpreted as a reverse in time propagator. For simplification, we define the superoperator  $\mathcal{Y}(t)$

$$\mathcal{Y}(t) = \int_{t_0}^t dt' \mathcal{G}(t, t') \mathcal{Q}\mathcal{L}(t') \mathcal{P}G(t, t'). \quad (2.20)$$

The QME within the TCL method is then

$$\begin{aligned} \frac{d}{dt} \mathcal{P}\rho_{\text{SB}}(t) &= \mathcal{K}(t) \mathcal{P}\rho_{\text{SB}}(t) + \mathcal{P}\mathcal{L}(t) [1 - \mathcal{Y}(t)]^{-1} \mathcal{G}(t, t_0) \mathcal{Q}\rho_{\text{SB}}(t_0), \\ \mathcal{K}(t) &= \mathcal{P}\mathcal{L}(t) [1 - \mathcal{Y}(t)]^{-1} \mathcal{P}. \end{aligned} \quad (2.21)$$

This equation is exact and time local. Expanding the superoperator  $\mathcal{K}(t) = \sum_{n=1}^{\infty} g_C^n \mathcal{K}_n(t)$  in powers of the coupling strength  $g_C$  gives a correct expansion of the master equation. This expansion demon-

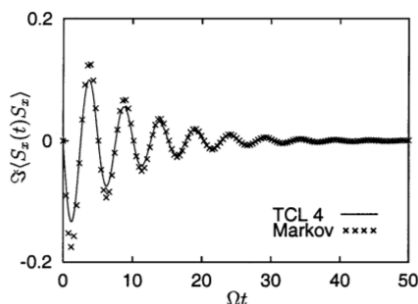


FIG. 2.1: Comparison of the imaginary part of the correlation function  $\langle S_x(t)S_x(0) \rangle$  between the TCL method up to fourth order in  $\mathcal{K}(t)$  and the Born-Markov approximation in the spin-boson model with a single spin  $\vec{S}(t) = (S_x(t), S_y(t), S_z(t))$  coupled to a bath of bosons in the low temperature regime. Figure taken with permission from Ref. [53]. Copyright (2001) by Elsevier.

strates that, e.g., non-Markovian effects can be important for short times and in the low temperature regime. An example for the spin-boson model is shown in Fig. 2.1. This will be discussed in more detail in Sec. 5.2.

The different terms of Eq. 2.21 are difficult to interpret in a physical way, because they, e.g., depend on the reverse time propagator. We therefore develop in chapter 5 a different approach to derive a time local expansion of the QME, which can easily be understood in each term of the expansion.

### 2.3 Diagrammatic Expansion of the QME

Another way to expand the quantum master equation in the coupling strength was found by Schoeller *et al.* in the 1990s [57, 58]. The

starting point is the equation of motion of one reduced density matrix element  $\rho_{nn'}(t)$  represented in the  $H_S$  eigenbasis  $|n\rangle$  with  $H_S |n\rangle = E_n |n\rangle$  [59]. For simplicity we focus on time-independent system and bath Hamiltonians.

One element of the reduced density matrix  $\rho(t)$  can be calculated with the expectation value of the projection operator  $\hat{p}_{nn'} = |n'\rangle \langle n|$ ,

$$\rho_{nn'}(t) = \langle n|\rho(t)|n'\rangle = \sum_{\tilde{n}} \langle \tilde{n}|\rho(t)|n'\rangle \langle n|\tilde{n}\rangle = \text{Tr}_S\{\rho(t)\hat{p}_{nn'}\}. \quad (2.22)$$

By switching to the interaction picture with respect to the Hamiltonian  $H_0 = H_S + H_B$ , we can define the time evolution operator in the interaction picture

$$U_I(t_0, t) = \mathcal{T} \left[ e^{i \int_{t_0}^t dt' H_{C,I}(t')} \right]. \quad (2.23)$$

We use now the approximation that at the initial time  $t_0$  the total density matrix  $\rho_{SB}(t)$  can be separated into the direct product of the system  $\rho(t_0)$  and the bath density matrix  $\rho_B(t_0)$

$$\rho_{SB}(t_0) = \rho(t_0) \otimes \rho_B(t_0) = \sum_{nn'} \rho_{nn'}(t_0) |n\rangle \langle n'| \otimes \rho_B(t_0). \quad (2.24)$$

This implies that system and bath are uncorrelated at time  $t_0$  which in general is not correct. However, in the limit  $t_0 \rightarrow -\infty$  or in a Markovian description, the assumption is satisfying. An out of equilibrium initial state of a non-Markovian system is always entangled with its environment [55]. We will analyze this assumption in Sec. 5.3 in more detail.

The expectation value of Eq. (2.22) leads with this considerations to

$$\begin{aligned} \rho_{nn'}(t) &= \text{Tr}_{\text{SB}}\{\rho_{\text{SB}}(t)\hat{p}_{nn'}\} \\ &= \sum_{\bar{n}\bar{n}'} \rho_{\bar{n}'\bar{n}}(t_0) \langle \bar{n} | \text{Tr}_{\text{B}}\{\rho_{\text{B}}(t_0)U_{\text{I}}(t_0, t)\hat{p}_{nn'I}(t)U_{\text{I}}(t, t_0)\} | \bar{n}' \rangle. \end{aligned} \quad (2.25)$$

With the exception of the initial product state this equation is still exact. In the next step, we expand the exponential functions of the time evolution operators  $U_{\text{I}}(t, t_0)$  in the coupling strength  $g_{\text{C}}$ . Eventually, the resulting integrals can be symbolized by diagrams and the master equation can be written as

$$\begin{aligned} \rho_{nn'}(t) &= \sum_{\bar{n}\bar{n}'} \rho_{\bar{n}'\bar{n}}(t_0) \prod_{\bar{n}\bar{n}' \rightarrow nn'} (t_0, t), \\ \prod_{\bar{n}\bar{n}' \rightarrow nn'} (t_0, t) &= \begin{array}{c} |\bar{n}\rangle \\ \text{---} \\ t_0 \\ \text{---} \\ |\bar{n}'\rangle \end{array} \begin{array}{c} \text{---} \\ |n'\rangle \\ \text{---} \\ t \\ \text{---} \\ |n\rangle \end{array} + \begin{array}{c} |\bar{n}\rangle \\ \text{---} \\ t_0 \\ \text{---} \\ |\bar{n}'\rangle \end{array} \begin{array}{c} \text{---} \\ |n'\rangle \\ \text{---} \\ t_1 \\ \text{---} \\ |n\rangle \end{array} + \dots \end{aligned} \quad (2.27)$$

The square at the right end of the diagram represents the projection operator  $\hat{p}_{nn'}(t)$  evaluated at time  $t$  and the dots symbolize the interaction Hamiltonians  $H_{\text{C}}(t_x)$ . We compute the integrals on the Keldysh contour [59] and a solid line depicts the free time evolution of the system. The different operators are ordered along the Keldysh contour, e.g.,

$$\begin{array}{c} |\bar{n}\rangle \\ \text{---} \\ t_0 \\ \text{---} \\ |\bar{n}'\rangle \end{array} \begin{array}{c} \text{---} \\ |n'\rangle \\ \text{---} \\ t_1 \\ \text{---} \\ |n\rangle \end{array} = \int_{t_0}^t dt_1 \int_{t_0}^{t_1} dt_2 \langle \bar{n} | \text{Tr}_{\text{B}}\{\rho_{\text{B}}(t_0)U_0(t_0, t_2)H_{\text{C}}U_0(t_2, t)\} | \bar{n}' \rangle$$



### 2.3 Diagrammatic Expansion of the QME

$$\times \hat{p}_{nn'} U_0(t, t_1) H_C U_0(t_1, t_0) \} |\bar{n}'\rangle. \quad (2.28)$$

With the previously defined coupling  $H_C = g_C \sum_i s_i X_i$  and Wick's theorem the trace over the bath can be calculated. The bath operator correlators decay into products of two time expectation values

$$\begin{aligned} \text{Tr}_B \{ \rho_B(t_0) X_{iI}(t_1) \dots X_{kI}(t_n) \} &= \langle X_{i1} \dots X_{kn} \rangle_B \\ &= \sum_j \langle X_{j1} X_{j2} \rangle_B \dots \langle X_{j_{n-1}} X_{jn} \rangle_B, \end{aligned} \quad (2.29)$$

with the short-hand notation  $X_{kI}(t_n) = X_{kn}$ . The sum over  $j$  contains all possible permutations of indices in  $X_{kn}$ . The diagrammatic representation of Wick's theorem for four vertices is

$$\begin{aligned} \underbrace{\begin{array}{c} t_4 \quad t_2 \\ \bullet \quad \bullet \\ | \bar{n} \rangle \quad | n' \rangle \\ t_0 \quad t \\ \bullet \quad \bullet \\ | \bar{n}' \rangle \quad | n \rangle \\ t_3 \quad t_1 \end{array}}_{\langle X_{i1} X_{j2} X_{k3} X_{l4} \rangle_B} &= \underbrace{\begin{array}{c} t_4 \quad t_2 \\ \bullet \quad \bullet \\ | \bar{n} \rangle \quad | n' \rangle \\ t_0 \quad t \\ \bullet \quad \bullet \\ | \bar{n}' \rangle \quad | n \rangle \\ t_3 \quad t_1 \end{array}}_{\langle X_{i1} X_{j2} \rangle_B \langle X_{k3} X_{l4} \rangle_B} + \underbrace{\begin{array}{c} t_4 \quad t_2 \\ \bullet \quad \bullet \\ | \bar{n} \rangle \quad | n' \rangle \\ t_0 \quad t \\ \bullet \quad \bullet \\ | \bar{n}' \rangle \quad | n \rangle \\ t_3 \quad t_1 \end{array}}_{\langle X_{i1} X_{l4} \rangle_B \langle X_{j2} X_{k3} \rangle_B} \\ &+ \underbrace{\begin{array}{c} t_4 \quad t_2 \\ \bullet \quad \bullet \\ | \bar{n} \rangle \quad | n' \rangle \\ t_0 \quad t \\ \bullet \quad \bullet \\ | \bar{n}' \rangle \quad | n \rangle \\ t_3 \quad t_1 \end{array}}_{\langle X_{i1} X_{k3} \rangle_B \langle X_{j2} X_{l4} \rangle_B}. \end{aligned} \quad (2.30)$$

A dashed line illustrates a contraction between two vertices, i.e.,

$$\gamma(s_{i,I}(t_x), s_{j,I}(t_y)) = \langle \bar{n}_x | s_{i,I}(t_x) | n_x \rangle \langle \bar{n}_y | s_{j,I}(t_y) | \bar{n}' \rangle \langle X_{ix} X_{jy} \rangle_B. \quad (2.31)$$

Here, the states  $|n_x\rangle$  and  $|\bar{n}_x\rangle$  ( $|n_y\rangle$  and  $|\bar{n}_y\rangle$ ) are the incoming and outgoing states at the vertex  $s_{i,\mathbb{I}}(t_x)$  ( $s_{j,\mathbb{I}}(t_y)$ ). The bath operator function is called correlation function of the bath  $C_{ij} = \langle X_{ix} X_{jy} \rangle_{\mathbb{B}}$  and reflects the properties of the bath as, e.g., the memory.

We can now proceed with using the standard text book method of defining the self-energy  $\Sigma_{\bar{n}\bar{n}' \rightarrow nn'}(t_0, t)$  as all non-separable diagrams of the full time-propagator  $\Pi_{\bar{n}\bar{n}' \rightarrow nn'}(t_0, t)$  [25], i.e.,

$$\boxed{\Pi} = \text{---} \text{---} \text{---} + \text{---} \text{---} \text{---} + \dots + \underbrace{\text{---} \text{---} \text{---}}_{\text{separable}} + \underbrace{\text{---} \text{---} \text{---}}_{\text{non-separable}} + \dots, \quad (2.32)$$

$$\boxed{\Sigma} = \text{---} \text{---} \text{---} + \text{---} \text{---} \text{---} + \text{---} \text{---} \text{---} + \text{---} \text{---} \text{---} + \text{---} \text{---} \text{---} + \dots \quad (2.33)$$

Using the Dyson-equation for  $\boxed{\Pi}$

$$\boxed{\Pi} = \boxed{\Pi_0} + \boxed{\Pi} \boxed{\Sigma} \boxed{\Pi_0}, \quad (2.34)$$

and that  $\boxed{\Pi_0}$  represents the free time evolution

$$\boxed{\Pi_0} = \text{---} \text{---} \text{---}, \quad (2.35)$$

it is possible to obtain the QME for the reduced density matrix. To return from the diagrammatic form of the QME to the real mathematical equations, several rules were formulated in reference [57]:

- A contraction from vertex 1 at time  $t_1$  to vertex 2 at time

$t_2$  yields the term  $\gamma(s_{i,I}(t_x), s_{j,I}(t_y))$ . All vertices are only attached to one contraction.

- The connection between two vertices along the Keldysh contour is given by  $\langle n|U_0(t_1, t_2)|n'\rangle$ , the free time evolution of the states.
- A diagram gets a prefactor  $(-1)^{a+b}$  with  $a$  the number of contractions and  $b$  the number of vertices on the lower part of the Keldysh contour.

This method creates an easy tool to investigate problems in an efficient way, e.g., to find a class of diagrams which can be summed and thus calculated to all orders, or to see higher order effects in the number of contractions. In a mathematic formulation, this means

$$\dot{\rho}(t) = i [\rho(t), H_S] + \int_{t_0}^t dt' \Sigma(t', t) \rho(t'), \quad (2.36)$$

$$\dot{\rho}_I(t) = \int_{t_0}^t dt' \Sigma_I(t', t) \rho_I(t'), \quad (2.37)$$

constituting an expansion in contractions of the self-energy  $\Sigma_I(t', t)$ . For a time-translational invariant problem, the self-energy only depends on the difference between the two times, i.e.,  $\Sigma_I(t - t')$ .

## 2.4 Environment-Induced Superselection

In the previous sections of this chapter, we presented the mathematical language to treat a quantum mechanical system coupled to a large environment. In this section, we will focus on one of the consequences of this framework stated first by Zurek in 1992 [39].

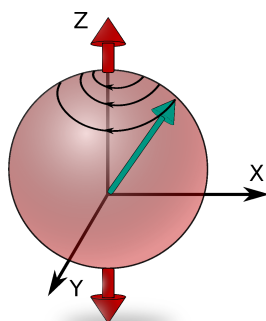


FIG. 2.2: Environment-induced superselection of a two level system represented by the Bloch sphere. Decoherence by an  $\sigma_z$  coupling forces an arbitrary state to the north or south pole of the sphere which is then a classical bit with one and zero state.

The question he addressed is: How does the classical world appear in the quantum mechanical description of a system? The basic idea is that the full Hilbert space of the quantum system is reduced by environment-induced decoherence to *pointer states* which are stable under this influence. In particular, a measuring device will decohere the system and thus change the measured outcome itself. A demonstrative example is the limit coupling strength to infinity, i.e.,  $g_C \rightarrow \infty$ . Then, the natural states of the system are the eigenstates of the coupling Hamiltonian  $H_C(t)$  and not the eigenstates of the system Hamiltonian  $H_S(t)$ . Another example is shown in Fig. 2.2 for a two level system represented by a Bloch sphere. The closed quantum system decoupled from the environment would let an arbitrary state (depicted by the green arrow) evolve with the time evolution of the system Hamiltonian. The coupling, which is in this example a  $\sigma_z$

coupling with  $\sigma_z$  the Pauli-matrix, yields decoherence in the system and the steady states are the up or down state of the system. In more complicated systems with  $g_C \neq 0$  and  $[H_C, H_S] \neq 0$  any state, which eventually is stable under the competition between system Hamiltonian and the coupling to the environment, can be the pointer state. For example, this state is recorded by the measurement device in experiments. The stable steady states calculated by the QME are a representation of these pointer states.

A separation in environment and system of interest, namely the small quantum system, is crucial for this interpretation of quantum mechanics. The universe is divided in quantum mechanical interacting systems with correlations between them [60]. Environment-induced superselection describes the transition between classical behavior of a system and the quantum mechanical properties. The boundary between classical and quantum mechanical can be shifted by the coupling strength and depends on the coupling to the environment as well as on the measurement. Furthermore, also the measurement device is correlated with the system and the environment. The measured quantity which is stored in the memory of the device is itself a pointer state and will be the only accessible state of the device. A detailed overview is given by Zurek in Ref. [60].



# 3 Chapter

---

## Single Magnetic Adatoms

We use the method of the quantum master equation developed in chapter 2 to evaluate the dynamics of a single magnetic atom on top of a metallic surface. The adsorbed atoms are called adatoms. In this setup the single adatom is coupled to the bulk electrons of the metal and in addition to the tip of a spin-polarized scanning tunneling microscope (STM). The coupling to the tip is experimentally required for read-out and manipulation of the atomic state. The stability of the single adatoms can be calculated with the QME and the solutions are compared with experimental results.

The demand for higher storage densities in the information technology sector is growing and will lead in the end to the maximal achievable density for atoms: one atom represents one bit. Promising candidates for this aim are magnetic adatoms which have a preferential direction of their magnetic moment. Essential for data storage are long lifetimes of the bit and the possibility to read and write the bit. With a spin-polarized current it is at least possible to read and manipulate these adatoms [I] [29, 30, 34, 61, 62]. The first long lifetimes of several minutes were measured by Miyamachi *et al.* [I] with exceptional gain over before measured lifetimes of a few hundred nanoseconds. We will present the theoretical background and a detailed analysis of these experiments in this chapter.

The magnetic adatoms are often analyzed by a STM and an exemplary picture is shown by Fig. 3.1. With a spin-polarized tip, which is typically anti-ferromagnetically coated, a spin-polarized current can be used. The anti-ferromagnetic coating has the advantage of reduced magnetic stray fields compared to a ferromagnetic tip. Still, a spin-polarized current can be produced due to the last atom or domain of the tip, which has a preferred magnetic direction. The spin-polarization offers the opportunity to measure the magnetic orientation of the sample.

### 3.1 Stevens Operator Method

The effective description of single magnetic atoms on top of a metallic surface, which we present here, is around 65 years old and originates from the work of Blenay, Elliot and Stevens (1953) [63, 64].



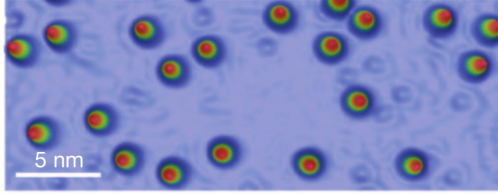


FIG. 3.1: Topographic STM picture of single Ho atoms on Pt(111) at 4.4 K. Figure taken with permission from Ref. [1]. Copyright (2013) by Nature Publishing Group.

The magnetic properties of the atom are determined by the electrons surrounding the nucleus. The influence of the nucleus itself will be neglected in the following discussion. Each electron features its own orbital angular momentum  $\vec{l}_i$  and spin  $\vec{s}_i$ . The total orbital angular momentum  $\vec{L} = \sum_{i=1}^{N_e} \vec{l}_i$  and the total spin  $\vec{S} = \sum_{i=1}^{N_e} \vec{s}_i$  of an electron configuration of the atom with  $N_e$  electrons produce the magnetic characteristics of the atom. Because of the relativistic spin orbit coupling the total angular momentum  $\vec{J} = \vec{L} + \vec{S}$  is an appropriate quantity to describe the magnetic atom which couples, e.g., to an external electromagnetic field or to scattering electrons. If the spin orbit coupling is strong,  $J$  is a good quantum number for the system and this will be assumed in the rest of this chapter. The possible values of  $J$  are

$$J = |L - S|, |L - S| + 1, \dots, L + S, \quad (3.1)$$

altogether known as the fine structure of the atom. Each multiplet belonging to one quantum number  $J$  is  $2J + 1$  times degenerate. The

quantum numbers  $S$ ,  $L$  and  $J$  of a multiplet can be identified with the help of Hund's rules [65]:

- I. Maximize the total spin  $S$ .
- II. Maximize the total orbital angular momentum  $L$ .
- III. If the shell is less than half full  $J = |L - S|$ , else  $J = L + S$ .

Because full shells do not contribute to the magnetic moment of the atom, only atoms with a partially filled shell are suitable for being magnetic atoms. For example, we will later consider Ho which has a  $4f^{10}$  electron configuration in compound with orbital angular momentum  $L = 6$ , spin  $S = 2$  and thus a total angular momentum  $J = 8$ .

The aforementioned degeneracy of all the states of a multiplet is lifted if the atom is placed on a surface [66]. The breaking of the spherical symmetry due to the surrounding charges of the bulk changes the energies. This change of the energies of the different total angular momentum states depends on the symmetry of the adsorption place and can lead to a magnetic anisotropy [64]. The calculation of the Coulomb potential of the crystal as point charges affecting each electron of the multiplet is very difficult and not practical. The Stevens operator method is an elegant way to avoid this issue. The Stevens operators  $O_n^m$  and  $\tilde{O}_n^l$  ( $n \geq 1$ ,  $0 \leq m \leq n$ ,  $1 \leq l \leq n$ ) which are polynomials of the total angular momentum operators  $J_z$ ,  $J_{\pm} = J_x \pm iJ_y$ , correspond to the effect of the coulomb potential of the lattice expressed in tesseral spherical harmonics on the atom. Tesseral spherical harmonics are also known as real-valued

### 3.1 Stevens Operator Method

---

spherical harmonics. The operators  $O_n^m$  and  $\tilde{O}_n^m$  contain  $J$  and  $J_z$  to the power  $n$  and the operators  $J_+$  and  $J_-$  to the power  $n - m$ . They are listed, e.g., in Ref. [67] and the relevant ones for Ho on Pt with a (111) surface configuration are listed in Sec. 3.3. In this sense, any crystal and adsorption site with a given symmetry can be expanded in these operators

$$H_{\text{CF}} = \sum_{n=1}^{\infty} \left( \sum_{m=0}^n B_n^m O_n^m + \sum_{l=1}^n \tilde{B}_n^l \tilde{O}_n^l \right). \quad (3.2)$$

The parameters  $B_n^m$  and  $\tilde{B}_n^l$  are known as Stevens or anisotropy parameters. They are very system specific as they depend on the symmetry of the adsorption site, the type of substrate and the magnetic atom.

If the leading term of the crystal field Hamiltonian  $H_{\text{CF}}$  is

$$B_2^0 O_2^0 = B_2^0 \left( 3J_z^2 - J(J+1) \right), \quad (3.3)$$

and  $B_2^0$  is negative, the eigenstates of the Hamiltonian are approximately the  $J_z$  eigenstates

$$H_{\text{CF}} \approx B_2^0 \left( 3J_z^2 - J(J+1) \right), \quad (3.4)$$

$$H_{\text{CF}} |m\rangle = E_m |m\rangle, \quad (3.5)$$

$$J_z |m\rangle = m |m\rangle, \quad (3.6)$$

and the energies vs. the  $J_z$  expectation value fit to an inverted parabola as shown in Fig. 3.2. The height of the parabola is known as the magnetic anisotropy barrier. This corresponds to an easy axes

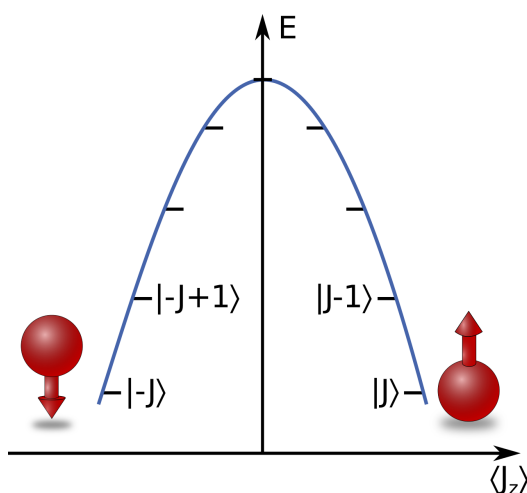


FIG. 3.2: The energies of the eigenstates of the crystal field Hamiltonian  $H_{\text{CF}} = B_2^0 (3J_z^2 - J(J+1))$  with  $B_2^0 < 0$  vs. the  $J_z$  expectation value. The maximum  $J_z$  states of the inverted parabola represent the two 'classical' bit states.

perpendicular to the metallic surface and the two ground states of the system are the states with maximum  $J_z$  expectation value pointing in or out of the surface. As a classical analogon, the two states represent one and zero of a bit on a computer. Therefore, these systems are promising candidates for single atom memory bits. In the following discussion, the focus will be most of the time on the case when the system has two degenerate ground states with maximum  $J_z$  expectation value. The influence of other Stevens operators is discussed with the specific example of Ho on Pt(111) in Sec. 3.3. In general, they result in new eigenstates of the system which are superpositions of the  $J_z$  eigenstates.

The Secs. 3.2-3.7 are based on the Ref. Karlewski *et al.* [III] and this publication will not be cited in this part any further.

## 3.2 Coupling of Adatoms to Electrons

The magnetic adatom is coupled on the one hand to the electronic bath of the metal and on the other hand to the spin-polarized STM tip. This tip is required for read-out and control of the state of the magnetic atom. The setup is shown schematically in Fig. 3.3 for the exemplary system of a single Ho atom on Pt(111).

The electrons of the two reservoirs, the bulk and the tip, dynamically scatter with the adatom and can change the angular momentum  $\vec{J}$ . The Hamiltonian which describes this system is

$$H = H_S + H_B + H_C, \quad (3.7)$$

$$H_S = H_{\text{CF}} + g_J \mu_B \vec{B} \cdot \vec{J}, \quad (3.8)$$

$$H_B = \sum_{\substack{\alpha=T,B \\ \sigma=\uparrow,\downarrow; k}} (\varepsilon_{k\sigma}^\alpha + eU^\alpha) c_{k\sigma}^{\alpha\dagger} c_{k\sigma}^\alpha, \quad (3.9)$$

$$H_C = \sum_{\substack{\alpha,\alpha'=T,B \\ kk'}} t_{kk'}^{\alpha\alpha'} \left\{ J_+ c_{k\downarrow}^{\alpha\dagger} c_{k'\uparrow}^{\alpha'} + J_- c_{k\uparrow}^{\alpha\dagger} c_{k'\downarrow}^{\alpha'} \right. \\ \left. + J_z \left[ c_{k\uparrow}^{\alpha\dagger} c_{k'\uparrow}^{\alpha'} - c_{k\downarrow}^{\alpha\dagger} c_{k'\downarrow}^{\alpha'} \right] \right\}, \quad (3.10)$$

and consists of three parts: First, the system Hamiltonian  $H_S$  including the crystal field Hamiltonian of the magnetic adatom and the coupling to an applied or stray magnetic field  $\vec{B}$ . Here, the parameter  $g_J = \frac{3}{2} + \frac{S(S+1)-L(L+1)}{2J(J+1)}$  is the Landé-factor and  $\mu_B$  is the

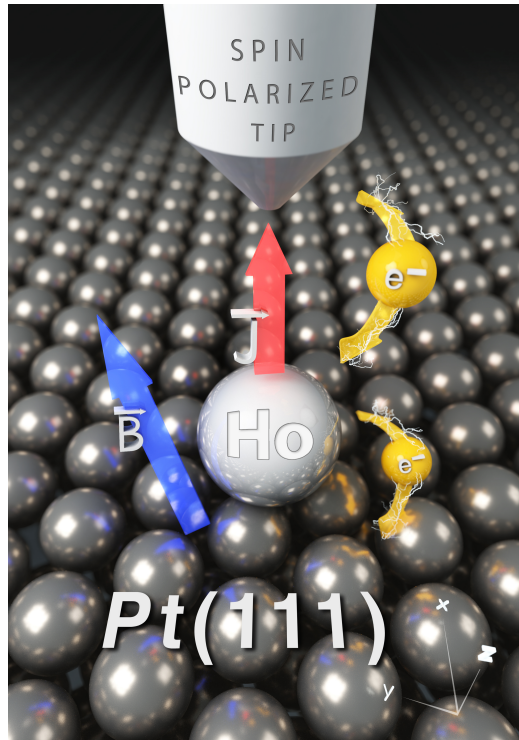


FIG. 3.3: Setting of the experiment in Ref. [I]: The magnetic state of a Ho atom on a Pt(111) surface is studied by a STM with a spin-polarized tip. Reprinted with permission from [III]. Copyright (2015) by the American Physical Society.

Bohr magneton.

Second, the total Hamiltonian contains the Hamilton operator describing the electron reservoirs  $H_B$ . The operator  $c_{k\sigma}^{\alpha\dagger}$  ( $c_{k\sigma}^{\alpha}$ ) creates (annihilates) an electron in the reservoir  $\alpha = T, B$ , where  $T$  stands for *tip* and  $B$  for *bulk*, with spin  $\sigma = \uparrow, \downarrow$ . The electron energy  $\varepsilon_{k\sigma}^{\alpha}$

is shifted by the potential of the bulk  $U^B$  or the tip  $U^T$ . The spin dependency of the electron energy  $\varepsilon_{k\sigma}^\alpha$  is later important for spin dependent density of states at the Fermi edge of the spin-polarized tip.

Third, the coupling between the electronic reservoirs and the system is needed. The first two terms in the coupling Hamiltonian  $H_C$  describe scattering with spin flip, whereas the third term is without change of the spin states. We have to distinguish between three possible processes affecting the adatom. For  $\alpha \neq \alpha'$  the term  $H_C$  corresponds to a tunneling electron from the tip to the bulk via the adatom or vice versa. For  $\alpha = \alpha' = B$ , the term describes the scattering of a bulk electron and for  $\alpha = \alpha' = T$  of a tip electron. The scattering strength of the different processes is parameterized by the amplitude  $t_{kk'}^{\alpha\alpha'}$ . In principle, electrons can scatter also with other multiplets of the magnetic adatom or tunnel directly between the tip and the bulk, which has to be taken into account by comparing the theoretically calculated current with experiments (see Sec. 3.4.1).

The dynamics of the magnetic adatom in contact with the mentioned reservoirs is governed by a QME in Lindblad-form as introduced in chapter 2 of this thesis. We will in the following develop the QME for this specific system. Metallic bulk and tip are supposed to be huge electron reservoirs weakly coupled to the magnetic adatom. Thus, the Born-Markov approximation can be used. In the interaction picture and with the coupling Hamiltonian as previously defined

we find

$$\begin{aligned}
 \dot{\rho}_I(t) = & - \sum_{\substack{\nu, \nu' = +, -, z \\ \alpha, \alpha' = T, B}} \int_0^\infty dt' \\
 & \times \left\{ [J_\nu(t) J_{\nu'}(t') \rho_I(t) - J_{\nu'}(t') \rho_I(t) J_\nu(t)] C_{\nu\nu'}^{\alpha\alpha'}(t-t') \right. \\
 & \left. + [\rho_I(t) J_{\nu'}(t') J_\nu(t) - J_\nu(t) \rho_I(t) J_{\nu'}(t')] C_{\nu\nu'}^{\alpha\alpha'}(t'-t) \right\}, \tag{3.11}
 \end{aligned}$$

with the dissipative kernel expressed by the correlation functions

$$C_{\nu\nu'}^{\alpha\alpha'}(t) = \sum_{k, k'} |t_{kk'}^{\alpha\alpha'}|^2 \langle s_{kk'\nu}^{\alpha\alpha'}(t) s_{k'k\nu'}^{\alpha'\alpha}(0) \rangle \tag{3.12}$$

with

$$\begin{aligned}
 s_{kk'-}^{\alpha\alpha'} &= c_{k\downarrow}^{\alpha\dagger} c_{k'\uparrow}^{\alpha'}, & s_{kk'+}^{\alpha\alpha'} &= c_{k\uparrow}^{\alpha\dagger} c_{k'\downarrow}^{\alpha'}, \\
 s_{kk'z}^{\alpha\alpha'} &= c_{k\uparrow}^{\alpha\dagger} c_{k'\uparrow}^{\alpha'} - c_{k\downarrow}^{\alpha\dagger} c_{k'\downarrow}^{\alpha'}. \tag{3.13}
 \end{aligned}$$

The Fourier transformed correlation functions are

$$\begin{aligned}
 \tilde{C}_{+-}^{\alpha\alpha'}(\hat{\omega}_{nm}) &= |t^{\alpha\alpha'}|^2 N_\uparrow^\alpha N_\downarrow^{\alpha'} \zeta(\hat{\omega}_{nm} + e(U^\alpha - U^{\alpha'})) \\
 \tilde{C}_{-+}^{\alpha\alpha'}(\hat{\omega}_{nm}) &= |t^{\alpha\alpha'}|^2 N_\downarrow^\alpha N_\uparrow^{\alpha'} \zeta(\hat{\omega}_{nm} + e(U^\alpha - U^{\alpha'})) \\
 \tilde{C}_{zz}^{\alpha\alpha'}(\hat{\omega}_{nm}) &= |t^{\alpha\alpha'}|^2 \left( N_\uparrow^\alpha N_\uparrow^{\alpha'} + N_\downarrow^\alpha N_\downarrow^{\alpha'} \right) \zeta(\hat{\omega}_{nm} + e(U^\alpha - U^{\alpha'})). \tag{3.14}
 \end{aligned}$$

We assume energy independent coupling constants  $t_{kk'}^{\alpha\alpha'} \approx t^{\alpha\alpha'}$  and define the spin-dependent electron densities of states at the Fermi-



### 3.2 Coupling of Adatoms to Electrons

---

edge  $N_\sigma^\alpha$  ( $\sigma = \uparrow, \downarrow$ ). Additionally, we introduce the matrix of the energy differences of the system  $\hat{\omega}_{nm} = E_n - E_m$ , with  $H_S |n\rangle = E_n |n\rangle$ .

The correlation functions are evaluated at the energy differences which are shifted by the energy of the applied voltage  $e(U^\alpha - U^{\alpha'})$ . The function  $\zeta(\omega)$  is given by

$$\zeta(\omega) = \int f(E) [1 - f(E - \omega)] dE = \frac{\omega}{\exp[\omega/(k_B T)] - 1},$$

where  $f(E) = [e^{E/(k_B T)} + 1]^{-1}$  is the Fermi function.

In this setting the STM tip is spin-polarized. We account for this by defining the tip polarization  $\eta = (P_\uparrow - P_\downarrow)/(P_\uparrow + P_\downarrow) \in [-1, 1]$  as it is done in the field of tunneling-magneto resistance. Here,  $P_{\uparrow/\downarrow}$  are the spin up and down populations of the tip. They enter in our calculation in the densities of states  $P_{\uparrow/\downarrow} \propto N_{\uparrow/\downarrow}^T = N^T \cdot \frac{1}{2}(1 \pm \eta)$ . The bulk is in most cases paramagnetic and, hence, the bulk electrons are not spin-polarized  $N_{\uparrow/\downarrow}^B = N^B$ . The remaining parameters, apart from the polarization  $\eta$ , can be combined in the coefficients

$$c_{\alpha\alpha'} = \frac{1}{2} |t^{\alpha\alpha'}|^2 N^\alpha N^{\alpha'}.$$

So far the theory is generally applicable to all magnetic adatoms which can be described by a single spin or total angular momentum on metal surfaces with Stevens operators. We will concentrate in the Secs. 3.3-3.7 on Ho on Pt(111) also analyzed in Ref. [I] and [68, 69].

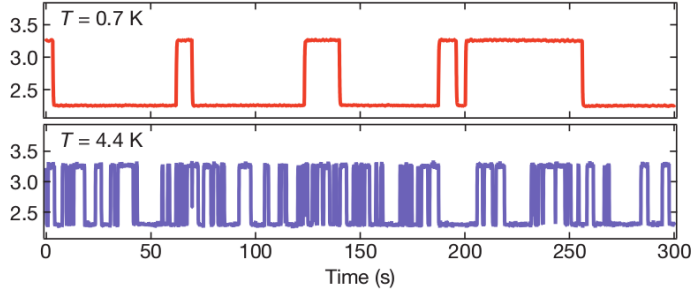


FIG. 3.4: The differential conductance vs. time for Ho on Pt(111) for the two temperatures  $T = 0.7$  K (top) and  $T = 4.4$  K (bottom). Reprinted with permission from Ref. [I]. Copyright (2013) by Nature Publishing Group.

### 3.3 Holmium on Platinum (111)

The values of the Stevens parameters and the total angular momentum are the determining factors of the characteristics of the adatom. For Ho on Pt(111), the conditions to use our theory are fulfilled because Ho has a strong spin orbit coupling as a rare earth metal [70] and the total angular momentum is a good quantum number for the system with  $J = 8$ . We consider in our theory only the dynamics of this multiplet with its 17 eigenstates. This setting showed exceptionally long lifetimes of the two ground states of the system in the experiment of Miyamachi *et al.* [I].

The measurements of the differential conductance vs. the time is shown in Fig. 3.4. The signature is telegraph-noise like corresponding to the switching between the two ground states. The lifetimes of the two ground states are in the order of minutes. In recent ex-

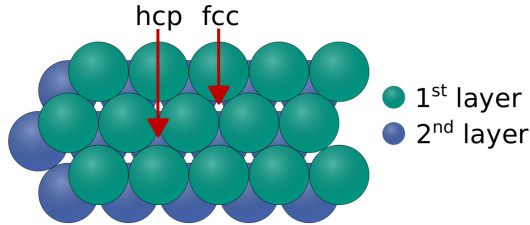


FIG. 3.5: Scheme of the Pt(111) surface with the two possible adsorption sites at the hcp and fcc positions.

periments of Steinbrecher *et al.* [33] the telegraph-noise could not be measured and the conclusion was that the  $4f$ -electron shell could not be detected by the STM-tunneling current. The  $4f$ -shell is shielded by the surrounding  $5s$ -shell and close to the nucleus, thus scattering with the tunneling electrons is suppressed. A possible explanation could be the larger noise levels in the measurement of Steinbrecher *et al.* [33]. We will continue in this work with the results of Miyamachi *et al.* [I].

The Pt(111) surface has two possible adsorption sites, one in the hexagonal close-packed (hcp) and one at the face-centered cubic (fcc) configuration, which is schematically shown in Fig. 3.5. From density functional theory (DFT) calculations the adsorption energy of the hcp site was estimated with around 6 meV and for the fcc site around 8 meV [I]. Thus, the fcc site is the preferred adsorption place. Both sites are located on a  $C_{3v}$  symmetric point of the lattice. The  $C_{3v}$  point group has three rotational axes and three vertical mirror planes. This has direct consequence on the crystal-field Hamiltonian of the adatom. Only the Stevens parameters obeying the three-fold

symmetry are included in the crystal-field Hamiltonian [63, 64]

$$\begin{aligned}
 H_{\text{CF}} &= \sum_{\substack{n=2,4,6 \\ m=0,3,6 \\ m \leq n}} O_n^m B_n^m & (3.15) \\
 &= 3J_z^2 B_2^0 + 35J_z^4 B_4^0 + \frac{1}{4} \left[ J_z, (J_+^3 + J_-^3) \right]_+ B_4^3 + \dots
 \end{aligned}$$

The index  $n$  has the constraints that it has to be non-negative, even because of the time inversion symmetry, and smaller or equal to  $2l$ , with  $l$  the orbital angular momentum of an electron as mentioned in Sec. 3.1. In the case of Ho,  $l$  equals 3 which results in a maximum of  $n = 6$ .

The  $C_{3v}$ -symmetry reflects itself in the appearing powers of the  $J^+$  and  $J^-$  operators occurring only in multiples of three, i.e.,  $m = 0, 3, 6$ . The full list of involved Stevens operators can be found in Ref. [1] and [71]. They are given by

$$O_2^0 = 3J_z^2 - J(J+1), \quad (3.16)$$

$$\begin{aligned}
 O_4^0 &= 35J_z^4 - 30J(J+1)J_z^2 + 25J_z^2 - 6J(J+1) \\
 &\quad + 3J^2(J+1)^2, & (3.17)
 \end{aligned}$$

$$O_4^3 = \frac{1}{4} \left[ J_z(J_+^3 + J_-^3) + (J_+^3 + J_-^3)J_z \right], \quad (3.18)$$

$$\begin{aligned}
 O_6^0 &= 231J_z^6 - 315J(J+1)J_z^4 \\
 &\quad + 735J_z^4 + 105J^2(J+1)^2J_z^2 - 525J(J+1)J_z^2 \\
 &\quad + 294J_z^2 - 5J^3(J+1)^3 \\
 &\quad + 40J^2(J+1)^2 - 60J(J+1), & (3.19)
 \end{aligned}$$

$$O_6^3 = \frac{1}{4} \left[ (11J_z^3 - 3J(J+1)J_z - 59J_z)(J_+^3 + J_-^3) + (J_+^3 + J_-^3)(11J_z^3 - 3J(J+1)J_z - 59J_z) \right], \quad (3.20)$$

$$O_6^6 = \frac{1}{2} [J_+^6 + J_-^6]. \quad (3.21)$$

The other important parts besides the Stevens operators are the associated Stevens parameters or crystal field parameters  $B_n^m$ . They define the strength of the different operators and hence the physical properties of the adatom. Miyamachi *et al.* [I] determined the Stevens parameters for Ho on Pt(111) at the fcc site by *ab-initio* DFT calculations listed in Tab. 3.1. The first excitation energy fits to the experimental measured inelastic step in the current spectrum. But Donati *et al.* [69] found another set of coefficients. They used only the parameters  $B_2^0$  and  $B_4^0$  to fit their experiments very accurately. The  $B_2^0$  term is in both cases dominating and negative leading to the general inverted parabola behavior. But in Ref. [69], the  $B_4^0$  coefficient is stronger which influences the position of the largest  $J$  states. We will have a closer look at the difference in the dynamics in Sec. 3.5.5, but concentrate our analysis on the parameters of Ref. [I].

The  $C_{3v}$ -symmetry is of course also reflected in the eigenstates of the crystal-field Hamiltonian  $H_{\text{CF}}$ . Because the generator of the rotation  $R_3 = e^{-i\frac{2\pi}{3}J_z}$  commutes with the crystal-field Hamiltonian  $[R_3, H_{\text{CF}}] = 0$ , the operators have a common set of eigenstates and we can label them with  $r = +, -, 0$  corresponding to the three possible eigenvalues of  $R_3 |\psi_m^r\rangle = e^{ri\frac{2\pi}{3}} |\psi_m^r\rangle$  [72]. The states can be represented as superpositions of the  $J_z$  eigenstates with magnetic

Anisotropy constant	Value
$B_2^0$	-239 $\mu\text{eV}$
$B_4^0$	86 neV
$B_4^3$	293 neV
$B_6^0$	0.186 neV
$B_6^3$	-1.967 neV
$B_6^6$	0.630 neV

TAB. 3.1: Anisotropy parameters as used in Ref. [I].

quantum numbers differing by multiples of three

$$|\psi_m^r\rangle = \sum_k a_{m,m\pm 3k}^r |m \pm 3k\rangle, \quad -J \leq m \pm 3k \leq J. \quad (3.22)$$

The sum over  $k$  contains all terms fulfilling the condition  $-J \leq m \pm 3k \leq J$ . The crystal-field Hamiltonian  $H_{\text{CF}}$  has  $2J + 1 = 17$  eigenstates which we label by a lower index  $m$  indicating the dominant  $J_z$  eigenstate  $|m\rangle$ . Therefore, the  $J_z$  expectation value together with the eigenenergy enables to identify a state and get information about superpositions of these states which will be useful for later investigations. This is shown in Fig. 3.6 a) for the  $H_{\text{CF}}$  eigenstates. The three sets +, - and 0 are depicted by red circles, green squares and blue triangles respectively. It can be clearly seen that the + and - set fit approximately on the inverted parabola, whereas the 0 states built superpositions with  $\langle J_z \rangle = 0$ .

Eigenstates from one of the sets contain no  $J_z$  eigenstates from one of the other sets. For example, the ground state  $|\psi_{-8}^-\rangle$  is made of the  $J_z$  eigenstates  $|-8\rangle$ ,  $|-5\rangle$ ,  $|-2\rangle$ ,  $|1\rangle$ ,  $|4\rangle$  and  $|7\rangle$ , whereas the

### 3.3 Holmium on Platinum (111)

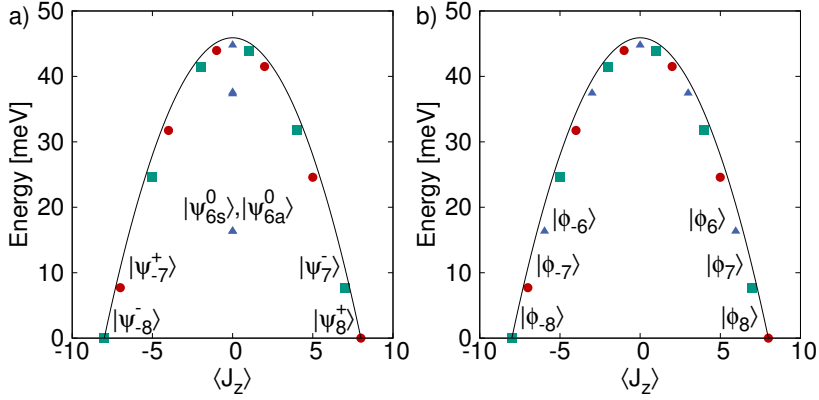


FIG. 3.6: a) Energies of the eigenstates of the Hamiltonian  $H_{CF}$  plotted vs. the expectation value  $\langle J_z \rangle$ . b) Energy expectation values of the steady states  $|\phi_m\rangle$  of the QME for strong dissipation due to an applied voltage of  $U = 7.3$  mV. The labels refer to the dominantly contributing  $J_z$ -eigenstates. Reprinted with permission from [III]. Copyright (2015) by the American Physical Society.

other ground state  $|\psi_8^+\rangle$  contains  $|-7\rangle$ ,  $|-4\rangle$ ,  $|-1\rangle$ ,  $|2\rangle$ ,  $|5\rangle$  and  $|8\rangle$ . This is also true for all the excited degenerated states belonging to the sets + and -. They are superpositions from non-degenerate  $J_z$  eigenstates. The situation is different for the 0 family. The possible  $J_z$  eigenstates are multiples of three, so the  $|\psi_m^0\rangle$  state consists of degenerate states coupled via the Stevens operators  $O_4^3$ ,  $O_6^3$  and  $O_6^6$ . The coupling yields a splitting in symmetric and antisymmetric (s,a) states  $|\psi_{6s}^0\rangle$ ,  $|\psi_{6a}^0\rangle$ ,  $|\psi_{3s}^0\rangle$  and  $|\psi_{3a}^0\rangle$  with zero  $J_z$  expectation value. This is shown by the centered blue triangles in Fig. 3.6 a).

An exceptional property of the Ho on Pt(111) system produces the long measured lifetimes which can be qualitatively understood

by looking at the matrix element  $\langle \psi_m^\sigma | J_\nu | \psi_{-m}^{-\sigma} \rangle$  for  $\nu \in \{+, -, z\}$ ,  $\sigma = \pm$  and all  $m$  between two degenerate eigenstates from different sets, i.e., the + and - set. This matrix element is needed for the rate between the states defined by a Fermi's Golden rule approximation giving a first estimation of the transition rate (we assume no potential difference in the electron reservoirs, see Eq. (3.14))

$$\Gamma_{m-m} = 2\pi |\langle \psi_m^\sigma | J_\nu | \psi_{-m}^{-\sigma} \rangle|^2 \zeta(0). \quad (3.23)$$

Specific for this system is that this matrix element is exactly zero. The reasons are the combination of the  $C_{3v}$ -symmetry of the adsorption site and the time-reversal symmetry for zero magnetic field  $\vec{B} = 0$ . As described before the  $C_{3v}$ -symmetry determines the relevant Stevens operators and thus the coupling between the eigenstates. Additionally, the time reversal symmetry with the time reversal operator  $\mathcal{T}$  yields [I]

$$\begin{aligned} \mathcal{T}^2 &= 1, & \langle \chi | \phi \rangle &= \langle \mathcal{T} \phi | \mathcal{T} \chi \rangle, \\ \mathcal{T} J_\nu &= -J_\nu \mathcal{T}, & \mathcal{T} | \psi_m^\sigma \rangle &= | \psi_{-m}^{-\sigma} \rangle. \end{aligned} \quad (3.24)$$

The matrix element  $\langle \psi_m^\sigma | J_\nu | \psi_{-m}^{-\sigma} \rangle$  with these ingredients is given by

$$\begin{aligned} \langle \psi_m^\sigma | J_\nu | \psi_{-m}^{-\sigma} \rangle &= \langle \mathcal{T} \psi_m^\sigma | \mathcal{T} J_\nu \psi_{-m}^{-\sigma} \rangle^* = -\langle \psi_{-m}^{-\sigma} | J_\nu \mathcal{T} \psi_m^\sigma \rangle^* \\ &= -\langle \psi_{-m}^{-\sigma} | J_\nu | \psi_m^\sigma \rangle^* = -\langle \psi_m^\sigma | J_\nu | \psi_{-m}^{-\sigma} \rangle, \end{aligned} \quad (3.25)$$

$$\Rightarrow \langle \psi_m^\sigma | J_\nu | \psi_{-m}^{-\sigma} \rangle = 0. \quad (3.26)$$

Therefore, transitions between degenerated eigenstates from different



sets with single electron scattering are forbidden. In particular, the two ground states  $|\psi_{\pm 8}^{\pm}\rangle$  are decoupled and are very stable which was observed in Ref. [I].

The described symmetry protection would suggest that the lifetimes are infinitely long, but in the experiments of Miyamachi *et al.* [I] lifetimes in the order of minutes were measured. This is caused by several possible perturbations on the system. The electronic reservoirs of the bulk and the tip are at non-zero temperature and an applied voltage  $U$  additionally gives the electrons enough energy to overcome the lowest energy gap of the crystal-field Hamiltonian. These excitations can then decay to the other side of the parabola and lead to transitions between the ground states. Furthermore, the symmetry protection is based on time-inversion symmetry which can be broken by various perturbations of the Hamiltonian, e.g., a magnetic stray field creating direct transitions between the ground states. Altogether, the finite relaxation time  $T_1$  is the significant quantity characterizing the system and its external influences.

#### 3.3.1 Pointer States of Ho on Pt(111)

The interesting properties of the system, e.g., lifetimes of the ground states, are encoded in the QME for the magnetic adatoms (3.11). A detailed explanation how to effectively implement the general QME in a numerical computer program is given in Appendix A.1. We describe in this part the specific terms for Ho on Pt(111). To achieve a form of the QME easily solvable with standard numerical tools, we

transform Eq. (3.11) to

$$\dot{\vec{\rho}}(t) = \mathcal{M}\vec{\rho}(t), \quad (3.27)$$

with the density matrix  $\vec{\rho}(t)$  reshaped from a square matrix (here  $17 \times 17$ ) to a vector (with 289 components). The large matrix  $\mathcal{M}$  ( $289 \times 289$ ) contains all the coherent and dissipative dynamics of the system. The disadvantage of the method is the quadrature of the problem dimension, but this is often balanced by the simplicity of the resulting QME. An important step to achieve this structure is the relation [73]

$$\text{vec}\{AXB\} = (A \otimes B^T)\text{vec}\{X\}, \quad (3.28)$$

where  $A$ ,  $X$  and  $B$  are matrices. The function  $\text{vec}\{\cdot\}$  is the vectorization of a matrix in row-ordered form, i.e., each row is taken in turn to create the vector. The Kronecker product depicted by the symbol  $\otimes$  is defined as

$$A \otimes B = \begin{bmatrix} a_{11}B & \cdots & a_{1n}B \\ \vdots & \ddots & \vdots \\ a_{m1}B & \cdots & a_{mn}B \end{bmatrix}. \quad (3.29)$$

In our case, we are interested in the reduced density matrix  $\rho(t)$  corresponding to the matrix  $X$ . The operators  $J_\nu(t)$  from the coupling Hamiltonian  $H_C$  together with proper used identity matrices are the matrices  $A$  and  $B$ .

In the Born-Markov approximation, the time integrals of the QME

can be calculated explicitly by using the correlation functions of the system and the time dependency of the system operators  $J_{\nu}(t)$  [II] [74]. We define

$$S_{\nu\nu'}^{\alpha\alpha'\pm} \equiv \int_0^{\infty} d\tau C_{\nu\nu'}^{\alpha\alpha'}(\pm\tau) e^{-iH_S\tau} J_{\nu'} e^{iH_S\tau}. \quad (3.30)$$

The time evolution operators can be evaluated in the system eigenbasis  $H_S |n\rangle = E_n |n\rangle$  and the matrix elements of  $S_{\nu\nu'}^{\alpha\alpha'}(\pm\tau)$  are

$$\begin{aligned} \langle n | S_{\nu\nu'}^{\alpha\alpha'\pm} | m \rangle &= \int_0^{\infty} d\tau C_{\nu\nu'}^{\alpha\alpha'}(\pm\tau) \\ &\quad \times \langle n | e^{-iH_S\tau} | n \rangle \langle n | J_{\nu'} | m \rangle \langle m | e^{iH_S\tau} | m \rangle \end{aligned} \quad (3.31)$$

$$= \langle n | J_{\nu'} | m \rangle \int_0^{\infty} d\tau C_{\nu\nu'}^{\alpha\alpha'}(\pm\tau) e^{i\hat{\omega}_{nm}\tau} \quad (3.32)$$

$$= \langle n | J_{\nu'} | m \rangle \left[ \frac{1}{2} C_{\nu\nu'}^{\alpha\alpha'}(\pm\hat{\omega}_{nm}) - iP \int \frac{d\omega}{2\pi} \frac{C_{\nu\nu'}^{\alpha\alpha'}(\omega)}{\hat{\omega}_{nm} \mp \omega} \right]. \quad (3.33)$$

We use the diagonal form of  $H_S$  in its eigenbasis, define the matrix of energy differences with the entries  $\hat{\omega}_{nm} = E_m - E_n$  and indicate again the Fourier transform of the correlation function by its argument in frequency space.

With this definition, the large matrix  $\mathcal{M}$ , which contains as mentioned all the information of the dynamics, is given by

$$\mathcal{M} = \mathcal{M}_C + \mathcal{M}_D \quad (3.34)$$

$$\mathcal{M}_C = i \left( \mathbb{1} \otimes H_S^T - H_S \otimes \mathbb{1} \right) \quad (3.35)$$

$$\begin{aligned} \mathcal{M}_D = - \sum_{\substack{\nu, \nu' = +, -, z \\ \alpha, \alpha' = T, B}} & \left[ \left( J_\nu S_{\nu\nu'}^{\alpha\alpha'+} \otimes \mathbf{1} \right) - \left( S_{\nu\nu'}^{\alpha\alpha'+} \otimes (J_\nu)^T \right) \right. \\ & \left. + \left( \mathbf{1} \otimes [S_{\nu\nu'}^{\alpha\alpha'-} J_\nu]^T \right) - \left( J_\nu \otimes [S_{\nu\nu'}^{\alpha\alpha'-}]^T \right) \right]. \end{aligned} \quad (3.36)$$

The coherent part of the QME defined by the system Hamiltonian  $H_S$  is represented by  $\mathcal{M}_C$  and the dissipative part is induced by scattering with electrons by  $\mathcal{M}_D$ .

Important information about the dynamics of the system is given by the spectral decomposition of this matrix

$$\mathcal{M} \vec{\rho}_n = m_n \vec{\rho}_n, \quad (3.37)$$

$$\vec{\rho}(t) = \sum_{n=1}^{289} c_n \vec{\rho}_n e^{m_n t}. \quad (3.38)$$

All rates along different transition paths in the adatom are given by the eigenvalues and eigenstates of  $\mathcal{M}$ . The coefficients  $c_n$  are determined via the initial state at  $t_0$ . Obviously, the steady state of the system  $\vec{\rho}(t \rightarrow \infty) = \vec{\rho}_{st} = \vec{\rho}_0$  corresponds to the eigenvector with zero eigenvalue  $m_0 = 0$  [75]. All other eigenvalues need to be negative relaxation rates. Their transition paths  $\vec{\rho}_n$ ,  $n > 0$ , are decaying to zero in the long time limit. For more details see Appendix A.1.

The calculation of the full QME can be computationally intensive and the interpretation of transition rates is difficult because of the mixture of coherent and incoherent transitions as described before. Thus, it is often useful or desirable to reduce the QME to rate equations between the populations  $P_i$  of a set of basis states. This kind of reduction is possible if the coherences, the off-diagonal elements

of the density matrix, decay much faster in this basis than the non-equilibrium populations. Then, the time scales of the dynamics are separated and the off-diagonal elements can be neglected

$$\frac{dP_i}{dt} = \sum_j (\Gamma_{ji}P_j - \Gamma_{ij}P_i). \quad (3.39)$$

A transition from state  $|j\rangle$  to state  $|i\rangle$  is characterized by the rate  $\Gamma_{ji}$ . The choice of the basis is the central problem in this description, because of the required decoupling between coherences and populations. If the bath coupling is very small, the obvious selection are the eigenstates of the system  $H_S$ . They will probably be hardly affected by the environment. The success of this model and the proper description of physical effects was, e.g., presented in Refs. [34–38].

This reduction to classical rate equations is impossible if the basis states (for example, the  $H_S$  eigenstates) are not weakly affected by the environment. Therefore, the use of the previously described spectral decomposition of Eq. (3.38) including all off-diagonal dynamics is necessary. The steady state solution eigenvectors, i.e., the eigenbasis of the steady state reduced density matrix, are superpositions of different  $H_S$  eigenstates. In our case this applies especially for the 0-set of  $H_S$  eigenstates which are coherent symmetric and antisymmetric superpositions of predominantly two  $J_z$  basis states. In this discussion we assume zero magnetic field, i.e.,  $H_S = H_{CF}$ . Thus, the 0-set states have vanishing  $J_z$  expectation value as shown in Fig. 3.6 a). The coupling to the environment can cause decoherence and reduces the system to states being stable under this coupling in the long time limit. Zurek called this environment-induced superselection [39, 60]

and we made a short overview of this interpretation in Sec. 2.4. We represent the pointer states by  $|\phi_m\rangle$  and  $m = -J, -J + 1, \dots, J$ , which are the steady state solutions of the QME (3.38) [76]. Again, the lower index  $m$  indicates the predominantly  $J_z$  basis state of the superposition  $|\phi_m\rangle$ . For the case of strong dissipation in comparison with the coupling between the  $J_z$  basis states  $|\pm 6\rangle$  the pointer states approach de facto the original  $J_z$  basis states and fit nearly on the inverted parabola as displayed in Fig. 3.6 b). The states  $|\phi_{\pm 6}\rangle$  and  $|\phi_{\pm 3}\rangle$  have then non-vanishing  $J_z$  expectation values  $\langle J_z \rangle \approx \pm 6$  and accordingly  $\langle J_z \rangle \approx \pm 3$ .

In Fig. 3.7 we have a closer look at the  $U$  dependency of the  $J_z$  expectation value of the pointer states  $|\phi_{\pm 6}\rangle$ . This displays the composition of the  $J_z$  basis states. The plot shows two limiting cases. On the one hand, for low voltages the  $\langle J_z \rangle$ -value is nearly zero indicating that the symmetric and antisymmetric  $H_{\text{CF}}$  eigenstates  $|\psi_{6s}^0\rangle$  and  $|\psi_{6a}^0\rangle$  are untouched. The electrons do not have enough energy to scatter into the high excitations  $|\phi_{\pm 6}\rangle$ . On the other hand, for higher voltages, the scattering becomes possible and the dissipation decoheres the superposition to the states with maximum  $\langle J_z \rangle$ . Because of the finite temperature, this starts already for energies below the first excitation energy of 7.7 meV. At the first excitation energy, a distinct dip back to the symmetric and antisymmetric states appears. This is caused by the resonance of the applied voltage with the first excitation. Because the energy gaps in the system are not equidistant, a transition to the first excited state and then a direct decay to the ground states is much more likely than an additional excitation.

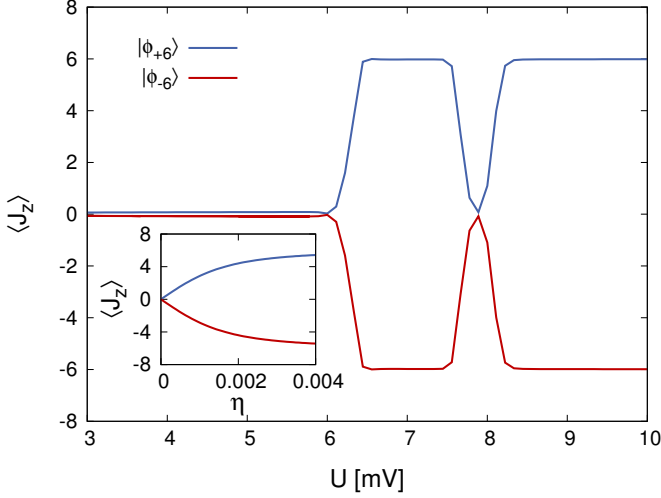


FIG. 3.7: Expectation value  $\langle J_z \rangle$  of the pointer states  $|\phi_{+6}\rangle$  and  $|\phi_{-6}\rangle$  vs. the voltage  $U$  for a tip polarization  $\eta = -0.15$ , and in the inset vs. the polarization  $\eta$  for  $U = 7.3$  mV. The other parameters are  $B_z = 10^{-8}$  T and  $c_{TB} = 3.41 \cdot 10^6 (\text{meV s})^{-1}$ . Reprinted with permission from [III]. Copyright (2015) by the American Physical Society.

The polarization of the tip  $\eta$  is important for the selection of the maximum  $\langle J_z \rangle$  values by the environment-induced superselection. The dependency of the  $\langle J_z \rangle$  values on the tip polarization  $\eta$  is presented in the inset of Fig. 3.7. A polarization in  $z$ -direction is assumed. The electrons without polarization ( $\eta = 0$ ) produce no spin dependent scattering with the Ho adatom, therefore the pointer states possess no favored magnetic moment direction and the pointer states remain the symmetric and antisymmetric superpositions. However, the system saturates already for small polarizations  $\eta$  to the pointer states with maximum  $\langle J_z \rangle$ .

This environment-induced superselection has direct consequences on relaxation rates and, thus, on the lifetimes of the two ground states which will be analyzed in the next Sec. 3.4.

### 3.4 Relaxation Time $T_1$

The relaxation time  $T_1$  of the system corresponding to the decay time of a non-equilibrium state to the steady state can be calculated by the spectral decomposition of the matrix  $\mathcal{M}$  as defined in the previous Sec. 3.3.1. One condition is that the system is primarily in one of the two ground states. Therefore, low temperatures of the setting are required to exclude too much thermal excitations. In the experiments of Ref. [I] the temperature was 0.7 K (i.e.,  $k_B T \approx 0.060$  meV). This is well below typical system energies like the first excitation energy 7.7 meV. In this case, the inverse of the  $T_1$  time is according to its amount smallest negative non-zero eigenvalue  $m_1$  of the matrix  $\mathcal{M}$  (see Eq. (3.38)) belonging to slowest transition in the system with the eigenvector  $\vec{\rho}_1 = (1, 0, \dots, 0, -1)^T$ . The entries of the vector  $\vec{\rho}_1$  are listed in the order in which the first and the last entries are the populations of the two ground states  $|\phi_{\pm 8}\rangle$ .

All possible relaxation channels between the two ground states contribute in the transition rate  $-m_1 = 1/T_1 = \Gamma_{-8 \rightarrow +8} + \Gamma_{+8 \rightarrow -8}$ . This is different from the already introduced rates, e.g.,  $\Gamma_{-88}$ , by the rate equations (3.39). They just account for the direct transition between the states, whereas  $\Gamma_{-8 \rightarrow +8}$  from  $|\phi_{-8}\rangle$  to  $|\phi_8\rangle$  also includes transitions via excited states. The spin-polarization of the tip or a magnetic field create different lifetimes  $\tau_{+8}$  and  $\tau_{-8}$  for



the two ground states given by the quotient of the rates  $\Gamma_{-8 \rightarrow +8}$  and  $\Gamma_{+8 \rightarrow -8}$  and the steady state populations  $P_{-8}$  and  $P_{+8}$ , i.e.,  $\tau_{-8}/\tau_{+8} = \Gamma_{+8 \rightarrow -8}/\Gamma_{-8 \rightarrow +8} = P_{-8}/P_{+8}$ .

### 3.4.1 Current through the Tip

One crucial parameter of the model is the coupling strength of the tunneling electrons via the Ho atom which is needed to compare the theory with the experiment of Ref. [I]. With the measured current through the tip, it is possible to estimate this coupling by matching the theoretical predicted current via the QME with the actual experimental data. In the model, the current through the tip is defined as the time-derivative of the number of electrons in the tip  $N_T(t)$ ,

$$N_T(t) = \sum_{k\sigma} \left( c_{k\sigma}^T \right)^\dagger (t) c_{k\sigma}^T(t), \quad (3.40)$$

$$I_{\text{Th}}(t) = e \frac{d}{dt} \langle N_T(t) \rangle = ie \langle [H, N_T(t)] \rangle. \quad (3.41)$$

All terms of the Hamiltonian  $H$  commute with the number of electrons  $N_T(t)$  except of the coupling Hamiltonian  $H_C$  yielding

$$\begin{aligned} I_{\text{Th}} = & -ie \sum_{kk'} \left( t^{TB} \right)^2 \left( \langle J_+ \left( c_{k\downarrow}^B \right)^\dagger c_{k'\uparrow}^T \rangle + \langle J_- \left( c_{k\uparrow}^B \right)^\dagger c_{k'\downarrow}^T \rangle \right. \\ & + \langle J_z \left[ \left( c_{k\uparrow}^B \right)^\dagger c_{k'\uparrow}^T - \left( c_{k\downarrow}^B \right)^\dagger c_{k'\downarrow}^T \right] \rangle - \langle J_+ \left( c_{k\downarrow}^T \right)^\dagger c_{k'\uparrow}^B \rangle \\ & \left. - \langle J_- \left( c_{k\uparrow}^T \right)^\dagger c_{k'\downarrow}^B \rangle - \langle J_z \left[ \left( c_{k\uparrow}^T \right)^\dagger c_{k'\uparrow}^B - \left( c_{k\downarrow}^T \right)^\dagger c_{k'\downarrow}^B \right] \rangle \right). \quad (3.42) \end{aligned}$$

As one would suspect, the current consists of positive terms corre-

sponding to tunneling processes from the tip to the bulk and of negative terms describing the backwards events. The structure is very similar to the dissipative part of QME  $\mathcal{M}_D$  and the same mathematic procedures are applicable. We are again interested in the stationary limit of the current and the resulting equation is [77],

$$\mathcal{M}_D^I = \sum_{\nu, \nu'} \left\{ S_{\nu\nu'}^{TB+} \otimes J_\nu^T + J_\nu \otimes [S_{\nu\nu'}^{TB-}]^T - S_{\nu\nu'}^{BT+} \otimes J_\nu^T - J_\nu \otimes [S_{\nu\nu'}^{BT-}]^T \right\}, \quad (3.43)$$

$$I_{\text{Th}} = \text{Tr} \left[ \hat{I}_{\text{Th}} \rho_{\text{St}} \right] = e \sum_{ij} (\mathcal{M}_D^I)_{(j-1) \cdot 17 + j, i} (\vec{\rho}_{\text{St}})_i. \quad (3.44)$$

The matrix multiplication of the supermatrix  $\mathcal{M}_D^I$  and the steady state density matrix  $\vec{\rho}_{\text{St}}$  is calculated by the sum over  $i$  with  $1 \leq i \leq 17^2 = 289$ , whereas the trace is given by the sum over  $j$  with  $1 \leq j \leq 17$ . The vectorization of the trace leads to the difficult  $j$  dependency of the supermatrix  $\mathcal{M}_D^I$ .

The current described by  $I_{\text{Th}}$  contains electrons tunneling via the Ho atom from or to the tip. However, there exist additional electrons which tunnel directly between tip and bulk and other electrons which tunnel via the Ho atom but do not scatter with the  $4f$  shell, i.e., the multiplet of interest. This 'leakage' current  $I_{\text{Leak}}$  is independent of the state of the Ho atom and therefore can be separately identified. Particularly, the differential conductance  $G = dI/dU(U)$  shows for the transition between elastic scattering of electrons, i.e., below the first excitation gap, to inelastic scattering above the first excitation gap a step  $s = G(U^>)/G(0) - 1$  with  $eU^> > \Delta E_{87}$ . This step depends

on the ratio between the elastic and inelastic channels and thus on the state of the Ho atom. With increasing leakage current  $I_{\text{Leak}}$  the step size gets reduced. The theoretical predicted step size by  $I_{\text{Th}}$  would be 10% without leakage current, whereas in the experiment a step size of  $s_{\text{Exp}} \approx 0.9\%$  was measured. This leads to the conclusion that the leakage current accounts for 90% of the total current and only 10% are represented by  $I_{\text{Th}}$  yielding a step size of  $s_{\text{Tot}} \approx 1\%$ . An accordance between theory and experiment is thereby achieved.

In the experiments the total current was measured and fixed at the value  $I_{\text{Exp}} = 1 \text{ nA}$ . The theoretical current  $I_{\text{Th}}$  is about 10% of the total current, i.e.,  $I_{\text{Th}} = 0.1 \text{ nA}$ . With this value for the current we can fix the coupling strength of the electrons resulting in  $c_{TB} = 3.41 \cdot 10^6 (\text{meV s})^{-1}$  for  $U = 3 \text{ mV}$ .

#### 3.4.2 Voltage Dependency

With the help of the pre-examinations made in the last sections, we can start the numerical investigation of the lifetimes of the Ho ground states and the dependency on several parameters and perturbations. We will focus most of the time on the regime of voltages above  $U = U^T - U^B > 3 \text{ meV}$  as they were applied in the experiments. The used voltage is needed to measure the current and to get information about the state of the Ho atom. Under this conditions, the influence of the tunneling electrons is dominant compared to the scattering of tip electrons, thus we neglect them in this analysis, i.e.,  $c_{TT} = 0$ . Additionally, the bulk electrons have little effect on the system due to their small energy (low temperatures). We will have a closer look at them separately in Sec. 3.5.1 and in the derivation of

the  $T_2$  time in Sec. 3.6, i.e.,  $c_{BB} = 0$  for most parts. In all numerical investigations we added a very weak magnetic field in z-direction ( $B_z = 10^{-8}$  T) because of numerical stability of the solution. Without the magnetic field in some parameter regimes divergences could occur or the reduced density matrix becomes non-positive semidefinite because of the complete decoupling of the two ground states.

We begin with the relaxation time  $T_1$  dependency on the applied tip voltage  $U$ . Different temperatures are used starting from  $T = 0.7$  K as in the experiments to  $T = 1.4$  K,  $T = 3.5$  K, and last  $T = 7$  K. For each temperature and also in the later figures, the outcome which is numerical achieved by the full QME solution is plotted together with the result from the approximate rate equations (3.39) in the basis of the  $H_S$  eigenstates.

For the two lowest temperatures  $T = 0.7$  K and  $T = 1.4$  K and low voltages (below 7 mV and below 5.5 mV, respectively) the system shows an exponentially activated behavior. This is reflected in the linear part of the solid lines in the semi-log plot of Fig. 3.8. Both, the full QME and the rate equations, describe this physical effect nearly identically. An excitation from the ground state to one of the first excited states  $|\phi_7\rangle$  or  $|\phi_{-7}\rangle$ , decays in some cases into the ground state on the opposite side of the parabola, being the leading transition channel between the two ground states. The excitation process is the bottleneck of this transition and defines the relaxation time  $1/T_1 \approx \Gamma_{87} + \Gamma_{-8-7}$ . Approximately, without tip polarization and magnetic field, the rates  $\Gamma_{87}$  and  $\Gamma_{-8-7}$  are equal and are given

### 3.4 Relaxation Time $T_1$

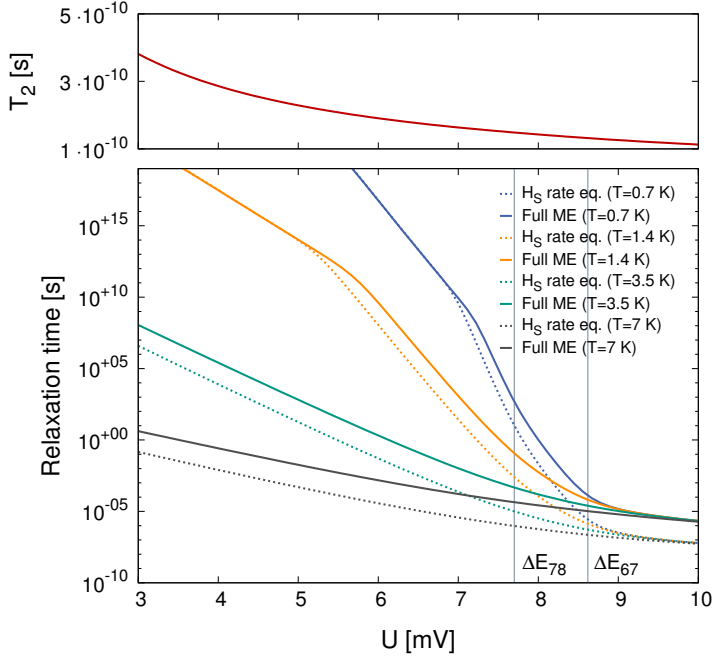


FIG. 3.8: Relaxation time  $T_1$  and decoherence time  $T_2$  of the two ground states vs. the applied voltage  $U$  obtained from the full QME (3.38) (solid lines) and the rate equation (3.39) based on  $H_S$  eigenstates (dotted lines). A weak magnetic field  $B_z = 10^{-8}$  T is applied, the temperatures are  $T = 0.7$  K,  $T = 1.4$  K,  $T = 3.5$  K and  $T = 7$  K, and the coupling strength is  $c_{TB} = 3.41 \cdot 10^6 (\text{meV s})^{-1}$ . Reprinted with small modifications and permission from [III]. Copyright (2015) by the American Physical Society.

by

$$\Gamma_{87} = c_{TB} |\langle \psi_7^- | J_- | \psi_8^+ \rangle|^2 \cdot \zeta(E_7 - E_8 - eU) \quad (3.45)$$

$$\approx 16c_{TB} \frac{(E_7 - E_8 - eU)}{e^{(E_7 - E_8 - eU)/k_B T} - 1}. \quad (3.46)$$

Above 7 mV the lifetimes calculated by the two methods start to deviate from each other, for high voltages several orders of magnitude. The reason is the environment-induced superselection of the symmetric and antisymmetric  $H_{\text{CF}}$ -eigenstates  $|\psi_{6s}^0\rangle$  and  $|\psi_{6a}^0\rangle$  decaying in the full QME in the pointer states  $|\phi_{\pm 6}\rangle$ . A detailed investigation is given in Sec. 3.3.1. In the rate equations the states  $|\psi_{6s}^0\rangle$  and  $|\psi_{6a}^0\rangle$  possess large overlap matrix elements and therefore high transition rates between each other and also to both sides of the parabola. This yields a 'shortcut' through the anisotropy barrier and if the states are energetically available, i.e., if the scattering electrons have enough energy to excite the system up to the 0-set states, this leads to a high switching probability. In contrast, the pointer states  $|\phi_{\pm 6}\rangle$  in this regime are approximately the  $J_z$  eigenstates  $|\pm 6\rangle$  as shown in the Figs. 3.7 and 3.9 a). The coupling between these states is weak and the shortcut is closed. The stability of the ground states grows drastically. The same applies for the higher  $|\psi_{3s}^0\rangle$  and  $|\psi_{3a}^0\rangle$  states from the 0-set.

The slope of the curves changes again qualitatively at voltages above 8.6 mV corresponding to the largest energy gap of the system between the first and second excited states  $\Delta E_{67} = E_6 - E_7 \approx 8.6$  meV. All the electrons contain enough energy to excite the system to all higher states independent of the temperature. Thus, the leading transition channel is sequential tunneling over the top of the parabola. Therefore, the slope of  $T_1(U)$  vs.  $U$  flattens. This is generic for all plots with different temperatures, because the additional energy provided by the heat of the electrons is not needed. But for lower voltages the temperature is important. Higher temperatures

### 3.4 Relaxation Time $T_1$

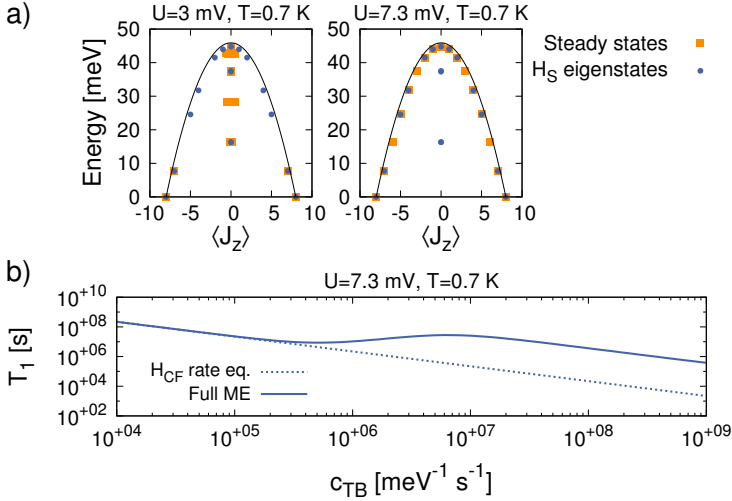


FIG. 3.9: a) Energy expectation values vs. the expectation values  $\langle J_z \rangle$  for the steady states of the full QME and for the  $H_S$  eigenstates at  $T = 0.7$  K for  $U = 3$  mV and  $U = 7.3$  mV. b) Relaxation time  $T_1$  vs. the coupling strength  $c_{TB}$  as obtained from the full QME and the rate equation for  $T = 0.7$  K and  $U = 7.3$  mV. Reprinted with permission from [III]. Copyright (2015) by the American Physical Society.

smear out the borders between the different regimes, especially for  $T = 3.5$  K and  $T = 7$  K. For these temperatures, the plots in Fig. 3.8 for the full QME and the rate equations are always separated, meaning the switching is always via higher excited states. The rate equations underestimate the stability of the ground states.

To emphasize the difference between the pointer states and the  $H_S$ -eigenstates we plotted  $\langle J_z \rangle$  vs. the energy for two different applied voltages  $U$  in Fig. 3.9 a). For the low voltage ( $U = 3$  mV) the excitations to the high excited states are exponentially suppressed.

The states  $|\psi_{6s}^0\rangle$  and  $|\psi_{6a}^0\rangle$  are unaffected by scattering and the superpositions remain. The higher pointer states can not be tracked numerically, because these states are nearly completely unpopulated, thus they cluster in the full QME solution non-physically. As no scattering in these states occurs they have no influence on the physical properties of the system. For the high voltage ( $U = 7.3$  mV) scattering in all excited states is possible and the pointer states fit approximately on the inverted parabola (orange squares). The shortcut between left and right side of the parabola is closed.

This of course depends on the coupling strength  $c_{TB}$  of the electrons which we investigate in Fig. 3.9 b) for the experimental temperature  $T = 0.7$  K and  $U = 7.3$  mV. When the rate equations lead to the same lifetimes as the full QME, the shortcut remains also for the full QME. This is true for small coupling strengths  $c_{TB} < 10^5$  (meV s) $^{-1}$ . For the rate equations the lifetimes have a  $1/c_{TB}$  dependency, because the rates are proportional to the coupling strength. However, in the full QME the destruction of the symmetric and the antisymmetric state with rising coupling strength even increases the lifetimes in the range of  $10^5$  (meV s) $^{-1} \leq c_{TB} \leq 10^7$  (meV s) $^{-1}$ . The two sides of the parabola become more and more decoupled.

### 3.4.3 Experimental Issues

In the experiments of Ref. [I] two modifications of the setting described so far were made for technical reasons which we have to take into account if we want to compare our results. First, the applied tip voltage was not a fixed DC voltage but modulated to



### 3.4 Relaxation Time $T_1$

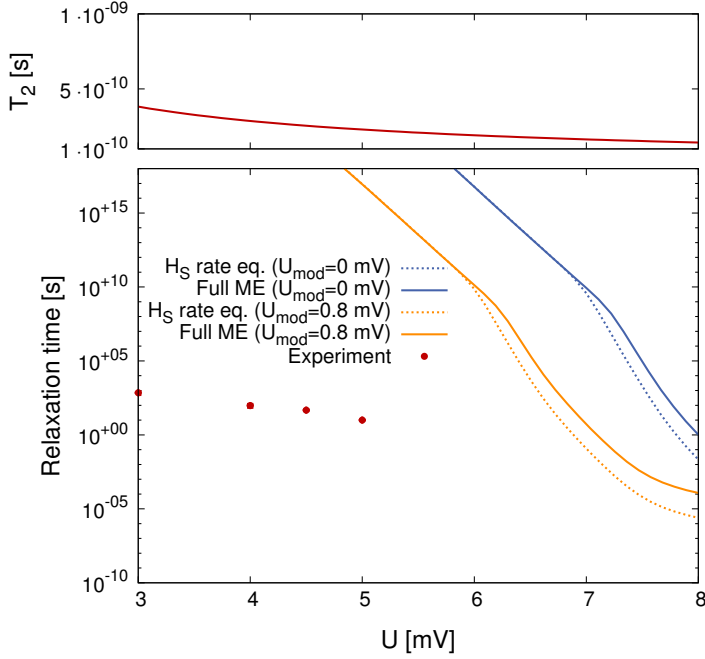


FIG. 3.10: Relaxation time  $T_1$  and decoherence time  $T_2$  of the two ground states vs. the applied voltage  $U$  in a weak magnetic field  $B_z = 10^{-8}$  T at  $T = 0.7$  K for the full QME solution and the rate equation (3.39) with the  $H_{CF}$  eigenstates with and without modulation voltage  $U_{\text{mod}} = 0.8$  mV. For comparison the experimental data are shown in red. Reprinted with small modifications and permission from [III]. Copyright (2015) by the American Physical Society.

measure derivatives of the current,  $U_{\text{tot}}(t) = U + \sqrt{2}U_{\text{mod}} \cos(\omega t)$ , with  $U_{\text{mod}} = 0.8$  mV and a frequency of  $\omega = 720$  Hz. The period of one oscillation is several orders of magnitude shorter than our timescales of interest which are the lifetimes of the ground states in order of seconds. Accordingly, we can describe the modulation by

an energy distribution of the tunneling electrons. The cosine implies that many electrons experience the maximum or minimum potential energy  $U \pm \sqrt{2}U_{\text{mod}}$ , whereas only few electrons undergo the average potential energy  $U$ . This can be modeled with the energy distribution  $h(U') = 1/\pi [2(eU_{\text{mod}})^2 - (eU')^2]^{-1/2}$  for  $U' \leq \sqrt{2}U_{\text{mod}}$  and  $h(U') = 0$  otherwise [78]. The energy distribution has to be convoluted with the correlation functions  $\tilde{C}_{ij}^{\alpha\alpha'}(\hat{\omega}_{nm})$  in which the electron energies enter, e.g.,

$$\tilde{C}_{+-}^{TB}(\hat{\omega}_{nm}) = c_{TB} \frac{1}{2} (1 + \eta) \int dU' \zeta(\hat{\omega}_{nm} + eU^T + eU') h(U'). \quad (3.47)$$

In Fig. 3.10 the difference between the solutions with and without the modulation is shown. The highest energy electrons become dominant and the modulation yields essentially a shift to  $U \rightarrow U + \sqrt{2} \cdot U_{\text{mod}}$ , in our case approximately 1.1mV.

The second modification of our theory is that in the experiments the tunnel current in the STM setting was kept fixed at  $I_{\text{Exp}} = 1 \text{ nA}$ . This was achieved by fine-tuning the distance between tip and Ho adatom. We can implement this feature by assigning a  $U$  dependency  $c_{TB}(U)$  to the coupling strength. The tunnel contact operates in this parameter regime almost as an Ohmic resistance,  $I_{\text{Th}} \approx U/R_{Tun}$ . To keep the current fixed the coupling strength has to be  $c_{TB}(U) \propto 1/U$ . Of course, this is not exact, e.g., at the transition from elastic to inelastic scattering, where new transport channels open, but the difference is very small. As shown in the Sec. 3.4.1, 90% of the current is leakage current and with  $c_{TB}(U = 3 \text{ mV}) = 3.41 \cdot 10^6 (\text{meV s})^{-1}$  the theoretical current is  $I_{\text{Th}} = 0.1 \text{ nA}$ , in agreement with the ex-

### 3.4 Relaxation Time $T_1$

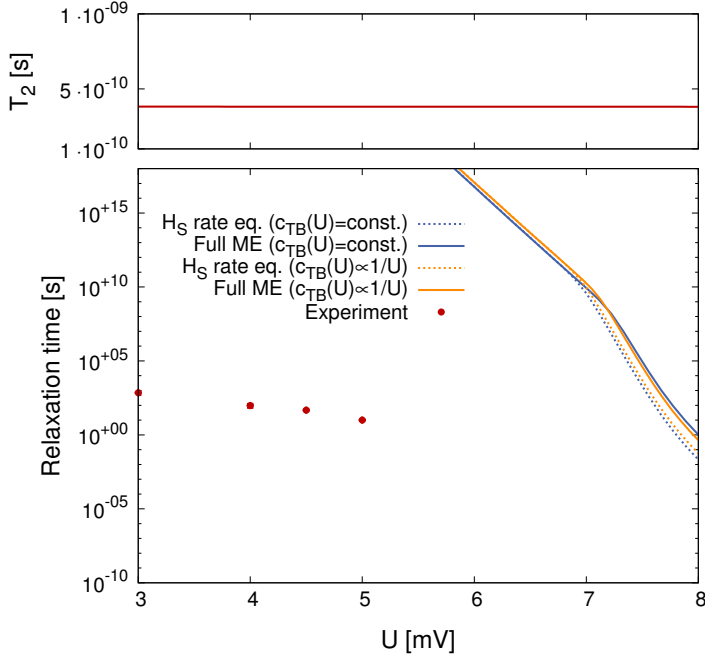


FIG. 3.11: Relaxation time  $T_1$  and decoherence time  $T_2$  of the two ground states vs. the applied voltage  $U$  in a weak magnetic field  $B_z = 10^{-8}$  T at  $T = 0.7$  K for the full QME solution and the rate equation (3.39) with the  $H_{CF}$  eigenstates with and without tip distance correction. For comparison the experimental data are shown in red. Reprinted with small modifications and permission from [III]. Copyright (2015) by the American Physical Society.

periment. The influence of this correction of the coupling strength is shown in Fig. 3.11. The difference between solutions with and without correction is small. Because the coupling strength becomes smaller for larger  $U$  with the correction, the difference between the full QME and the rate equations result is smaller as without the

correction and large  $U$  (see also Fig. 3.9 b)).

## 3.5 Deviations from the Ideal Situation

The previous simulated relaxation times are several orders of magnitude longer as measured in experiments depicted by the red dots in Figs 3.10 and 3.11. The theory overestimates the stability of the ground states. The ideal situation we described so far has to be modified by perturbations and experimental deviations from this model. Some of the possible issues are presented in the Secs. 3.5.1 to 3.5.5 and, eventually, we get lifetimes in the right order of magnitude with realistic parameters.

### 3.5.1 Scattering of Bulk Electrons

We started our investigation with setting the scattering strength of bulk electrons  $c_{BB}$  to zero. Reasons for this are, on the one hand, that they have not enough energy to overcome the first excitation gap. On the other hand, we see a clear voltage dependency of the lifetimes emphasizing the leading impact of the tunneling electrons. In this part, we will have a closer look at the influence of the bulk electrons on the model and answer the question if they could solve the discrepancy between theory and experiment. We add the scattering of the bulk electrons as an extra bath in the QME which is possible in the Born-Markov approximation. The coupling strength to the bulk electrons  $c_{BB}$  is assumed to be slightly higher than the coupling of the tunneling electrons  $c_{BB} = 1.0 \cdot 10^7 (\text{meV s})^{-1} > c_{TB} = 3.41 \cdot 10^6 (\text{meV s})^{-1}$  to see a clear effect of the bulk electrons. The results of the simu-

### 3.5 Deviations from the Ideal Situation

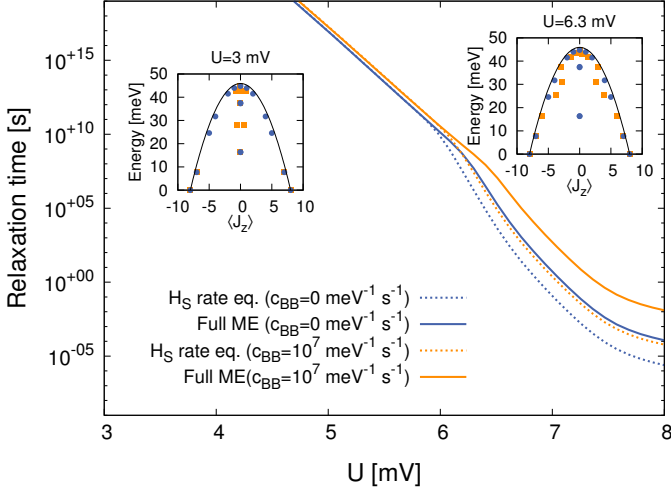


FIG. 3.12: Relaxation time  $T_1$  vs. the voltage  $U$  for the model with modulation voltage broadening and tip distance correction with and without bulk electron scattering strength  $c_{BB} = 1.0 \cdot 10^7 (\text{meV s})^{-1}$ . Reprinted with small modifications and permission from [III]. Copyright (2015) by the American Physical Society.

lations are presented in Fig. 3.12. The voltage modulation and tip distance correction are also included. As expected, the bulk electrons possess not enough energy to excite the system and 'cool' the system into its ground states yielding longer lifetimes. They can not be responsible for the shorter lifetimes measured in the experiments and, counter intuitively, the additional coupled environment stabilizes the system by freezing it in its ground states.

### 3.5.2 Breaking the $C_{3v}$ -Symmetry

In the experimental adatom system the  $C_{3v}$ -symmetry of the adsorption site is probably not perfectly fulfilled. For example, the tip could not be directly centered over the Ho atom, or defects in the crystal break the symmetry. We will use as an exemplary term the Stevens operator  $B_2^1 \cdot O_2^1 = B_2^1 \cdot [J_z, J_+ + J_-]_+$  [79] breaking *all* the rotational symmetries of the system. In real systems, a lower symmetry could remain in the system, even with defects and so on, which would be interesting to investigate in future. A magnetic field in the xy-plane along some specific axes would lead to a similar effect.

The influence of the symmetry-breaking term is shown in Fig. 3.13 for a Stevens parameter  $B_2^1$  between  $10^{-15}$  meV and  $10^{-3}$  meV and the voltage  $U = 6$  mV. The leading term of the crystal-field Hamiltonian  $B_2^0 = -0.239$  meV remains dominating in this range of  $B_2^1$  and our general considerations are still valid. The main effects of the symmetry breaking are the mixing of the  $H_{\text{CF}}$  eigenstates and the loss of the symmetry protection. A direct transition between the ground states becomes possible and is the main transition channel in the Fig. 3.13 for the rate equations (dotted lines). The full QME  $T_1$  time is not affected by the symmetry breaking up to  $B_2^1 \approx 10^{-11}$  meV. The main transition remains over the first excitation and a subsequent decay. For comparison, the lifetime for  $U = 6$  mV in the ideal model was approximately  $T_1 \approx 10^{17}$  s. For  $B_2^1 > 10^{-11}$  meV, the  $T_1$  time is in both models inverse proportional to the symmetry breaking strength squared, i.e.,  $T_1 \propto (B_2^1)^{-2}$ .

The result of the rate equations differs a lot from the full QME

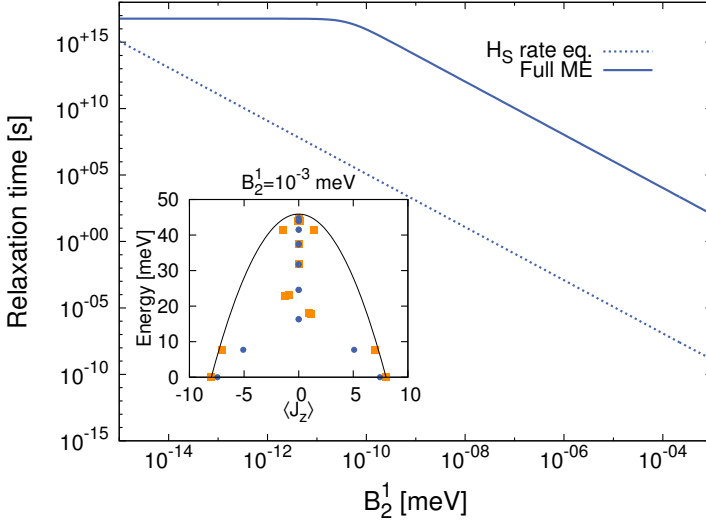


FIG. 3.13: Relaxation time  $T_1$  vs. Stevens parameter  $B_2^1$  characterizing the deviation from the perfect trigonal symmetry. We compare the results obtained from the full QME (3.38) and the rate equation (3.39) based on the  $H_S$  eigenstates. We choose the parameters  $U = 6$  mV and  $B_z = 10^{-8}$  T. The inset shows the  $J_z$  expectation value of the steady states and the  $H_S$  eigenstates. Reprinted with small modifications and permission from [III]. Copyright (2015) by the American Physical Society.

solution. The coupling to the environment again destroys the mixing of the states and leads to pointer states closer to the  $J_z$  eigenstates. This is depicted in the inset of Fig. 3.13. The focus is here on the ground states of the system which are directly coupled via  $B_2^1$ . The  $J_z$  expectation values of the first excited states  $|\phi_{\pm 7}\rangle$  are also much closer to the inverse parabola as the  $H_S$  eigenstates. This is further the reason why the full QME solution does not change for small

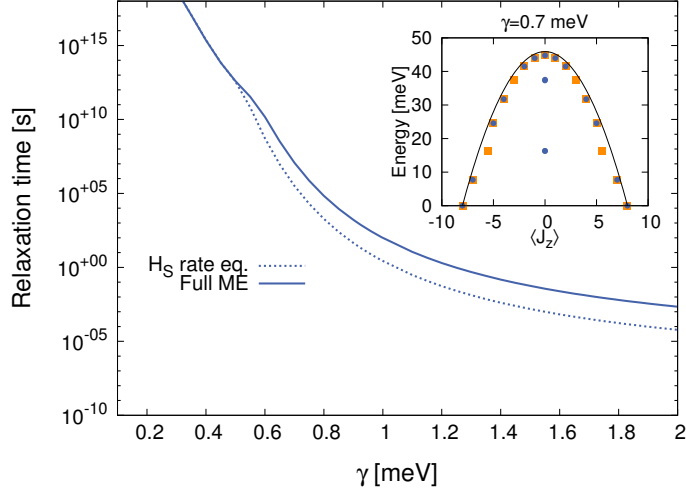


FIG. 3.14: Relaxation time  $T_1$  vs. the strength of Gaussian broadening  $\gamma$  chosen to account for further lifetime broadening effects. We compare the results obtained from the full QME (3.38) and the rate equation (3.39) based on the  $H_S$  eigenstates. We choose the parameters  $U = 5$  mV and  $B_z = 10^{-8}$  T. The insets show the  $J_z$  expectation value of the steady states and the  $H_S$  eigenstates. Reprinted with permission from [III]. Copyright (2015) by the American Physical Society.

$B_2^1$ , because the pointer states are nearly unaffected. The detailed analysis of the effect of  $B_2^1$  is impossible in the experiment because it is not independently accessible and can not be varied easily.

### 3.5.3 Noise in the Circuit

There are other possible uncontrolled perturbations on the system which could have great influence on the lifetimes, e.g., thermal noise in the electronics. We include these effects by a Gaussian broadening



### 3.5 Deviations from the Ideal Situation

---

of the electron energies. Many perturbations can eventually be described by such behavior [78]. The correlation functions  $\tilde{C}_{ij}^{\alpha\alpha'}(\hat{\omega}_{nm})$  are convoluted with the energy distribution of the electrons,

$$g(\delta E, \gamma) = 1/\sqrt{2\pi\gamma^2} \exp[-\delta E^2/(2\gamma^2)], \quad (3.48)$$

similar to the modulation broadening in Sec. 3.4.3, e.g.,

$$\tilde{C}_{+-}^{TB}(\hat{\omega}_{nm}) = c_{TB} \frac{1}{2}(1 + \eta) \int dU' \zeta(\hat{\omega}_{nm} + eU^T + eU') g(U', \gamma). \quad (3.49)$$

The Gaussian broadening is characterized by the parameter  $\gamma$ .

In Fig. 3.14 the effect of the broadening on the relaxation time  $T_1$  is shown. The exponential decrease of the lifetime is caused by the rising possibility to excite the Ho atom to the first excited state via the broader distribution of the tunneling electrons. The main transition up to  $\gamma \approx 0.6$  meV is an excitation followed by a decay to the ground state on the opposite side. Above  $\gamma \approx 0.6$  meV also sequential scattering to higher excitations get possible and the rate equations yield different results than the full QME. This can again be explained by the different  $J_z$  expectation values of the  $H_S$  eigenstates and the pointer states in the inset of Fig. 3.14. The shortcut through the 0-family states is closed by the high energy electrons. The figure is qualitatively similar to the voltage dependency in Fig. 3.8.

The order of magnitude of the relaxation times of the experiment can be reached (see Fig. 3.15) with all the perturbations to the ideal system which we considered in the beginning. The parameters are tuned to physical acceptable values. To take care of electron heating

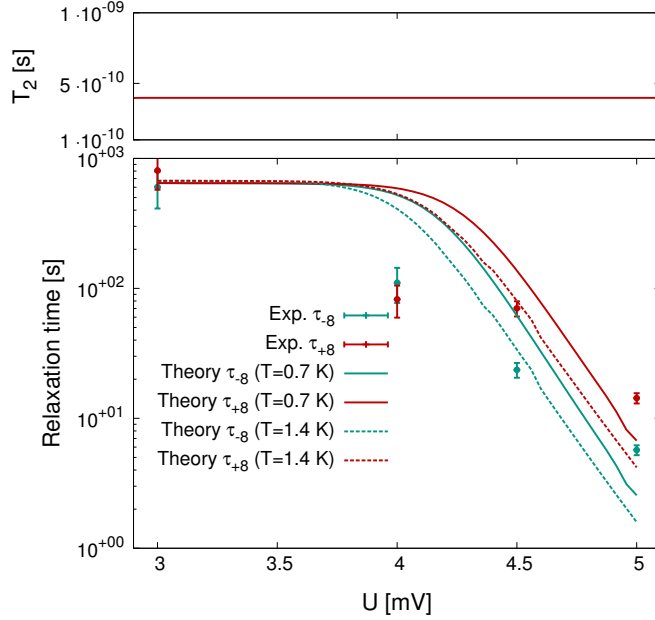


FIG. 3.15: Relaxation time  $T_1$  and decoherence time  $T_2$  of the two ground states vs. the applied voltage  $U$  at  $T = 0.7$  K and  $T = 1.4$  K for the modulation amplitude  $U_{\text{mod}} = 0.8$  mV, lifetime broadening  $\gamma = 0.95$  meV, magnetic field  $B_z = 1 \cdot 10^{-8}$  T, symmetry breaking  $B_2^1 = 4 \cdot 10^{-4}$  meV, and tip spin-polarization  $\eta = 0.15$ . We compare the results obtained from the full QME (3.38) (solid lines) and the rate equation (3.39) based on the  $H_S$  eigenstates (dashed lines). The theoretical values are compared with the state-dependent data from the experiment with error bars indicating the statistical errors of the measurement. Reprinted with permission from [III]. Copyright (2015) by the American Physical Society.

induced by the current, we plot the results for the experimental bath temperature  $T = 0.7$  K and for a higher temperature of  $T = 1.4$  K. A very high temperature alone of around  $T \approx 8$  K could be sufficient to

fit the experimental data also in agreement, but a maximum heating of  $T = 1.5$  K is expected by the experimentalists. Altogether, too few data points exist to perform a real fit of the data to determine the large number of parameters independently, but it shows that the measured data are physically explainable without questioning the model itself.

### 3.5.4 Magnetic Field Dependency

A magnetic field in  $z$ -direction breaks the time inversion symmetry and thereby the symmetry protection of the ground states. Such a magnetic field is probably present in the experiments, caused, e.g., by stray fields of the spin-polarized tip or by a deliberately applied field.

The effect of the magnetic fields on the lifetimes is strongly depending on the values of the other parameters which can be seen in comparison between Fig. 3.16 and Fig. 3.17. The main transition channel for low voltages  $U = 5$  mV with applied magnetic field is directly between the two ground states  $|\psi_8^+\rangle$  and  $|\psi_8^-\rangle$ . Fig. 3.16 shows the result for the ideal model without any modifications as defined in Sec. 3.4.2. The symmetry breaking magnetic field reduces the lifetimes drastically, even with still small rates. The simulations with the rates equations and the full QME are nearly identical.

However, with another set of parameters, the dependency can be even qualitatively completely different from Fig. 3.16 plotted in Fig. 3.17. We choose the parameters from the experimental fit in Fig. 3.15. The ground states become stabilized by the magnetic field working against the mixing of the states by the symmetry break-

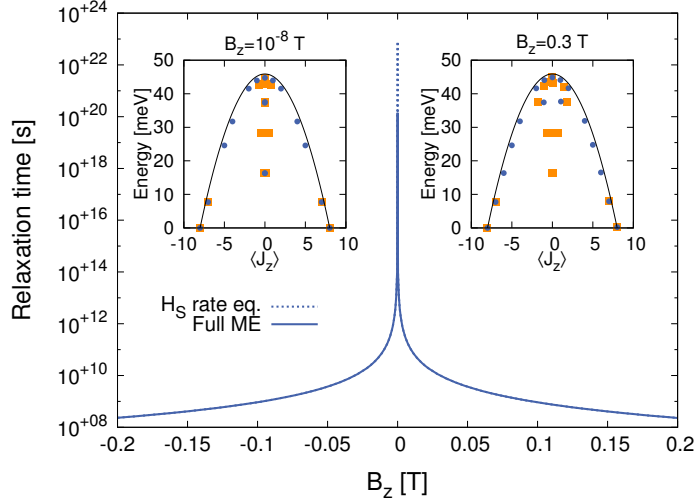


FIG. 3.16: Relaxation time  $T_1$  of the two ground states vs. a magnetic field  $B_z$  as obtained from the full QME (3.38) and the rate equations (3.39) based on  $H_S$  eigenstates. The insets show the expectation value of  $J_z$  for the two descriptions. Results for the ideal model for  $U = 5$  mV. Reprinted with permission from [III]. Copyright (2015) by the American Physical Society.

ing term  $B_2^1$ . The pointer states get closer to the  $J_z$  eigenstates with stronger magnetic fields and the lifetimes increase. This qualitatively different behavior should be a good test to examine the strength of different influences on the Ho adatom. A detailed study of the magnetic field dependency in future could give new insights into the dynamics.

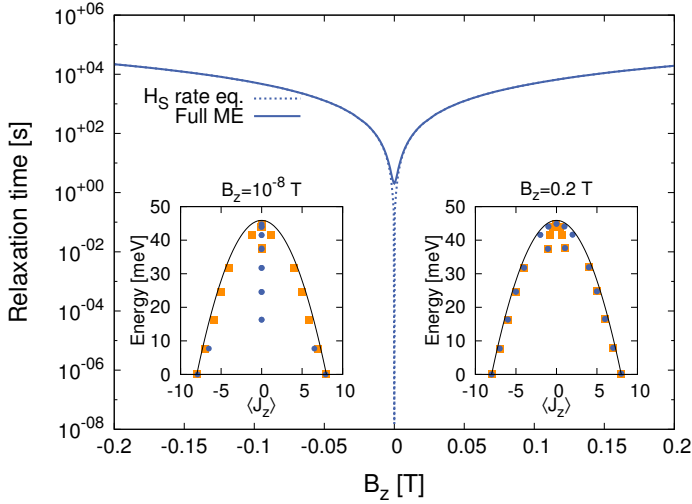


FIG. 3.17: Relaxation time  $T_1$  of the two ground states vs. a magnetic field  $B_z$  as obtained from the full QME (3.38) and the rate equations (3.39) based on  $H_S$  eigenstates. The insets show the expectation value of  $J_z$  for the two descriptions and  $U = 5$  mV. Results with symmetry-breaking and Gaussian broadening corresponding to the fits of Fig. 3.15, i.e.,  $U_{\text{mod}} = 0.8$  mV,  $\gamma = 0.95$  meV, and  $B_2^1 = 4 \cdot 10^{-4}$  meV. Reprinted with permission from [III]. Copyright (2015) by the American Physical Society.

### 3.5.5 Alternative Steven's Parameters

The properties of the adatom system are determined by the involved Steven's operators and the strength of the Steven's parameters. Our choice from the publication of Miyamachi *et al.* [I] is based on a DFT calculation and confirmed by the measured excitation spectrum. Investigations by Donati *et al.* [69] measured x-ray absorption spectroscopy (XAS) and magnetic circular dichroism (XMCD) to analyze

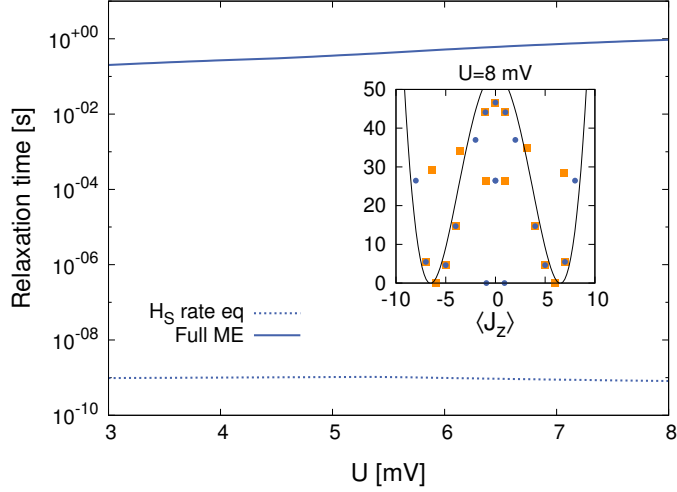


FIG. 3.18: Relaxation time  $T_1$  of the two ground states vs. the voltage  $U$  as obtained from the full QME and from the rate equations (3.39) based on  $H_S$  eigenstates for  $B_z = 10^{-8}$  T. The inset shows the expectation value of  $J_z$  for the two descriptions for  $U = 8$  mV. The black line shows the function  $f(J_z) = -140 \mu\text{eV} \cdot O_2^0 + 1 \mu\text{eV} \cdot O_4^0 + \text{const.}$ . Reprinted with permission from [III]. Copyright (2015) by the American Physical Society.

Ho on Pt(111) yielding a different set of Steven's parameters. They managed to fit their experimental results accurate with a crystal-field Hamiltonian from Eq. 3.15 and only the coefficients  $B_2^0 = -140 \mu\text{eV}$  and  $B_4^0 = 1 \mu\text{eV}$  unequal zero. On the contrary, the model proposed by Miyamachi *et al.* [I] and used in the last sections comprises all possible Steven's parameters tolerating the  $C_{3v}$  symmetry.

The ground states in the model of Donati *et al.* [69] are completely decoupled and a numerical simulation would not be possible for low

temperatures and voltages. To simulate the model from Donati *et al.* [69] we add a small  $B_4^3 \approx 0.3 \mu\text{eV}$  as described by Miyamachi *et al.* [I] to achieve finite lifetimes.

In the inset of Fig. 3.18, the new level structure of the  $H_S$  eigenstates is depicted in blue and the pointer states in orange. The stronger term  $B_4^0$ , containing the term  $J_z^4$ , bends the states with the highest  $J_z$  expectation values  $|\psi_{-8}^- \rangle$ ,  $|\psi_8^+ \rangle$ ,  $|\psi_{-7}^+ \rangle$  and  $|\psi_7^- \rangle$  upwards. The most important difference to the previous shown spectra is that the states  $|\psi_{6s}^0 \rangle$  and  $|\psi_{6a}^0 \rangle$  ( or  $|\phi_6 \rangle$  and  $|\phi_{-6} \rangle$ ) become the ground states of the system. They are strongly coupled via the term  $B_4^3$  and are not symmetry protected yielding short lifetimes in the rate equations shown in Fig. 3.18. The results of the full QME simulation are in the order of milliseconds instead of nanoseconds as in the rate equations, so the difference is even more pronounced than before. The environment-induced superselection chooses the pointer states being closer to the  $J_z$  eigenstates  $|\pm 6 \rangle$  which are much more stable than the superpositions.

Another qualitatively different feature occurring in this simulation is that higher voltages stabilize the system, because the higher states are more decoupled than the ground states  $|\phi_6 \rangle$  and  $|\phi_{-6} \rangle$ . They still have a coupling matrix element equal to zero for transitions between states of the sets  $\pm$ , i.e., are symmetry protected. The voltage dependency observed by Miyamachi *et al.* [I], where the lifetimes decrease with increasing voltages, is in stark contrast with this. It supports the use of the parameters derived by DFT calculations where only high-symmetry fcc adsorption sites on the Pt(111) surface were considered. The experiments of Donati *et al.* [69] worked with a high

coverage of Ho atoms of 0.04 monolayers with a mixture of hcp and fcc adatoms. A detailed analysis is needed to answer if this is the reason for the differing results. First unpublished data from the experimental group of Brune in Lausanne with very low coverage indicate that the coverage has no influence on their results.

### 3.6 Decoherence Time $T_2$

In quantum mechanical devices, e.g., qubits, the decoherence time is essential for the successful operation of the device. The  $T_2$  is defined as the decay time of the phase of a coherent superposition of the logical basis states. In our case, this is the phase between the ground states of the Ho adatom  $|\psi_8^+\rangle$  and  $|\psi_8^-\rangle$ . The phase information is given by the off-diagonal matrix element  $\rho_{+8-8}$  of the reduced density matrix. The decay rate of this reduced density matrix element corresponds to the matrix element  $\mathcal{M}_{8-8\rightarrow 8-8}$  of the QME in the form of Eq. 3.27,

$$\begin{aligned} 1/T_2 &= -\mathcal{M}_{8-8\rightarrow 8-8} \\ &\approx 4c_{TB} \langle \psi_8^+ | J_z | \psi_8^+ \rangle \langle \psi_8^- | J_z | \psi_8^- \rangle \zeta(-eU) \\ &\approx 264 c_{TB} eU. \end{aligned} \quad (3.50)$$

In the previous Figs. 3.8, 3.10, 3.11 and 3.15  $T_2$  times are plotted for different parameters. The result is that  $T_2$  is mainly depending on the number of scattered electrons, i.e., the current. For the dephasing of the superposition is no energy needed and practically every electron which tunnels on or from the Ho adatom causes decoher-



ence, independent of the other parameters. Therefore, if the current is kept constant by not changing  $U$  or by adjusting the coupling constant  $c_{TB}(U)$  the decoherence time is fixed. Only in the Figs. 3.8 and 3.10,  $T_2$  is decreasing proportionally to  $1/U$  with increasing  $U$ . But in all plots, it turns out that  $T_2$  is short, i.e., in the order of  $10^{-10}$  s. Thus, the system is probably not usable in this form as a qubit.  $T_2$  needs to be compared with the time required to operate the qubit, i.e., to execute a logical gate. At the moment, it is totally unclear how such a gate would look like in this system. Furthermore, according to our investigations,  $T_2$  is independent of the symmetry breaking term  $B_2^1$ , the broadening  $\gamma$  or the magnetic field  $B_z$ .

One could argue that an operating qubit is not permanently coupled to a tip or another bias current and if  $T_2$  is only depending on the current, this system could for  $U = 0$  still be an operating qubit. Without the bias current, all the possible coupling terms to the environments  $\tilde{C}_{\nu\nu'}^{\alpha\alpha'}(\pm\hat{\omega}_{nm})$  with  $\{\nu, \nu'\} = \{T, B\}$  are without any precognition relevant. In the Born-Markov approximation, the environments are additive and  $T_2$  can be estimated by

$$\begin{aligned}
 1/T_2 &= -M_{8-8 \rightarrow 8-8} \\
 &\approx 4 \left( \sum_{\nu\nu'} c_{\nu\nu'} \right) \langle \psi_8^+ | J_z | \psi_8^+ \rangle \langle \psi_{-8}^- | J_z | \psi_{-8}^- \rangle \zeta(0) \\
 &\approx 264 k_B T \sum_{\nu\nu'} c_{\nu\nu'}.
 \end{aligned} \tag{3.51}$$

For coupled environments with coupling strengths in the order of magnitude found in our investigation of the current in Sec. 3.4.1  $\sum_{\nu\nu'} c_{\nu\nu'} \approx 10^6 (\text{meV s})^{-1}$  and a temperature of  $T = 1$  K, the deco-

herence time is approximately  $10^{-8}$  s. Therefore, also in the best case scenario,  $T_2$  is still very small.

### 3.7 Initialization

The long lifetimes reported so far are one key ingredient for using the Ho adatom as memory. Another important part is the writing process or more general, the initialization of one of the ground states. It would also be useful for experiments with defined initial state. The different parameters should be modified to the point that high fidelity initialization can be accomplished. This is achievable in our setting by voltage pulsing the system with the spin-polarized current for a time  $t_p$  and by letting the system afterwards relax for  $t_r$ . The relaxation time  $t_r$  should be large enough that all excitations decay in the ground states and we choose  $t_r = 1 \mu\text{s}$  for all simulations. As the important quantity, we look at the switching probability  $S_{-8 \rightarrow 8}(U, t_p)$ . It depends on the pulse voltage strength  $U$  and the pulse length  $t_p$ .  $S_{-8 \rightarrow 8}(U, t_p)$  is defined as the probability to end after the pulse in state  $|\psi_8^+\rangle$  if you start in state  $|\psi_{-8}^-\rangle$ . If this probability is close to one for one parameter set and close to the zero for the contrary writing process, a good initialization of a wanted state is possible.

We use the full QME model and parameters as in the case of the comparison with the experiment in Fig. 3.15, but without the  $c_{TB}(U)$  correction (because we want to pulse the system). According to this comparison, we neglect the scattering of bulk electrons. The switching probability  $S_{-8 \rightarrow 8}(U, t_p)$  is plotted vs. the applied voltage  $U$  for different spin-polarizations  $\eta$  of the tip and a pulse time

### 3.7 Initialization

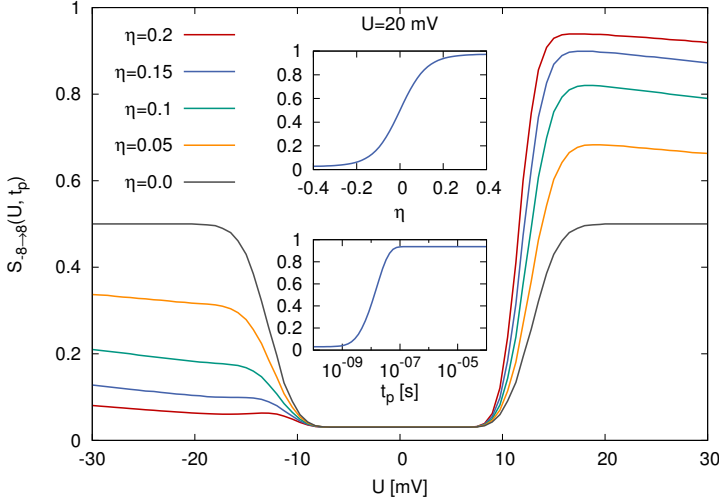


FIG. 3.19: The probability for switching from  $|\psi_{-8}^-\rangle$  to  $|\psi_8^+\rangle$  vs. the applied pulse voltage for different values of the tip polarization  $\eta$  and a pulse time of  $t_p = 2.5 \cdot 10^{-7}$  s. The upper inset shows the switching probability vs. the tip polarization for pulse strength  $U = 20$  mV and pulse time  $t_p = 2.5 \cdot 10^{-7}$  s. The lower inset shows the dependency on the pulse time  $t_p$  for pulse strength of  $U = 20$  mV and  $\eta = 0.2$ . Reprinted with permission from [III]. Copyright (2015) by the American Physical Society.

$t_p = 2.5 \cdot 10^{-7}$  s in Fig. 3.19. As one could expect, for higher polarizations higher fidelities can be reached. In the regime above  $U \approx 20$  mV and strong polarization, the switching probability becomes close to one. Furthermore, a pulse with the opposite voltage strength  $U < -20$  mV does not change the population of the state  $|\psi_{-8}\rangle$ , the switching probability remains small. Combined, this means that both states can be prepared by strong pulses and by a

better polarization of the tip. One disadvantage of high polarizations is the enhancement of the stray fields belonging to the tip.

Voltage pulses in the range of  $-10$  mV to  $10$  mV leave the system unchanged. The pulse time and corresponding number of electrons with high energy are not enough to cause a transition between the states. The plots for  $\eta \neq 0$  show all a small maximum between  $10$  mV and  $20$  mV. The population for no polarization  $\eta = 0$  voltage pulses above  $U \approx 15$  mV is equally distributed on both ground states. There is no preferred state of the system without polarization.

The dependency of the fidelity on the tip polarization  $\eta$  is shown in the upper inset of Fig. 3.19 for the approximately best conditions  $U = 20$  mV and pulse time  $t_p = 2.5 \cdot 10^{-7}$  s. This leads again to the conclusion that the higher the polarization the better the initialization. By looking at the dependency of the fidelity on the pulse time  $t_p$  in the lower inset of Fig. 3.19, we can estimate the number of electrons needed for a good initialization process, i.e., switching probability close to 1. The voltage is again near the optimum of  $U = 20$  mV producing a current of  $I_{\text{Th}}(20 \text{ mV}) \approx 0.75$  nA. We can see from the plot that the pulse time has to be longer than approximately  $250$  ns. The number of electrons needed to flip the ground state with a high fidelity is

$$N_e = \frac{I_{\text{Th}}(20 \text{ mV}) \cdot t_p^{\text{min}}}{e} \approx 1100, \quad (3.52)$$

with  $e$  the elementary charge. This could be tested in the experiments by changing the tip distance, i.e., changing the number of tunneling electrons.

### 3.7 Initialization

---

In summary, we propose an initialization process which is fast, i.e., pulse times of a few hundreds nanoseconds, and which gives high fidelities with the assumption of good tip polarizations. But it is important to consider the effect of the coupling strength  $c_{TB}$  which has direct impact on the required pulse time  $t_p^{\min}$ .



# 4 Chapter

---

## Double Quantum Dots

The second system we analyze with the QME is a double quantum dot (DQD) coupled to a microwave oscillator. Our method for solving the QME allows us to investigate DQDs with multiple levels in each dot and coupled to different environments simultaneously. To be more specific, the DQD is connected to two electronic leads and a bath of phonons. This leads to incoherent and coherent transitions in the DQD with rich and interesting dynamics. We will investigate different possible processes and lasing situations. In particular, we have a more detailed look at the situation sketched in the introduction in Fig. 1.2 b) and the influence of the phonon coupling.

This chapter is based on the publication Karlewski *et al.* [V] which will not be further cited in this part.

## 4.1 The DQD Hamiltonian and the QME

The QME, defined by the Hamiltonian of the system, the baths and the coupling between them, can be solved with the method used in the previous chapters. In the first part, we will therefore show in detail how the DQD coupled to the oscillator and the electronic leads can be described in this framework. With this in mind, we introduce the additional phonon bath and reproduce the derivation of the QME with the new environment.

### 4.1.1 DQD Coupled to a Microwave Oscillator

The Hamiltonian of the DQD system with discrete energy levels  $\varepsilon_{\alpha i}$  in the left and in the right dot ( $\alpha = L, R$ ) coupled to a microwave oscillator and electronic leads is

$$H = H_{\text{DQD}} + H_{\text{osc}} + H_{\text{DQD-osc}} + H_{\text{C}} + H_{\text{leads}}. \quad (4.1)$$

The DQD Hamiltonian  $H_{\text{DQD}}$  describes the two semiconducting islands

$$\begin{aligned} H_{\text{DQD}} = & \sum_{\alpha=L,R} \sum_i \varepsilon_{\alpha i} n_{\alpha i} + \sum_{ij} \left( t_{ij} d_{Li}^\dagger d_{Rj} + \text{h.c.} \right) \\ & + U_1 \sum_{\substack{\alpha=L,R \\ i \neq j}} n_{\alpha i} n_{\alpha j} + U_2 \sum_{ij} n_{Li} n_{Rj}, \end{aligned} \quad (4.2)$$



with  $d_{\alpha i}^\dagger$  ( $d_{\alpha i}$ ) the creation (annihilation) operator and  $n_{\alpha i} = d_{\alpha i}^\dagger d_{\alpha i}$  the occupation of the  $i^{\text{th}}$  level of dot  $\alpha$  (left or right). The intra-dot and inter-dot Coulomb energy scales are  $U_1$  and  $U_2$ , respectively. The electrons can tunnel between the dots with amplitude  $t_{ij}$  which provides a transition channel of the current and additionally generates hybridization between the dot states.

We assume a single-mode oscillator with eigenfrequency  $\omega_0$ . This is, e.g., a very good description of the superconducting transmission line resonator [15],

$$H_{\text{osc}} = \omega_0 a^\dagger a. \quad (4.3)$$

The oscillator is coupled via the occupation of the left dot levels with an energy-independent coupling constant  $g$ ,

$$H_{\text{DQD-osc}} = g(a + a^\dagger) \sum_i n_{Li}. \quad (4.4)$$

In the QME we have to define our system of interest which is in our setting the combination of these three Hamiltonians  $H_S = H_{\text{DQD}} + H_{\text{osc}} + H_{\text{DQD-osc}}$ . To simplify the problem we assume large Coulomb energies  $U_1$  and  $U_2$  and reduce the Hilbert-space to at most one electron in the DQD, i.e., the three possibilities: one electron in the left dot or right dot or no electron in the DQD.

The electronic environments are given by the left and right lead which we assume to be coupled weakly and equal for both leads,

$\gamma_L = \gamma_R = \gamma$ , i.e.

$$H_C = \gamma \sum_{\substack{\alpha=L,R \\ ik}} \left( d_{\alpha i}^\dagger c_{\alpha k} + \text{h.c.} \right). \quad (4.5)$$

The coupling strength  $\gamma$  defines the tunneling rate of the electrons into the DQD

$$\Gamma = 2\pi N_0(E_f)\gamma^2, \quad (4.6)$$

where  $N_0(E_f)$  is the electron density of states at the Fermi edge. The tunneling rate  $\Gamma$  is the essential element of the overall current through the DQD and appears as a scaling factor of the current.

Similar to the Ho adatom, we assume that the electronic leads, in the case of Ho the tip and the bulk, are in equilibrium. The difference between the two systems (Ho and DQD) in the QME is the tunneling of electrons into the DQD system but not through the DQD. They stay there. This is reflected by the equilibrium Green's functions of the leads which are

$$\begin{aligned} G_{\alpha k}^<(t) &= i \langle c_{\alpha k}^\dagger(0) c_{\alpha k}(t) \rangle = i f(\epsilon_{\alpha k} + eV_\alpha) e^{-i(\epsilon_{\alpha k} + eV_\alpha)t}, \\ G_{\alpha k}^>(t) &= -i \langle c_{\alpha k}(t) c_{\alpha k}^\dagger(0) \rangle = -i [1 - f(\epsilon_{\alpha k} + eV_\alpha)] e^{-i(\epsilon_{\alpha k} + eV_\alpha)t}, \end{aligned} \quad (4.7)$$

with the Fermi-Dirac distribution function  $f(\epsilon)$ . Mind the small differences between the Green's function definitions and the correlation functions given by the Eqs. 3.14 of the Ho QME, e.g., the complex factor  $i$  and the appearance of the Fermi-Dirac distribution only once

not twice as in the correlation functions.

In accordance to the previous chapters, we are interested in properties of the small quantum system encoded in the reduced density matrix  $\rho(t)$  with the environment traced out. As mentioned before, this means in this setting that the DQD and oscillator states are important and the electronic leads enter through their Green's functions. We assume that the conditions for the Born-Markov approximation explained in chapter 2 are fulfilled, i.e., weak coupling to the electrodes and large decay rates of the correlations inside the leads as compared to typical system dynamic time scales. Therefore, we can use the QME in the shorthand notation (cf. Eq. (2.11))

$$\frac{\partial}{\partial t}\rho(t) = \mathcal{L}\rho(t), \quad (4.8)$$

with Liouvillian  $\mathcal{L} = \mathcal{L}_S + \mathcal{L}_C$  defined as

$$\begin{aligned} \mathcal{L}_S\rho(t) &= i[\rho(t), H_S], \\ \mathcal{L}_C\rho(t) &= -\int_{-\infty}^t dt' \langle [H_C(t), [H_C(t'), \rho(t)]] \rangle_{LR}. \end{aligned} \quad (4.9)$$

The Liouvillian  $\mathcal{L}$  describes a similar object as the superoperator  $\mathcal{M}$  of chapter 3, but still in the matrix dimension of  $\rho(t)$  and not in the enlarged space of  $\vec{\rho}(t)$ . As usual, we trace out the equilibrium leads  $\langle \cdot \rangle_{LR} = \text{Tr}_{LR} \{ \cdot \rho_L \rho_R \}$ .

We will transform Eq. (4.8) into a form that can be written with  $\vec{\rho}(t)$  and perform the same analysis used for the Ho adatom. So, we

introduce the Laplace transforms of the Green's functions

$$\begin{aligned}
 G_{\alpha k}^<(\omega) &= \int_{-\infty}^0 dt G_{\alpha k}^<(t) e^{i\omega t + \eta t} = \frac{f(\epsilon_{\alpha k} + eV_{\alpha})}{\omega - (\epsilon_{\alpha k} + eV_{\alpha}) - i\eta}, \\
 G_{\alpha k}^>(\omega) &= \int_{-\infty}^0 dt G_{\alpha k}^>(t) e^{i\omega t + \eta t} = -\frac{1 - f(\epsilon_{\alpha k} + eV_{\alpha})}{\omega + \epsilon_{\alpha k} + eV_{\alpha} - i\eta}, \quad (4.10)
 \end{aligned}$$

with the small parameter  $\eta = 0_+$  introduced for convergence. We follow our protocol, change into the eigenbasis of the system Hamiltonian  $H_S$ , i.e.,  $V^\dagger H_S V = \text{diag}(E_1, \dots, E_N)$  and introduce the notation  $\bar{A} = V^\dagger A V$ . The aim is to evaluate the Green's functions at the eigenenergies of the Hamiltonian. The dissipative part of the Liouvillian  $\mathcal{L}_C$  turns into [II] [74]

$$\begin{aligned}
 V^\dagger \mathcal{L}_C \rho(t) V &= i\gamma^2 \sum_{\substack{\alpha=L,R \\ ijk}} \\
 &\left\{ \bar{d}_{\alpha i} \left[ G_{\alpha k}^<(\hat{\omega}) * \bar{d}_{\alpha j}^\dagger \right] \bar{\rho}(t) + \bar{d}_{\alpha i}^\dagger \left[ G_{\alpha k}^>(\hat{\omega})^\dagger * \bar{d}_{\alpha j} \right] \bar{\rho}(t) \right. \\
 &\quad + \bar{d}_{\alpha i} \bar{\rho}(t) \left[ G_{\alpha k}^>(\hat{\omega}) * \bar{d}_{\alpha j}^\dagger \right] + \bar{d}_{\alpha i}^\dagger \bar{\rho}(t) \left[ G_{\alpha k}^<(\hat{\omega})^\dagger * \bar{d}_{\alpha j} \right] \\
 &\quad - \left[ G_{\alpha k}^>(\hat{\omega})^\dagger * \bar{d}_{\alpha i} \right] \bar{\rho}(t) \bar{d}_{\alpha j}^\dagger - \left[ G_{\alpha k}^<(\hat{\omega}) * \bar{d}_{\alpha i}^\dagger \right] \bar{\rho}(t) \bar{d}_{\alpha j} \\
 &\quad \left. - \bar{\rho}(t) \left[ G_{\alpha k}^<(\hat{\omega})^\dagger * \bar{d}_{\alpha i} \right] \bar{d}_{\alpha j}^\dagger - \bar{\rho}(t) \left[ G_{\alpha k}^>(\hat{\omega}) * \bar{d}_{\alpha i}^\dagger \right] \bar{d}_{\alpha j} \right\}. \quad (4.11)
 \end{aligned}$$

The product, denoted by the symbol  $*$ , represents the direct or Hada-

matrix product between two matrices, e.g.,

$$\left(G_{\alpha k}^{\gt}(\hat{\omega})^\dagger * \bar{d}_{\alpha j}\right)_{nm} = \left(G_{\alpha k}^{\gt}(\hat{\omega})\right)_{mn}^* \left(\bar{d}_{\alpha j}\right)_{nm}. \quad (4.12)$$

Additionally, we use again the matrix  $\hat{\omega}$  with elements  $\hat{\omega}_{nm} = E_n - E_m$ . In this form the QME can be easily written in the enlarged Hilbert-space  $\dot{\bar{\rho}}(t) = \mathcal{M}\bar{\rho}(t)$ , which is very useful for numerics. We are interested in the steady state  $\rho_{\text{st}}$  properties of the system given by the corresponding eigenstate of  $\mathcal{M}$  with the eigenvalue  $m_0 = 0$ . For details of this derivation see Appendix A.1 and section 3.3.1.

The oscillator is exposed to the environment and excitations decay into the surroundings of the oscillator with a decay rate  $\kappa$ . This can be treated as an additive term in the QME by the Liouvillian

$$\mathcal{L}_\kappa \rho(t) = \frac{\kappa}{2} \left( 2a\rho(t)a^\dagger - [a^\dagger a, \rho(t)]_+ \right), \quad (4.13)$$

where  $[\cdot, \cdot]_+$  is the anti-commutator.

The focus of our investigation of the system will be the analysis of the current through the DQD and the number of photons in the oscillator, as well as their statistical properties. Both are experimentally accessible and show characteristic behavior in the lasing situation. The total current is defined as the change in the number of electrons in the left or right lead (which are the same in the steady state solution). Without loss of generality we choose the left lead electron number  $N_L(t) = \sum_k c_{Lk}^\dagger(t)c_{Lk}(t)$ . The time evolution of this operator is given by the Heisenberg equation  $\dot{N}_L(t) = i[H(t), N_L(t)]$ . All parts of the total Hamiltonian except the coupling  $H_C(t)$  commute

with  $N_L(t)$  and the resulting current in the steady state through the left tunnel junction is

$$\begin{aligned} \langle I_L \rangle &= e \frac{d}{dt} \langle N_L(t) \rangle \Big|_{t \rightarrow \infty} = ie \langle [H(t), N_L(t)] \rangle \Big|_{t \rightarrow \infty} \\ &= 4e\gamma^2 \sum_{kij} \text{Tr} \left\{ \text{Im} \left[ -\bar{d}_{Li} \left( G_{Lk}^<(\hat{\omega}) * \bar{d}_{Li}^\dagger \right) \bar{\rho}_{\text{st}} \right. \right. \\ &\quad \left. \left. + \bar{d}_{Li}^\dagger \left( \bar{d}_{Lj} * G_{Lk}^>(\hat{\omega})^\dagger \right) \bar{\rho}_{\text{st}} \right] \right\}. \end{aligned} \quad (4.14)$$

The important observables for the oscillator are the number of photons and the distribution of these photons described by the Fano factor [80]. To be more specific, the Fano factor gives a quantitative measure for the statistical dispersion of a probability distribution. In particular, if the Fano factor equals 1, the distribution is a Poisson distribution. A Fano factor smaller (larger) than 1 means that the distribution is more narrow (wider) than the Poisson distribution known as sub-Poissonian (super-Poissonian). The average number of photons and the Fano factor are both defined via the photon number operator  $N_{\text{Ph}} = a^\dagger a$

$$\langle N_{\text{Ph}} \rangle = \text{Tr} \left\{ a^\dagger a \rho_{\text{st}} \right\} \quad (4.15)$$

$$F_a = \left( \langle N_{\text{Ph}}^2 \rangle - \langle N_{\text{Ph}} \rangle^2 \right) / \langle N_{\text{Ph}} \rangle. \quad (4.16)$$

We are interested in the possible lasing states of the oscillator. These display, on the one hand, a characteristic narrow peak in the number of photons. On the other hand, the Fano factor shows typical indications of the lasing state, i.e., it is approximately  $F_a \approx 1 + \langle N_{\text{Ph}} \rangle$  in the non-lasing regime, whereas in the transition to the lasing regime

the Fano factor should decrease. In the ideal lasing model, the photon generation events are discrete and independent giving a Poisson distribution with  $F_a = 1$ . In the more complex systems of our studies and in real systems, deviations from the ideal situation are possible. In particular, a sub-Poissonian distribution of the radiation field  $F_a < 1$  is achievable which is sometimes called *squeezed light* [41].

### 4.1.2 Coupling to a Phonon Bath

The phonons coupled to the DQD are an additional dissipative bath. We assume very low temperatures, therefore the phonons will remove energy from the system. The phonon bath is added to the QME in the Born-Markov approximation in the same manner as the electronic leads with small adjustments, e.g., the bosonic character of the phonons and the specific coupling. With the new dissipation channel, transitions inside the DQD can be increased and the total current through the DQD is influenced by the phonons of the semi-conducting bulk material [44, 49, 51]. First, we have to define the kind of coupling between the phonons and the electrons in the DQD. The dominant coupling in this system is the piezoelectric interaction as presented in Ref. [81] and given by

$$H_{\text{el-ph}} = g_{\text{el-ph}} \sum_{\alpha ik} n_{\alpha i} \varphi_{\alpha k}, \quad (4.17)$$

with phonon operators  $\varphi_{\alpha k} = b_{\alpha k} + b_{\alpha -k}^\dagger$  and the coupling constant  $g_{\text{el-ph}}$ , which is considered to be energy-independent. The operators  $b_{\alpha k}^\dagger$  ( $b_{\alpha k}$ ) are now *bosonic* creation (annihilation) operators of the

phonons. Following the procedure from the electron coupling, we use the phonon Green's functions for the phonon-bath in equilibrium

$$\begin{aligned} D_{\alpha k}^<(t) &= i \langle \varphi_{\alpha k}(0) \varphi_{\alpha k}(t) \rangle = i n_B(\omega_{\alpha k}) e^{-i\omega_{\alpha k} t} + i [1 + n_B(\omega_{\alpha k})] e^{i\omega_{\alpha k} t}, \\ D_{\alpha k}^>(t) &= -i \langle \varphi_{\alpha k}(t) \varphi_{\alpha k}(0) \rangle \\ &= -i n_B(\omega_{\alpha k}) e^{i\omega_{\alpha k} t} - i [1 + n_B(\omega_{\alpha k})] e^{-i\omega_{\alpha k} t}, \end{aligned} \quad (4.18)$$

with the Bose-Einstein distribution  $n_B(\omega)$ . The respective Laplace transforms are

$$\begin{aligned} D_{\alpha k}^<(\omega) &= \frac{n_B(\omega_{\alpha k})}{\omega - \omega_{\alpha k} - i\eta} + \frac{1 + n_B(\omega_{\alpha k})}{\omega + \omega_{\alpha k} - i\eta}, \\ D_{\alpha k}^>(\omega) &= -\frac{n_B(\omega_{\alpha k})}{\omega + \omega_{\alpha k} - i\eta} - \frac{1 + n_B(\omega_{\alpha k})}{\omega - \omega_{\alpha k} - i\eta}. \end{aligned} \quad (4.19)$$

With the coupling Hamilton operator  $H_{\text{el-ph}}$  and the Green's functions  $D_{\alpha j}^{\lessgtr}(\omega)$ , the Liouvillian of the phonon coupling is given by

$$\begin{aligned} V^\dagger \mathcal{L}_{\text{el-ph}} \rho_{\text{st}} V &= i g_{\text{el-ph}}^2 \sum_{\alpha i j k} \\ &\quad \times \left\{ \bar{n}_{\alpha i} \left[ D_{\alpha k}^<(\hat{\omega}) * \bar{n}_{\alpha j} \right] \bar{\rho}_{\text{st}} - \bar{n}_{\alpha i} \bar{\rho}_{\text{st}} \left[ D_{\alpha k}^>(\hat{\omega}) * \bar{n}_{\alpha j} \right] \right. \\ &\quad \left. - \left[ D_{\alpha k}^<(\hat{\omega}) * \bar{n}_{\alpha i} \right] \bar{\rho}_{\text{st}} \bar{n}_{\alpha j} - \bar{\rho}_{\text{st}} \left[ D_{\alpha k}^>(\hat{\omega}) * \bar{n}_{\alpha i} \right] \bar{n}_{\alpha k} \right\}. \end{aligned} \quad (4.20)$$

In the usual way, we convert the sum over  $k$  in an integral with the effective phonon density of states  $F(\omega)$ .

Altogether, the QME, describing our system, is the sum of the coherent evolution of the DQD coupled to the oscillator and the dissipative parts due to electron tunneling, phonon coupling and decay



of the oscillator

$$\dot{\rho}(t) = \mathcal{L}\rho(t) = (\mathcal{L}_S + \mathcal{L}_C + \mathcal{L}_{el-ph} + \mathcal{L}_\kappa) \rho(t). \quad (4.21)$$

The observables current, number of photons and Fano factor defined in section 4.1.1 depend on the stationary solution of the equation, i.e.,  $\mathcal{L}\rho_{st} = 0$ . This is the basis of the following numerical investigation in the next section in which we set the free parameters to values suggested by recent experiments.

## 4.2 Lasing in the Multi-Level System

With more than one level in each dot, several resonance conditions with the microwave oscillator are possible. We will restrict ourselves to a system with two levels in each dot qualitatively including all different lasing situations which can occur. An overview of the different possible resonant transitions is presented in section 4.2.1. In section 4.2.2, we have a closer look at the transition sketched in Fig. 1.2 b).

### 4.2.1 Overview of Different Lasing Situations

In the experiments of Liu *et al.* [49] the theoretical predicted lasing state in the system with one level in each dot has been confirmed. A small fly in the ointment: the chosen coupling strength to the leads is not covered by the QME described here and also the reached number of photons (8000) is out of scope of the numerical feasible range. Nevertheless, the encountered parameters are

our starting point with small adjustments to better emphasize our findings. The central quantity of the system is the oscillator frequency which  $f_0 = 7.8 \text{ GHz} = \omega_0/2\pi$ , i.e.,  $\omega_0 = 0.032 \text{ meV}$  in the experiment. All other parameters will be normalized with this energy reference scale. The multiple levels of the DQD lie all inside the range of the applied voltages at the left and right lead, i.e.,  $eV_L > \epsilon_{Li}, \epsilon_{Ri} > eV_R$ , to suppress any effect of too low applied voltages. We set the coupling of the left dot to the oscillator to  $g = 0.02\omega_0$ . This is an order of magnitude stronger than determined by the experiment to better highlight our different findings. For the same reason, we consider a very high-quality microwave oscillator with  $\kappa = 10^{-6}\omega_0$  corresponding to a quality factor  $Q = 2 \cdot 10^6$ . Such a quality has been achieved in purely superconducting systems [82], while in semiconductor-superconductor heterostructures only values reaching  $Q \approx 10^4$  have been reported [83].

The base temperature of the experiment was 10 mK, but e.g., the current heats the device and we include this by choosing a temperature of  $T = 100 \text{ mK} = 0.27\omega_0$ . Furthermore, the authors of Ref. [49] managed to fit the effective phonon density of states  $F(\alpha)(\omega) = \sum_{\alpha k} \delta(\omega - \omega_{\alpha k})$  and which is approximately

$$F(\omega) = \frac{(\omega/\Omega_0)^2}{[\alpha_1 + (\omega/\Omega_0)^2]^{\alpha_2/2+1}} \quad (4.22)$$

with the parameters  $\alpha_1 = 0.02$ ,  $\alpha_2 = 1.4$ , and  $\Omega_0 = 0.4 \text{ meV}$ .

As mentioned before, our investigation focuses on the model with two levels in each dot lying in the window between the applied potentials. One example is the situation depicted in Fig. 1.2 b) of the

introduction. The energy differences of the two levels in the left and right dot are  $\varepsilon_{L2} - \varepsilon_{L1} = \Delta_L \omega_0$  and  $\varepsilon_{R2} - \varepsilon_{R1} = \Delta_R \omega_0$ . In general, the energy splittings differ from the oscillator frequency ( $\Delta_{L/R} \neq 1$ ), and they differ from each other ( $\Delta_L \neq \Delta_R$ ). We assume that the dot levels can be shifted relative to each other by applied gate voltages in a way that the energy difference between the two lower levels is  $\varepsilon_{L1} - \varepsilon_{R1} = \varepsilon$ , whereas the energy difference of the dots  $\Delta_{L/R}$  remain constant. For simplicity we assume that the tunneling strength  $t_{ij}$  between the right and left dot levels is identical for all levels  $t_{ij} = t$  and  $i, j = \{1, 2\}$ . The tunneling strength of the electronic leads is  $\Gamma = 10^{-6} \omega_0$ .

By varying the relative shift  $\varepsilon$ , all the possible resonance situations between left and right dot levels can be realized. This is shown in Fig. 4.1 for the four levels of our model. The number of photons  $\langle N_{\text{Ph}} \rangle$  displayed in the upper part peaks every time a downwards transition in the DQD fulfills the lasing condition. As consequence, the DQD emits photons in the microwave oscillator. The bias voltage produces the needed population inversion, i.e., an occupation of the energetically higher states. We illustrate for each of the resonances the corresponding energy level structure in the small sketches. Blue wavy arrows indicate the emission of a photon, a red curved arrow the tunneling of an electron and a gray dashed arrow tunneling induced by a dissipative emission of a phonon.

The simplest lasing situation in the multi-level system is similar to the single level in each dot lasing scenario sketched in Fig. 1.2 a) [41]. A lasing transition occurs when a state in the left dot is exactly  $\omega_0$  higher than a right dot level. This is fulfilled by the

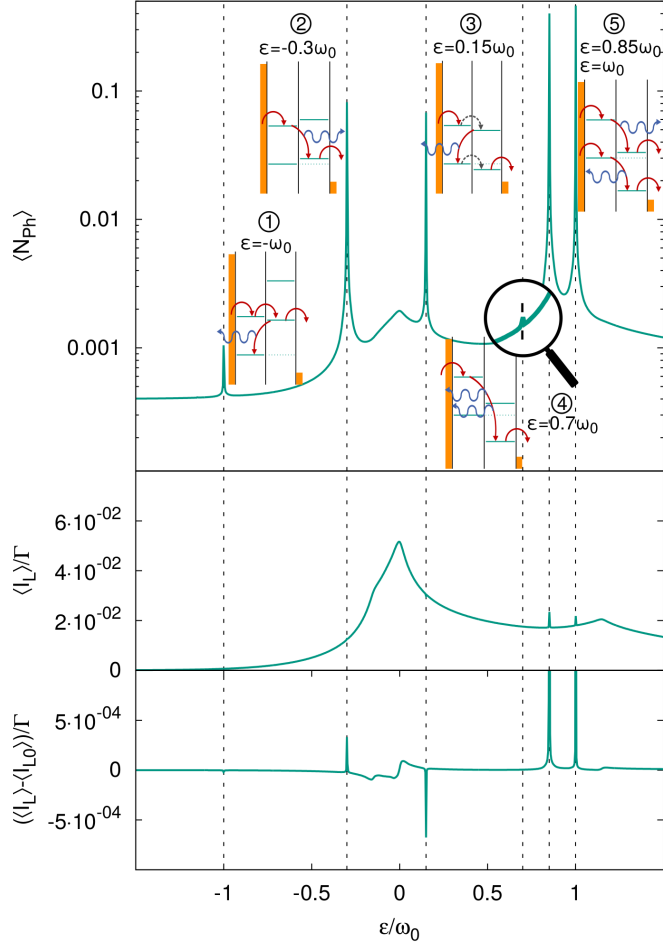


FIG. 4.1: Top: The photon expectation value  $\langle N_{\text{Ph}} \rangle$  vs. the detuning  $\varepsilon$  with  $\Delta_L = 1.3$ ,  $\Delta_R = 1.15$ . The parameters are  $t = 0.01\omega_0$  and  $g_{\text{el-ph}} = 0.01\omega_0$ . Mid: The current through the left lead  $\langle I_L \rangle / \Gamma$  vs. the detuning  $\varepsilon$ . Bottom: The difference between the current through the left lead with ( $g = 0.01\omega_0$ ) and without ( $g = 0$ ) coupling to the oscillator. The current is enhanced or decreased in the resonance situations. Reprinted with permission of Ref. [V]. Copyright (2015) by the American Physical Society.

two peaks at the right side of Fig. 4.1 which are at  $\varepsilon = \omega_0$  and  $\varepsilon = (1 - \Delta_L + \Delta_R)\omega_0$  (corresponding to the sketch labeled by (5)). The two lower or the two higher dot states are in resonance with the oscillator. The same applies for the peak labeled by (2) at  $\varepsilon = (1 - \Delta_L)\omega_0$ . Here, the upper left and the lower right dot level satisfy the resonance condition. All the exact solutions of the resonance conditions for  $\varepsilon$  in this overview part are valid for small tunneling couplings  $t \ll \Delta_{L/R}$  between the dots. Otherwise, the hybridization of the states have to be taken into account which is done in the investigation of the tunneling dependency in section 4.2.2.

More complex and qualitatively different is the lasing resonance at  $\varepsilon = (\Delta_R - 1)\omega_0$  labeled by (3). Sequential hopping of the electron among all four DQD levels eventually produces a photon in the resonator during the transport through the DQD. In this cascade of transitions three different steps happen. First, the phonon induced incoherent hopping from the higher left dot level to the higher right dot level. Second, the resonant transition with the microwave oscillator against the main current direction to the lower left dot level. Third, again an incoherent transition with the emission of a phonon to the right lower dot level.

The small peak labeled (1) is similar. The resonant transition occurs from the lower right dot level to the lower left dot level. This needs first a hopping from the higher level of the left dot to the lower level of the right dot by tunneling or incoherent transition with emission of a phonon. But the electron is trapped in the left dot and because of the high Coulomb energies the transport through the dot is blocked. A higher order or thermally activated process is needed

to overcome the barrier to the lower right dot level and opens again the DQD for the next electron. Therefore, the peak is small and this is also the reason for the asymmetry between positive and negative  $\varepsilon$ .

Our model is further able to account for more than one photon processes which can be seen at the position  $\varepsilon = (2 - \Delta_L)\omega_0$  (labeled by (4)). In this case, it is a two-photon process  $\epsilon_{L2} - \epsilon_{R1} = 2\omega_0$  strongly depending on the coupling strength between the DQD and the microwave oscillator. For our choice it is very small but becomes stronger with increasing coupling strength.

With Eq. (4.14) the current through the DQD can be simulated and is shown in the central plot of Fig. 4.1 vs.  $\varepsilon$ . The current  $\langle I_L \rangle$  depends on the properties of the system and with our set of parameters we get currents in the order of 1 fA which is experimentally accessible. In this regime, a change of  $\Gamma$  is dominantly a scaling of the current and we therefore plot the ratio between  $\langle I_L \rangle$  and  $\Gamma$ . For  $\varepsilon = 0$  the lower levels of the dots are aligned yielding a broad resonant peak. One might expect a similar peak for  $\varepsilon = \Delta_R - \Delta_L$  when the two upper states coincide. This peak is in fact much smaller than the central peak. The reason is that the lower left dot level is below the lower right dot level. If this state is occupied, the Coulomb interaction prevents another electron from tunneling from the left lead on the DQD and the transport can not continue until the electron hops via thermal activation, coherent tunneling or a higher order process to the right dot. Actually, this is why the current for  $\varepsilon < 0$  is smaller than for  $\varepsilon > 0$ . Another broader peak appears at the far right side of the plot when the lower left dot level is aligned with the higher

right dot level. In our case, the linewidth of this peak is determined by the temperature. In contrast to these broad peaks, much sharper peaks emerge at the lasing-resonances when one of the energy level gaps is tuned to the microwave oscillator frequency. The best visible ones are the two most right peaks where the broad peak is weaker. The other peaks are too small or too close to the central resonance peak at the given resolution of the plot.

To investigate the possible appearance of the lasing conditions in the current also for the smaller peaks, we plot the difference of the current between the situation with and without coupling to the oscillator in the lower of the three panels in Fig. 4.1. All lasing situations have a clear imprint in the current. In particular, the lasing peaks in the photon number identified as a backward tunneling process (labeled (3) and (1)) are linked to a sharp dip in the current.

### 4.2.2 Detailed Analysis of the Cascade Lasing

As described in Sec. 4.1.1, the Fano factor  $F_a$  accounts for the statistics of the produced photons in the microwave oscillator and has a specific behavior in the lasing regime. Therefore, it is a good measure if the sharp photon peaks are really associated with lasing. In Fig. 4.2 we show the results in the vicinity of the resonance labeled (3), but similar results are found also for the other lasing peaks. The figure displays the increase of the Fano factor in the vicinity of all peaks. For weak tunneling strength  $t = 0.01\omega_0$  and phonon coupling strength  $g_{el-ph} = 0.01\omega_0$ , the Fano factor shows a clear dip and even drops below 1. This is a signature of lasing, although the total number of photons remains small. With increasing phonon coupling or

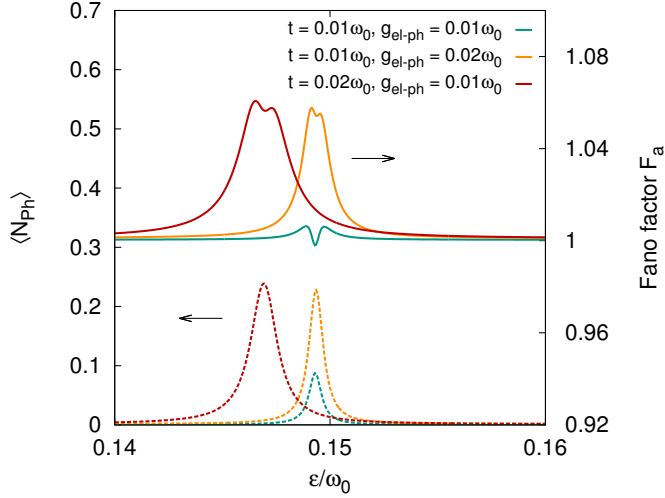


FIG. 4.2: Photon expectation value  $\langle N_{\text{Ph}} \rangle$  (dashed lines) and Fano factor  $F_a$  (solid lines) vs. detuning  $\varepsilon$  for  $\Delta_L = 1.3$ ,  $\Delta_R = 1.15$  and different phonon couplings strengths  $g_{\text{el-ph}}$  or tunneling strengths  $t$ . Reprinted with permission of Ref. [V]. Copyright (2015) by the American Physical Society.

tunneling strength the number of photon rises, but the dip is less pronounced.

The processes involving a series of transitions, inclusive inelastic ones, and the resulting lasing-type situations strongly rely on the coupling to the phonons. We illustrate this in Fig. 4.3 for the two processes labeled (2) at  $\varepsilon = (1 - \Delta_L)\omega_0$  and (3) at  $\varepsilon = (\Delta_R - 1)\omega_0$  by varying the strength of the phonon coupling. The peak in the photon number, arising from a backward tunneling process depending on the population of the upper right level, disappears in the absence of phonons and grows with increasing phonon coupling strength. The



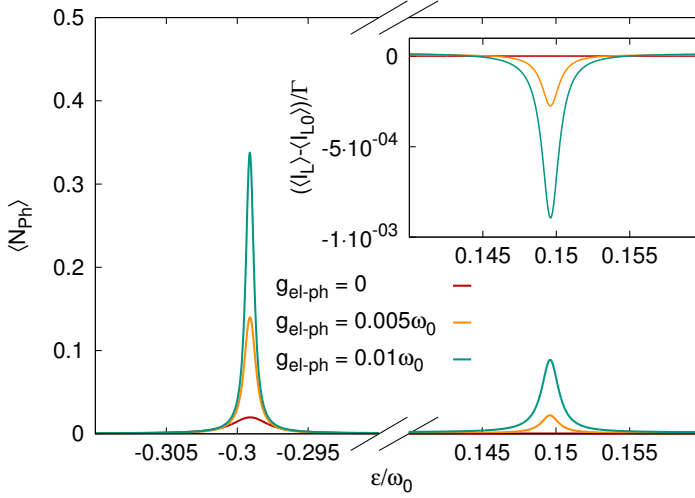


FIG. 4.3: Photon number  $\langle N_{\text{Ph}} \rangle$  vs. detuning  $\varepsilon$  for  $\Delta_L = 1.3$ ,  $\Delta_R = 1.15$  and different phonon coupling strengths  $g_{\text{el-ph}}$ . The tunneling strength is  $t = 0.01\omega_0$ . The inset shows the difference  $(\langle I_L \rangle - \langle I_{L0} \rangle)/\Gamma$  between the currents with ( $g = 0.01\omega_0$ ) and without ( $g = 0$ ) coupling to the oscillator vs. the detuning  $\varepsilon$ . Reprinted with permission of Ref. [V]. Copyright (2015) by the American Physical Society.

effect is also visible in the current as shown in the inset of the figure. Also in process (2) the transition through the DQD system is strongly enhanced by the phonons leading to more pronounced photon peaks.

In Fig. 4.5 we illustrate the dependency of the lasing peaks on the tunneling strength  $t$ . Such a dependency was also investigated in the experiments with single-level double quantum dots by Stockklauser *et al.* [50] shown in Fig. 4.4. They found that with stronger tunneling strength the hybridization of the levels leads to a merging of the

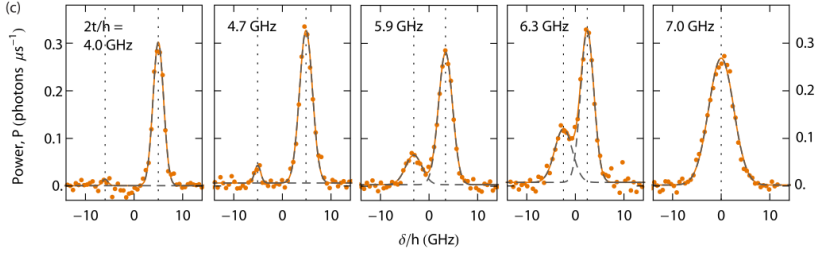


FIG. 4.4: Photon emission power vs. the detuning of the single dot levels  $\delta$  measured for the indicated interdot tunnel rates  $2t/h$  with  $h$  the Planck constant. The background proportional to the current is subtracted and the emission resonances are fitted using a sum of two Gaussian line shapes to extract the values of resonant detuning and power (sum is the solid orange line; individual line shapes are dashed gray lines). Reprinted with permission of Ref. [50]. Copyright (2015) by the American Physical Society.

resonance peaks. In our system, for weak tunneling the lasing peaks are sharp. With increasing tunneling strength the transport current through the DQD and the population inversion increase leading to more photons. But eventually also the hybridization of the dot levels becomes stronger. This leads to broader and weaker peaks, and the peaks are shifted due to the hybridization. Their positions  $\varepsilon_p$  follow from the condition

$$1 = \frac{\Delta_L + \Delta_R}{2} - \sqrt{\left(\frac{t}{\omega_0}\right)^2 + \left(\frac{\varepsilon_p}{2\omega_0}\right)^2} - \sqrt{\left(\frac{t}{\omega_0}\right)^2 + \left(\frac{\Delta_L - \Delta_R + \varepsilon_p/\omega_0}{2}\right)^2}. \quad (4.23)$$

This equation has two solutions for a sufficiently small tunneling  $t$  (as illustrated in the inset of Fig. 4.5) determining the positions of the two lasing peaks. When the tunneling strength is stronger the

## 4.2 Lasing in the Multi-Level System

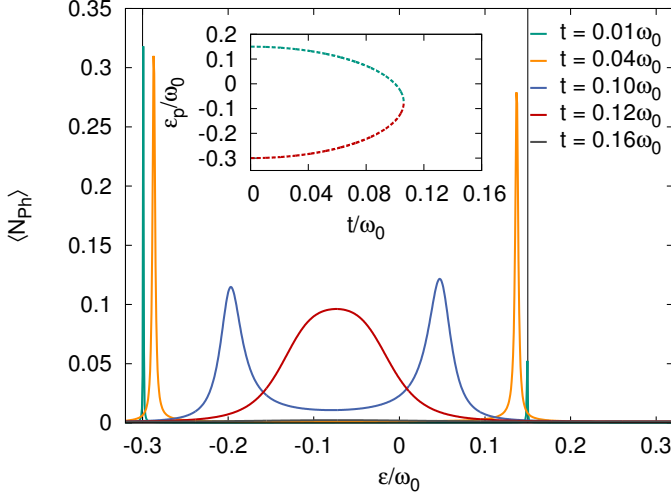


FIG. 4.5: Photon number  $\langle N_{\text{Ph}} \rangle$  vs. the detuning  $\varepsilon$  with  $\Delta_L = 1.3$ ,  $\Delta_R = 1.15$  and for different tunneling strengths  $t$ . The phonon coupling strength is  $g_{el-ph} = 0.01\omega_0$ . The inset shows the two ideal solutions for the peak position  $\varepsilon_p$  vs. the tunneling strength  $t$ . Reprinted with permission of Ref. [V]. Copyright (2015) by the American Physical Society.

peaks merge and it is not possible to satisfy the separate resonance conditions anymore. In this case we still observe an enhanced photon number, but the process is no longer associated with lasing. A physical argument for the disappearing of the lasing peaks may be as follows: For strong hybridization the distinction between left and right levels is lost. This is, however, crucial for the creation of a population inversion by the imposed current.



# 5 Chapter

---

## Master Equation

This part of the thesis focuses on the expansion of the QME beyond the Lindblad-form used in the chapters 3 and 4. The often used Born and Markov approximations are strong restrictions. The method developed in this thesis shows the dependencies and the validity of these approximations. It uses the diagrammatic expansion of the QME developed in the group of G. Schön at the KIT [57] as shown in chapter 2. We will illustrate our findings with three examples: the spin-boson model, the initial state problem and the two-time correlator.

## 5.1 Expansion of the QME

Solving the QME without any approximation is complex and even numerically most of the time challenging. The main problem is that the equation is not time local and therefore, depending on the kernel of the integral, the integration has to be made for the whole time range. As shown in the introductory chapter 2, Breuer *et al.* found with the TCL method a way to transform the QME in a time local equation, but this method is often clumsy and difficult to handle. In this chapter we develop an expansion of the QME which, on the one hand, results in a time local equation and, on the other, connects the Born and Markov approximations.

The following four sections 5.1.1-5.3 are based on the publication Karlewski and Marthaler [II] and the reference is therefore not cited any further in this part.

### 5.1.1 Time Local QME and Diagrammatic Expansion

To get the solution of the reduced density matrix  $\rho_I(t)$  at time  $t$ , the QME has to be solved for the whole past of  $\rho_I$  from  $t_0 \rightarrow -\infty$  to  $t$ , i.e.,

$$\dot{\rho}_I(t) = \int_{-\infty}^t dt' \Sigma_I(t', t) \rho_I(t'). \quad (5.1)$$

The Markov approximation reduces the problem by using just the actual state of the system and neglecting its history. This can be improved by not only using the information about  $\rho_I(t)$  but additionally the derivative  $\dot{\rho}_I(t)$ . Eventually, we use an expansion in derivatives

## 5.1 Expansion of the QME

---

of the reduced density matrix and primitive integrals of the kernels to obtain a time local QME as Rojek *et al.* [84] used in a similar way to describe the pumping of quantum dots. This is accomplished by integration by parts of Eq. (5.1) where an upper index will mark the primitive integral of a function. The antiderivatives of the self-energy are

$$\Sigma_{\text{I}}^{(k+1)}(t-t') = \int_{\infty}^{t-t'} dt'' \Sigma_{\text{I}}^{(k)}(t''). \quad (5.2)$$

We apply the integration by parts once to Eq.(5.1) resulting in the following term with the definition from above

$$\dot{\rho}_{\text{I}}(t) = - \left[ \int_{\infty}^{t-t'} dt'' \Sigma_{\text{I}}^{(0)}(t'') \rho_{\text{I}}(t') \right]_{t'=-\infty}^t + \int_{-\infty}^t dt' \Sigma_{\text{I}}^{(1)}(t-t') \dot{\rho}_{\text{I}}(t'). \quad (5.3)$$

The term in the square brackets can be identified as the Markov approximation (see Eq. (2.11)) if evaluated at  $t' = t$  and vanishes if evaluated at minus infinity. Continuous application of the integration by parts produces derivatives of the reduced density matrix multiplied by antiderivatives of the self-energy. It is an expansion in the derivatives of  $\rho_{\text{I}}(t)$  and we call it the Markov expansion. To keep things short, we define  $\mathcal{S}^{(k)} = \left( \int_0^{\infty} dt' \Sigma_{\text{I}}^{(k)}(t') \right)$  and the  $k^{\text{th}}$  derivative of  $\rho_{\text{I}}(t)$  as  $\rho_{(k),\text{I}}(t)$ . The QME (5.1) contains the propagation of the

first derivative and is in this notation

$$\rho_{(1),I}(t) = \sum_{l=0}^{\infty} \mathcal{S}^{(l)} \rho_{(l),I}(t). \quad (5.4)$$

The  $k^{\text{th}}$  derivative can be derived by  $k$ -times differentiating Eq. (5.4) and is coupled in this way to its antiderivative, itself and all the derivatives of itself

$$k > 0; \quad \rho_{(k),I}(t) = \sum_{l=k-1}^{\infty} \mathcal{S}^{(1-k+l)} \rho_{(l),I}(t). \quad (5.5)$$

The Eq. (5.4) is identical to Eq. (5.1) and is in this sense exact if all summands are considered. Now, we recursively insert Eq. (5.5) in Eq. (5.4). The right hand side of Eq. (5.4) should only depend on  $\rho_{(0),I}$  and not on any derivatives anymore (to keep the equation compact we write  $\rho_{(k),I}$  without its argument)

$$\rho_{(1),I} = \underbrace{\mathcal{S}^{(0)}}_{A_1} \rho_{(0),I} + \sum_{l=1}^{\infty} \mathcal{S}^{(l)} \sum_{m=l-1}^{\infty} \mathcal{S}^{(1-l+m)} \rho_{(m),I}, \quad (5.6)$$

$$\begin{aligned} \rho_{(1),I} &= A_1 \rho_{(0),I} + \underbrace{\mathcal{S}^{(1)} \mathcal{S}^{(0)}}_{A_2} \rho_{(0),I} \\ &+ \sum_{l=1}^{\infty} \mathcal{S}^{(l)} \sum_{m=l}^{\infty} \mathcal{S}^{(1-l+m)} \rho_{(m),I} + \sum_{l=2}^{\infty} \mathcal{S}^{(l)} \mathcal{S}^{(0)} \rho_{(l-1),I}. \end{aligned} \quad (5.7)$$

Repeated inserting of Eq. (5.5) leads to a compact form of Eq. (5.1)

$$\rho_{(1),I}(t) = \left( \sum_{n=1}^{\infty} A_n \right) \rho_{(0),I}(t). \quad (5.8)$$



## 5.1 Expansion of the QME

---

A  $A_n$  consists of different terms of products of  $\mathcal{S}^{(k)}$ ,

$$A_n = \sum_m \left[ \prod_1^n \mathcal{S}^{(f_m(n))} \right], \quad (5.9)$$

which can be calculated following these rules for  $f_m(n)$ :

- The sum of the indices  $f_m(n)$  for all  $\mathcal{S}^{(f_m(n))}$  of one term must be  $n - 1$ ,  $f_m(n) \in \mathbb{N}_0$ .
- Assign each  $\mathcal{S}^{(f_m(n))}$  from right to left a position index  $p$ . The sum of the indices  $f_m(n)$  from 1 to a given position  $p$  must be smaller  $p$ .

All terms fulfilling the two rules above must be summed ( $\sum_m$ ). For example, with these rules the possible terms of  $A_3$  are

$$\left. \begin{array}{l} \mathcal{S}^{(2)}\mathcal{S}^{(0)}\mathcal{S}^{(0)} \Rightarrow \checkmark \\ \mathcal{S}^{(0)}\mathcal{S}^{(2)}\mathcal{S}^{(0)} \Rightarrow \cancel{\checkmark} \\ \mathcal{S}^{(0)}\mathcal{S}^{(0)}\mathcal{S}^{(2)} \Rightarrow \cancel{\checkmark} \\ \mathcal{S}^{(1)}\mathcal{S}^{(1)}\mathcal{S}^{(0)} \Rightarrow \checkmark \\ \mathcal{S}^{(1)}\mathcal{S}^{(0)}\mathcal{S}^{(1)} \Rightarrow \cancel{\checkmark} \\ \mathcal{S}^{(0)}\mathcal{S}^{(1)}\mathcal{S}^{(1)} \Rightarrow \cancel{\checkmark} \end{array} \right\} A_3 = \mathcal{S}^{(2)}\mathcal{S}^{(0)}\mathcal{S}^{(0)} + \mathcal{S}^{(1)}\mathcal{S}^{(1)}\mathcal{S}^{(0)}. \quad (5.10)$$

The condition for the steady state solution of the system where the derivative of  $\rho_{(0),I}$  is zero, i.e.,  $\rho_{(1),I} = \sum_I^{(0)} \rho_{(0),I} = 0$ , implies identical solutions of the Markovian and non-Markovian QMEs in the steady state and of course all the derivatives of  $\rho_{(0),I}$  are then zero.

To have a useful expansion which we could truncate at wanted order, we need a small expansion parameter. Therefore, we use the

diagrammatic expansion introduced in chapter 2.3 and study the time dependence of the self-energy and the coupling to the bath. The diagrammatic expansion is done in the contractions and we call this the Born expansion because the lowest order in contractions is known as the Born approximation. The self-energy  $\Sigma_I(t - t')$  is defined as shown before by all the possible irreducible diagrams on the Keldysh contour

$$\Sigma_I(t - t') = \text{[diagram 1]} + \text{[diagram 2]} + \text{[diagram 3]} + \text{[diagram 4]} + \text{[diagram 5]} + \dots \quad (5.11)$$

With the notation we developed in this part we can write the diagrammatic expansion of the self-energy with a lower index  $k$  corresponding to the number of contractions

$$\Sigma_I(t, t') = \Sigma_{1,I}(t, t') + \Sigma_{2,I}(t, t') + \dots + \Sigma_{k,I}(t, t') + \dots \quad (5.12)$$

The next step is to identify the small parameter which is done via the combination of the two expansions.

### 5.1.2 Combined Expansion

It is important to define the correlation functions and their properties as general as possible to identify the order of magnitudes of the self-energy. Our assumption is that the bath or environment has a maximum memory time, i.e., a minimum decay rate  $\gamma_{\min}$ . Additionally, we estimate the decay as an exponential function  $C_{ij}^{\leq}(t) \propto \exp(-\gamma_{\min}t)$ . This is useful for the estimation of the order of magnitude of inte-

grations of the correlation functions. In principal, our method is also applicable for other cases if the order of magnitude of the integration can be predicted.

The important energy scales of the problem are the characteristic energy scale of the small quantum system which we call for now  $\Delta E$ , the coupling strength  $g_c$  between the system and the bath and the inverse of the maximum correlation time  $\hbar\gamma_{\min}$  (for comparison  $\hbar$  is written explicitly in this paragraph). The system energy  $\Delta E$ , e.g., is in a two level system given by the energy splitting of the two levels and defines in general the time scale of coherent dynamics in the system. It is included in the self-energy in exponential form by changing from the interaction to the Schrödinger picture. The Markov expansion as well as the number of contractions yields integrations of the self-energy. Each integration leads to a factor of the order  $1/(\hbar\gamma_{\min} + \Delta E)$ . We will assume that the correlation decay rate is larger than the system energy scale  $\hbar\gamma_{\min} > \Delta E$ . In this limit we can approximate the prefactor by  $1/\hbar\gamma_{\min}$ . This is the most important case. For example, if  $\hbar\gamma_{\min} \gg \Delta E$  the bath correlation decays fast on time scales relevant for the system dynamics and the bath correlation function can be approximated with a Dirac delta distribution. This case corresponds to the Markov approximation. In the opposite case, the prefactor can be approximated by  $1/\Delta E$  and our model is still applicable. The Born approximation is known as the weak coupling limit  $\Delta E \gg g_c$ . In our exact expansion we show that a combination of the coupling strength  $g_c$  and the decay rate  $\hbar\gamma_{\min}$  is the correct expansion parameter.

We combine the two expansions by extending the former defined

$\mathcal{S}^{(k)}$  with another index accounting for the involved number of contractions, i.e.,  $S^{(k)} = \sum_l \mathcal{S}_l^{(k)}$  with  $\mathcal{S}_l^{(k)} = \left( \int_{-\infty}^t dt' \Sigma_{l,I}^{(k)}(t-t') \right)$ . Thus, the QME (5.1) in the Born-Markov expansion is given by

$$\rho_{(1),I}(t) = \left( \sum_{n=1}^{\infty} \sum_m \left[ \prod_1^n \sum_l \mathcal{S}_l^{(f_m(n))} \right] \right) \rho_{(0),I}(t), \quad (5.13)$$

which is the main equation of this part. To estimate the order of magnitude of the terms we have a closer look at the  $\mathcal{S}_l^{(k)}$ . Each contraction produces a factor  $g_c^2$ , so  $l$  contractions give  $g_c^{2l}$ . Additionally, the contractions result in each diagram in  $2l - 1$  integrations and the primitive integrals give  $k$  more integrations. Altogether, each  $\mathcal{S}_l^{(k)}$  yields a factor  $\mathcal{O}\left(g_c^{2l}/\gamma_{\min}^{2l-1+k}\right)$  which is the small parameter of our Born-Markov expansion. To illustrate our result we present the expansion up to order  $\mathcal{O}(g_c^6/\gamma_{\min}^5)$

$$\begin{aligned} \rho_{(1),I} = & \left( \mathcal{S}_1^{(0)} + \mathcal{S}_2^{(0)} + \mathcal{S}_3^{(0)} + \right. \\ & \mathcal{S}_1^{(1)} \mathcal{S}_1^{(0)} + \mathcal{S}_2^{(1)} \mathcal{S}_1^{(0)} + \mathcal{S}_1^{(1)} \mathcal{S}_2^{(0)} + \\ & \left. \mathcal{S}_1^{(2)} \mathcal{S}_1^{(0)} \mathcal{S}_1^{(0)} + \mathcal{S}_1^{(1)} \mathcal{S}_1^{(1)} \mathcal{S}_1^{(0)} \right) \rho_{(0),I} + \mathcal{O}(g_c^8/\gamma_{\min}^7). \end{aligned} \quad (5.14)$$

The Markov approximation is the lowest order in the expansion in the primitive integrals, meaning all terms with a single  $\mathcal{S}_l^{(0)}$  (first row of Eq. (5.14)). The Born approximation corresponds to lowest order terms in the contractions  $\mathcal{S}_1^{(k)}$  (one contraction). The two approximations which seem first independent can now be compared by the order of magnitude of higher order terms. For example, the second term in the Born expansion is  $\mathcal{S}_2^{(0)} = \mathcal{O}(g_c^4/\gamma_{\min}^3)$  which is exactly the

same order of magnitude as the second term in the Markov expansion  $\mathcal{S}_1^{(1)}\mathcal{S}_1^{(0)} = \mathcal{O}(g_c^4/\gamma_{\min}^3)$ . Each higher order term of one of the expansions is of the same order as a cross term in the other expansion. Thus, it is not justifiable in general to use one of the approximations and go to all orders in the other, as e.g., in non-Markovian calculations with Born approximation [85–88]. It is possible that such investigations are correct on certain time-scales, what needs to be judged case by case.

An outstanding property of our method is that all terms can be traced back to their origin meaning if they result from correlation parts of the bath, higher order contractions or are cross terms. But they are still easy to estimate.

## 5.2 Spin-Boson Model

To see the influence of higher order terms of the different expansions and approximations we analyze the spin-boson model in this section. The spin-boson model is an important and often used model to analyze new ideas how to treat and expand the QME [89, 90]. It contains a two-level system (the spin) coupled to an infinite bath of bosonic modes. The popularity of the model is due to its simplicity and wide applicability, e.g., in electron transfer reactions [91], bio molecules [92], cavity-QED [93, 94] and general dissipative quantum systems [85, 95]. Moreover, it can be solved exact in the Born approximation [96] and perturbatively in a wide parameter regime [97].

We use now the method developed in the previous section of this

thesis to test the influence of the higher order terms in the Born and Markov expansions. Thus, we have to specify the different parts of the total Hamilton operator  $H(t)$ . The two level system is defined by its energy splitting  $\Delta E$ . We want to add a driving with driving frequency  $\omega_D$  being in resonance with the spin  $\omega_D = \Delta E$  to have the possibility to excite the system from the equilibrium state,

$$H_S(t) = \frac{1}{2}\Delta E\sigma_z + g_D\sigma_x \cos(\omega_D t)f(t). \quad (5.15)$$

$\sigma_z$  and  $\sigma_x$  are the Pauli matrices and the function  $f(t)$  defines the shape of the driving pulse. To analyze the influence of the different expansion terms we have a closer look at the decay of the excited state, thus the driving is important for our example. We will use the rotating frame with respect to the driving term to implement this in our calculation. The rotating frame transformation is done by separating the driving from the time independent Hamiltonian, i.e.,  $\tilde{A}(t) = e^{-\frac{i}{2}\Delta E\sigma_z t} A(t) e^{\frac{i}{2}\Delta E\sigma_z t}$ .

Next, we specify the environment as a bath of harmonic oscillators

$$H_B = \sum_i \omega_i b_i^\dagger b_i \quad (5.16)$$

with bosonic creation  $b_i^\dagger$  and annihilation  $b_i$  operators. The bosonic modes are coupled to the spin in the rotating wave approximation via

$$H_C = g_c \sum_i (\sigma_+ b_i + \sigma_- b_i^\dagger). \quad (5.17)$$

## 5.2 Spin-Boson Model

---

The bath will enter the QME due to their correlation functions as in Ref. [26]

$$\begin{aligned}\sum_i \langle \tilde{b}_i^\dagger(t') \tilde{b}_i(t) \rangle_{\text{B}} &= C^-(t-t') = \int_0^\infty d\omega J(\omega) n_{\text{B}}(\omega) e^{i\omega(t-t')} \\ \sum_i \langle \tilde{b}_i(t') \tilde{b}_i^\dagger(t) \rangle_{\text{B}} &= C^+(t-t') = \int_0^\infty d\omega J(\omega) (n_{\text{B}}(\omega) + 1) e^{-i\omega(t'-t)},\end{aligned}\tag{5.18}$$

with the spectral density function  $J(\omega)$  and the Bose-Einstein statistic

$$n_{\text{B}}(\omega) = \frac{1}{\exp(\hbar\omega/k_{\text{B}}T) - 1}.\tag{5.19}$$

Eq. (5.18) consistently defines the spectral function as the Fourier transform of the correlation function. The Fourier transformed functions are indicated just by their argument  $\omega$

$$\begin{aligned}C^-(\omega) &= J(\omega) n_{\text{B}}(\omega), \\ C^+(\omega) &= J(\omega) (n_{\text{B}}(\omega) + 1).\end{aligned}\tag{5.20}$$

In this example we will use the Ohmic spectral density with the Lorentz-Drude cutoff  $J(\omega) = \omega / (1 + (\frac{\omega}{\omega_{\text{C}}})^2)$  and  $\omega_{\text{C}}$  the cutoff frequency.

We start the simulation from the equilibrium without driving. Then, we pulse the system for a time  $\tau$ . This driving pulse affects the reduced density matrix  $\tilde{\rho}(t)$  but also its derivatives. These infor-

mation is included in Eq. (5.4) of the Markov expansion containing all the derivatives of  $\tilde{\rho}(t)$

$$\tilde{\rho}_{(1)}(t) = i[g_D \sigma_x f(t), \tilde{\rho}_{(0)}(t)] + \sum_{l=0}^{\infty} \tilde{\mathcal{S}}^{(l)} \tilde{\rho}_{(l)}(t). \quad (5.21)$$

It is particularly interesting that the derivatives give the spin an inertia. So, the reduced density matrix replies with delay to the beginning and ending of the driving pulse which is a non-Markovian effect. To estimate and compare the different orders of magnitude of the terms we assume that the  $k^{\text{th}}$  derivative of the reduced density matrix  $\tilde{\rho}_{(k)}$  is of order  $\mathcal{O}(g_c^{k \cdot 2} / \gamma_{\min}^k)$ . This is strictly speaking only correct in the limit of a time independent system Hamiltonian as described in section 5.1.2 in Eq. (5.13). To use this estimation, the change induced by the driving needs to be slow in comparison to the system dynamics. In the end, it results in the expansion up to order  $\mathcal{O}(g_c^6 / \gamma_{\min}^5)$ ,

$$\begin{aligned} \tilde{\rho}_{(1)} = & i[\tilde{H}_D(t), \tilde{\rho}_{(0)}] + \left( \tilde{\mathcal{S}}_1^{(0)} + \tilde{\mathcal{S}}_2^{(0)} + \tilde{\mathcal{S}}_3^{(0)} \right) \tilde{\rho}_{(0)} \\ & + \left( \tilde{\mathcal{S}}_1^{(1)} + \tilde{\mathcal{S}}_2^{(1)} \right) \tilde{\rho}_{(1)} + \tilde{\mathcal{S}}_1^{(2)} \tilde{\rho}_{(2)} + \mathcal{O}(g_c^8 / \gamma_{\min}^7). \end{aligned} \quad (5.22)$$

Additionally, the energy splitting of the spin is in principle influenced by the driving pulse. The new eigenenergies of the system are  $\pm \sqrt{\Delta E^2 / 4 + g_D^2}$ . Therefore, if the driving strength is small the eigenenergies are approximately  $\pm \frac{1}{2} |\Delta E|$ , and will not effect the expansion of the self-energy.

The choice of our coupling Hamiltonian  $H_C = g_c \sum_i (\sigma_+ b_i + \sigma_- b_i^\dagger)$  and the assumption of an equilibrium bosonic bath secures that the





as contribution to the integrand. The parameters  $b$ ,  $d$  and  $c$  depend on the contraction, i.e., if the contraction is along the Keldysh contour, on the order of the involved bath operators and on the involved energy splitting. A vertex at position  $t_l$  can thus either have a positive or negative sign in front of the time  $t_l$ , indicated below by an additional parameter  $a_l$ , and defined by the parameters  $b_l$ ,  $d_l$  and  $c_l$ .

Now, we can write a general form of a diagram  $\tilde{S}_{n_c}^{(k)}$  with  $n_c$  contractions in mathematical language with time ordered integrals  $I_{n_c}^j$  and in the limit of  $t_0 \rightarrow -\infty$

$$\prod_{j=1}^{2n_c-1} \int_{d\omega_j^{c_j}} I_{n_c}^j = \prod_{j=1}^{2n_c-1} \int_{d\omega_j^{c_j}} \int_{t_{j-1}}^{t_{j+1}} dt_j \left( \int_{\infty}^t dt_{2n_c} \right)^k \cdot e^{ia_j t_j (b_j \Delta E - c_j d_j \omega_j)} \cdot e^{ia_{2n_c} t_{2n_c} (b_{2n_c} \Delta E - c_{2n_c} d_{2n_c} \omega_{2n_c})}. \quad (5.25)$$

Each vertex is at a time  $t_j$ ,  $j = 1, 2, \dots, 2n_c - 1$  (the time of the last vertex is fixed to time  $t$ ) and time ordered with  $t_j < t_{j+1}$ . A vertex is defined by Eq. (5.24). We use the spectral functions (see Eq. (5.20)) in this equation and the frequency integrals  $\int_{d\omega_j^{c_j}}$  are symbolic representations for the integrals including these spectral functions

$$\int_{d\omega_j^<} = \int_{-\infty}^{\infty} d\omega_j J(\omega_j) n(\omega_j), \quad (5.26)$$

$$\int_{d\omega_j^>} = \int_{-\infty}^{\infty} d\omega_j J(\omega_j) (n(\omega_j) + 1). \quad (5.27)$$

## 5.2 Spin-Boson Model

---

Thus, only  $n_c$  spectral functions, one from each contraction, occur with  $n_c$  different  $\omega_j^{c_j}$ . The double counting by the index  $j$  numbering the vertices must be ignored and all integrals are only evaluated once. The time integrals to the power  $k$  are caused by the antiderivatives of the self-energy and should be read as

$$\left(\int_{\infty}^t\right)^k = \int_{\infty}^t d\tau_1 \int_{\infty}^{\tau_1} d\tau_2 \cdots \int_{\infty}^{\tau_{k-1}} dt_{2n_c}. \quad (5.28)$$

The spin-boson model in our formulation restricts the possible combinations of the parameters  $a_j$ ,  $b_j$ ,  $c_j$  and  $d_j$  and the frequency  $\omega_j$  of the spectral function for a contraction between the time steps  $t_j$  and  $t_l$  to

$$\omega_j = \omega_l, a_j = -a_l, b_j = b_l, c_j = c_l, d_j = d_l. \quad (5.29)$$

All these parameters appear in Eq. (5.25) in the exponent of the integrand. We combine them in the function  $\Gamma_j$  with  $\eta = 0^+$  as convergence factor of the integrals in Eq. (5.25)

$$\Gamma_j = a_j(b_j\Delta E - c_jd_j\omega_j - ia_j\eta). \quad (5.30)$$

With the exponents  $\Gamma_j$  the time integrals  $I_{n_c}^j$  are

$$\prod_{j=1}^{2n_c-1} I_{n_c}^j = \frac{\exp\left[i\sum_{l=1}^{2n_c}\Gamma_l t\right]}{\prod_{j=1}^{2n_c-1}(\sum_{l=1}^j i\Gamma_l) \cdot (\sum_{l=1}^{2n_c-1} i\Gamma_l)^k}. \quad (5.31)$$

At first glance this looks like the time dependence remains after the

integration, which would be incorrect. But each  $\Gamma_l$  is associated with a vertex and all the vertices are connected with one other vertex via a contraction. For each contraction between  $t_j$  and  $t_l$  the corresponding  $\Gamma_j$  and  $\Gamma_l$  fulfill the condition  $\Gamma_j = -\Gamma_l$  in the limit  $\eta \rightarrow 0$ . Summing up all the  $\Gamma_l$  in the exponent leads to a zero and the numerator of the fraction is 1, so the time dependence is removed.

To evaluate the denominator, the Sokhotsky-Weierstrass theorem

$$\lim_{\eta \rightarrow 0^+} \frac{1}{(x + i\eta)^n} = \text{P} \frac{1}{x^n} - i\pi \frac{(-1)^{n-1}}{(n-1)!} \delta^{(n-1)}(x), \quad (5.32)$$

where P denotes a principal value integral, can be used and yields

$k = 0 :$

$$\prod_{j=1}^{2n_c-1} I_{n_c}^j = \prod_{j=1}^{2n_c-1} (-1)^{n_c+1} \left[ \pi \delta^0 \left( \sum_{l=1}^j -\text{Re}\{\Gamma_l\} \right) + i\text{P} \frac{1}{\sum_{l=1}^j -\text{Re}\{\Gamma_l\}} \right] \quad (5.33)$$

$k > 0 :$

$$\begin{aligned} \prod_{j=1}^{2n_c-1} I_{n_c}^j &= \prod_{j=1}^{2n_c-1} (-1)^{n_c+1} \left[ \pi \delta^0 \left( \sum_{l=1}^j -\text{Re}\{\Gamma_l\} \right) + i\text{P} \frac{1}{\sum_{l=1}^j -\text{Re}\{\Gamma_l\}} \right] \\ &\cdot \left\{ (-1)^{n_c+1} \left[ \pi \frac{(-1)^{k-1}}{k!} \delta^{(k-1)} \left( \sum_{l=1}^{2n_c-1} -\text{Re}\{\Gamma_l\} \right) \right. \right. \\ &\left. \left. + i\text{P} \frac{1}{\left( \sum_{l=1}^{2n_c-1} -\text{Re}\{\Gamma_l\} \right)^k} \right] \right\}. \end{aligned} \quad (5.34)$$

This rather complicated expression for the integrand of the integrals  $\int_{d\omega_j^{c_j}}$  is not useful, because of the combination of principal value

integrals and Dirac delta distributions. But, the spin-boson model in our form makes it again possible to add up diagrams contributing to the same in- and outgoing states and number of contractions. For example, depending on the diagram, mirror operations on the diagram by changing the order of the operators on the real time axis can lead to such behavior. This corresponds to changing the sign of  $a_j$ , but not touching the other parameters  $b_j$ ,  $c_j$  and  $d_j$ . This means that complex numbers with opposite imaginary parts are summed in the Eq. (5.33) and Eq. (5.34). Therefore, the imaginary part of the self-energy with the principal values vanishes. But in general there could be principal value contributions to the real part of the system in higher order cross terms which needs to be taken into account.

In the simple case of the Born-Markov approximation with  $k = 0$  and  $n_c = 1$  only the delta distribution  $\delta(\omega - \Delta E)$ , the real part of Eq. (5.33), contributes to the QME. In the appendix A.2 an example of a summation of higher order diagrams is shown.

Based on reference [57] (see section 2.3), we established the following rules for our system [II]:

- I. A contraction from a  $\ominus$ -Vertex to a  $\oplus$ -Vertex along the Keldysh-contour gives a factor  $\frac{\partial^k \tilde{C}^-(\pm \Delta E)}{\partial \omega^k}$ .
- II. A contraction from a  $\oplus$ -Vertex to a  $\ominus$ -Vertex along the Keldysh-contour gives a factor  $\frac{\partial^k \tilde{C}^+(\pm \Delta E)}{\partial \omega^k}$ .
- III. The prefactor  $g_c^{2n_c} \cdot (-1)^{n_c+l}$  is given by  $n_c$  the number of contractions,  $l$  the number of vertices on the lower contour and  $g_c$  the coupling constant to the bath.

- IV. Each vertex at  $t_i$  gives a factor  $\langle \bar{q}_i | \sigma_i | q_i \rangle$  with  $|q_i\rangle$  the incoming state and  $|\bar{q}_i\rangle$  the outgoing state.

### 5.2.2 Comparing Different Orders

The different terms of our expansion can be used to investigate the effect of the often used Born and Markov approximations. Therefore, we compare three different simulations. First, a simulation which contains all terms of our expansion is given by Eq. (5.22). This, we call the non-Born-Markov (NBM) simulation. Second, we use the standard Born-Markov (BM) approximation and third, we compute the dynamics for the QME with Born approximation and without Markov approximation which we name Born simulation (Born). The QME in the BM approximation can in our theory be written as only single contraction diagrams and lowest order in the (anti)derivatives ( $k = 0$ )

$$\tilde{\rho}_{(1)} = \tilde{S}_1^{(0)} \tilde{\rho}_{(0)}. \quad (5.35)$$

This is equivalent to [26]

$$\dot{\tilde{\rho}}(t) = - \int_0^t dt' \text{Tr}_B \left\{ \left[ \tilde{H}_C(t), [\tilde{H}_C(t'), \tilde{\rho}(t) \rho_B] \right] \right\}. \quad (5.36)$$

Furthermore, it is straightforward to write the QME with Born approximation but to all orders in the Markov expansion by using only

single contraction diagrams  $\mathcal{S}_1^{(l)}$  but all terms in  $k$  in Eq. (5.4)

$$\tilde{\rho}_{(1)}(t) = \sum_{k=0}^{\infty} \tilde{\mathcal{S}}_1^{(k)} \tilde{\rho}_{(k)}(t), \quad (5.37)$$

which is in all orders equivalent to Ref. [26] and Eq. (2.8)

$$\dot{\tilde{\rho}}(t) = - \int_0^t dt' \text{Tr}_B \left\{ \left[ \tilde{H}_C(t), [\tilde{H}_C(t'), \tilde{\rho}(t') \rho_B] \right] \right\}. \quad (5.38)$$

For the numerical simulations we want to compute the dynamics up to the order  $\mathcal{O}(g_c^6/\gamma_{\min}^5)$ . This is identical to Eq. (5.22) with only single contractions

$$\tilde{\rho}_{(1)} = \tilde{\mathcal{S}}_1^{(0)} \tilde{\rho}_{(0)} + \tilde{\mathcal{S}}_1^{(1)} \tilde{\rho}_{(1)} + \tilde{\mathcal{S}}_1^{(2)} \tilde{\rho}_{(2)}. \quad (5.39)$$

The focus of this analysis is to investigate the decay of an excited state after the pulse depending on the involved terms from the expansion. For that reason, we prepare the excited state in the NMB model and use the resulting reduced density matrix for all models as starting point. As a result, the preparation is not model dependent. Naturally, initial state correlations of the excited state with the non-Markovian bath are included. Thus, the simulation starts with an equilibrium state and is then pulsed with a weak  $\pi/2$ -pulse in the rotating frame to excite the system. We use as pulse shape a simple step function

$$f(t) = \Theta(t - t_p - \frac{\pi}{2g_D}) \Theta(t_p - t), \quad (5.40)$$

with  $t_p$  the end,  $\frac{\pi}{2g_D}$  the length and  $g_D$  the height of the pulse. Therefore, the area under the pulse is  $\pi/2$ .

As a measure to compare the different decays of the reduced density matrices, we use the trace distance [98]

$$D(A, B) = \frac{1}{2} \|A - B\|_1, \quad (5.41)$$

with  $A$  and  $B$  two trace class operators and  $\|\cdot\|_1$  the trace norm. A trace class operator has a well defined trace also for an infinite dimensional Hilbert-space. Particularly, density matrices fulfill this condition. The physical interpretation of the trace distance for two reduced density matrices is the information about the distinguishability between them [98]. Additionally, the non-Markovianity of a system can be quantified by verifying if and how strong the trace distance increases in time. Markovian processes can in general only decrease the trace distance of two reduced density matrices with trace distance  $D(\rho_a(0), \rho_b(0))$  at time  $t = 0$ , i.e.,  $D(\rho_a(t), \rho_b(t)) \leq D(\rho_a(0), \rho_b(0))$ . If the trace distance grows, then a back flow of information from the bath to the quantum system has taken place which we call a non-Markovian process or effect.

We use in the following investigation the inverse temperature  $\beta = \frac{1}{k_B T} = 10 \Delta E$ , the cut-off frequency  $\omega_C = 10 \Delta E$  and measure all energy scales in multiples of the system energy splitting  $\Delta E$ . As driving strength we choose  $g_D = 0.2 \Delta E$  yielding an energy splitting of the energy eigenstates  $\approx \pm 0.54 |\Delta E|$ . We will use for simplicity also during the driving time the bare energy splitting of  $\pm 0.5 |\Delta E|$ . The end of the pulse  $t_p$  fixes the time  $t = 0$ , in order to investigate



## 5.2 Spin-Boson Model

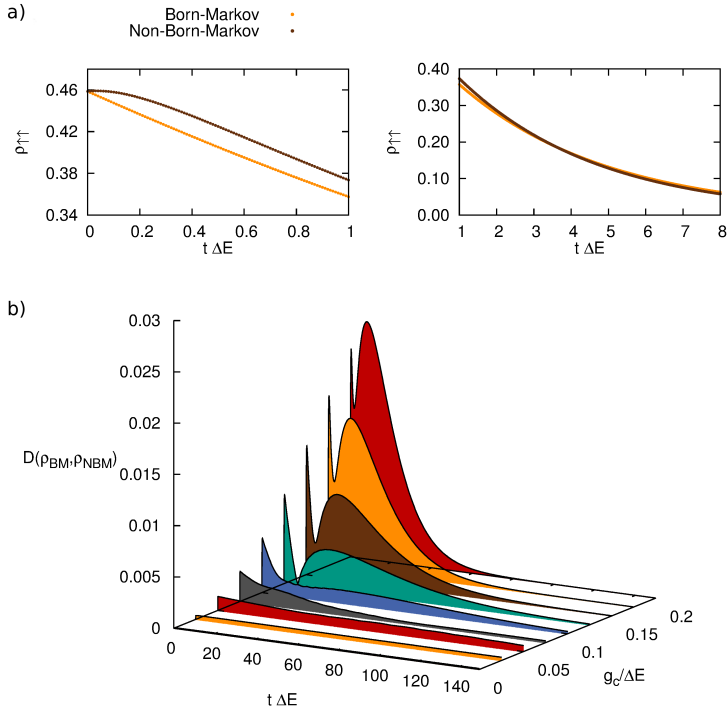


FIG. 5.1: The time  $t = 0$  equals the moment of the end of the pulse  $t_p$ . The inverse temperature is  $\beta = 10 \Delta E$  and the pulse strength is  $g_d = 0.2 \Delta E$ . a) The decay of the excited state  $\rho_{\uparrow\uparrow}$  with and without BM-approximation for the strongest coupling  $g_c = 0.2$  for short times and intermediate times. b) The trace distance  $D(\rho_{\text{BM}}, \rho_{\text{NBM}})$  between the BM simulation  $\rho_{\text{BM}}$  and the NBM simulation  $\rho_{\text{NBM}}$  for different coupling strengths  $g_c$ . Reprinted with permission from [II]. Copyright (2014) by the American Physical Society.

for all positive times the decay of the excited state.

In Fig. 5.1 the difference between the NBM model and the common BM approximation is shown. The population of the up state  $|\uparrow\rangle$  is en-

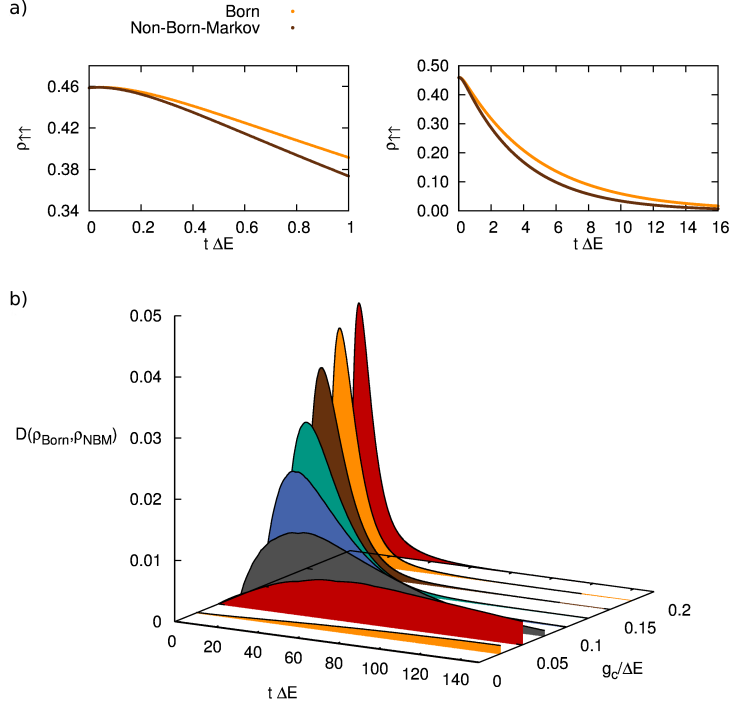


FIG. 5.2: The time  $t = 0$  equals the moment of the end of the pulse  $t_p$ . The inverse temperature is  $\beta = 10 \Delta E$  and the pulse strength is  $g_d = 0.2 \Delta E$ . a) The decay of the excited state  $\rho_{\uparrow\uparrow}$  with and without Born approximation for the strongest coupling  $g_c = 0.2$  for short times and intermediate times. b) The trace distance  $D(\rho_{\text{Born}}, \rho_{\text{NBM}})$  between the BM simulation  $\rho_{\text{Born}}$  and the NBM simulation  $\rho_{\text{NBM}}$  for different coupling strengths  $g_c$ . Reprinted with permission from [II]. Copyright (2014) by the American Physical Society.

coded in the matrix element  $\rho_{\uparrow\uparrow}(t)$ . With our choice of small temperatures the system will for long times decay in the down state  $|\downarrow\rangle$ . In the BM expansion the decay is strictly exponential which can be seen

from the corresponding ordinary differential equation for the matrix element  $\dot{\rho}_{\uparrow\uparrow}(t) = -\Gamma_{\uparrow\uparrow}\rho_{\uparrow\uparrow}(0)$  with  $\Gamma_{\uparrow\uparrow} = \langle \uparrow | \sigma_+ | \downarrow \rangle \langle \downarrow | \sigma_- | \uparrow \rangle C^2 (\Delta E)$  and negligible  $\Gamma_{\downarrow\downarrow}$  because of the small temperature (see Fig. 5.1 a)). The possible excitation from the down state  $|\downarrow\rangle$  is neglected because of the low temperature. However, NBM model shows in the beginning no decay because of the inertia or memory of the preparation. The past of the state is important for the system and initial correlation after the pulse exist. The dynamics for short and intermediate times differs from the BM approximation as shown in Fig. 5.1 b). The trace distance shows two peaks. The first one right after the beginning of the decay. Then, for strong couplings, the curves show a minimum and rise again. The non-Markovianity of the system induces a back flow of information resulting in general in a characteristic oscillating behavior. The stronger the coupling strength the larger is the memory effect. In the long time limit the system decays into its ground state and the different models yield the same state. In principal, there could be higher order coupling corrections giving a different steady state, but in our case this is not measurable. As one would suspect, the higher order terms become more important for short to intermediate times and stronger couplings.

In the next comparison in Fig. 5.2 we use the Born approximation and all the Markovian expansion terms up to order  $\mathcal{O}(g_c^6/\gamma_{\min}^5)$ . So, we directly see the influence of higher order contractions. As suspected, without the higher order contraction terms the decay is too slow as in Fig. 5.2 a). The non-exponential decay in the beginning produced by the higher order Markovian terms can be seen in both models. All models eventually decay into the ground state  $|\downarrow\rangle$ . The

trace distance again peaks, but in comparison to Fig. 5.1 b) shows no double peak structure. Interestingly, the trace distance is larger with just the Born approximation compared to trace distance with the BM approximation. This demonstrates the consequence of not adding up all terms belonging to the same order of magnitude. In summary, higher order terms in the Born expansion yield a faster decay, whereas higher order terms in the Markov expansion lead to a kind of inertia behavior.

In this section we used our model to explicitly calculate higher order corrections to the BM approximation and numerically investigate the influence of these terms. In our opinion, this is not the strength of our method, even though one advantage is that higher order terms only have to be computed once and can be used for all time steps of the simulation. The theory is more suitable in the estimation of orders of magnitude of higher order terms to justify the Born and Markov approximations or to define the parameters and time regimes in which they are valid.

### 5.3 Initial State Problem

In this section we want to show an application of our method in which we can understand physical consequences of non-Markovianity without calculating the self-energies explicitly. The problem we address is the occurrence of initial state correlations present in non-Markovian systems. If the system is always depending on its past, the investigation of an initial state which is not the steady state is not possible without considering initial state correlations with the bath.

### 5.3 Initial State Problem

---

The preparation of the excited state is important for the dynamics, therefore we introduced the driving pulse in section 5.2. To quantify the initial correlations, we cut the QME at  $t_c = 0$  and examine the limit  $t_0 \rightarrow -\infty$

$$\dot{\rho}_I(t) = \underbrace{\int_{-\infty}^0 dt' \Sigma_I^{(0)}(t-t') \rho_I(t')}_{A_0} + \underbrace{\int_0^t dt' \Sigma_I^{(0)}(t-t') \rho_I(t')}_{B_0}. \quad (5.42)$$

The initial correlations of the system are given by the term  $A_0$  and the dependence of  $\rho_I(t')$  in  $B_0$  on its past. They are non-Markovian effects and thus we use our Markov expansion from section 5.1.1 to investigate the order of magnitude of these correlations. We apply integration by parts to  $A_0$  and  $B_0$  and the  $k^{\text{th}}$  order of the Markov expansion of  $A_0$  and  $B_0$  are

$$A_k = \int_{-\infty}^0 dt' \Sigma_I^{(k)}(t-t') \rho_{I(k)}(t') \quad (5.43)$$

$$= \underbrace{\left( \int_{-\infty}^t dt' \Sigma_I^{(k)}(t') \right)}_{A_k^{\text{IC}}} \rho_{I(k)}(0) + \underbrace{\int_{-\infty}^0 dt' \Sigma_I^{(k+1)}(t-t') \rho_{I(k+1)}(t')}_{A_{k+1}},$$

$$B_k = \int_0^t dt' \Sigma_I^{(k)}(t-t') \rho_{I(k)}(t') = \underbrace{\mathcal{S}^{(k)} \rho_{I(k)}(t)}_{\text{see Eq. (5.4)}} \quad (5.44)$$

$$- \underbrace{\left( \int_{\infty}^t dt' \Sigma_{\text{I}}^{(k)}(t') \right)}_{B_k^{\text{IC}}} \rho_{I(k)}(0) + \underbrace{\int_0^t dt' \Sigma_{\text{I}}^{(k+1)}(t-t') \rho_{I(k+1)}(t')}_{B_{k+1}}.$$

In  $B_k$  the expected term from Eq. (5.4) can be recovered, but also the initial correlations appear in  $B_k^{\text{IC}}$ . As one can easily see, by adding  $A_k$  and  $B_k$  the terms  $A_k^{\text{IC}}$  and  $B_k^{\text{IC}}$  cancel and Eq. (5.4) is again exact by adding all orders in  $k$ . The simulation of an excited state without the preparation belongs to neglecting the terms  $A_k$  and the initial correlations  $B_k^{\text{IC}}$  must be considered. They are decaying like the self-energy  $\mathcal{S}^{(k)}\rho_{(k),\text{I}}(t)$  in time and are thus suppressed for  $t$  larger than  $1/\gamma_{\text{min}}$ , the maximum correlation time of the bath. But the short time behavior of the system is influenced by the non-Markovian initial correlations. With our method the order of magnitude of the initial correlations can be estimated to any order in the Markov expansion.

## 5.4 Two-Time Correlator

Another example of an application of our expansion by estimating the order of magnitude of different terms was made by Jin *et al.* in Ref. [IV]. This section is based on the work [IV] and the reference will only be cited at selected places in the text.

As already shown in this thesis, the reduced density matrix of a small quantum system enables the possibility to evaluate the expectation value  $\langle A(t) \rangle$  of any operator  $A$  of the system by calculating  $\text{Tr}_{\text{S}}\{A\rho(t)\}$ . This is a single-time expectation value and the compu-

tation is straightforward. The situation already becomes much more complicated considering two-time correlators

$$\langle A(t)B(0) \rangle = \text{Tr}_{\text{SB}}\{\rho_{\text{SB}}U(t_0, t)AU(t, 0)BU(0, t_0)\}, \quad (5.45)$$

with  $A$  and  $B$  system operators and the full time evolution of the system plus bath as in Sec. 2.3. With the Born-Markov approximation the two-time correlator is given by the quantum regression theorem [25, 26, 56]

$$\langle A(t)B(0) \rangle = \text{Tr}_{\text{S}}\{A\Pi(t, 0)B\rho(0)\}, \quad (5.46)$$

with  $\Pi(t, 0)$  the time evolution of the QME. This equation implies that the full time evolution  $\Pi(t, 0)$  is time-translational invariant. This is not the case for a non-Markovian system, i.e.,  $\Pi(t, 0) \neq \Pi(t, t')\Pi(t', 0)$ . But, Jin *et al.* [IV] could show that a very similar version of the quantum regression theorem can be found even in the case of non-Markovianity of the dynamics and in lowest order in the coupling strength, i.e., the Born approximation. To achieve this, the QME is expanded with the hierarchical QME method [99] which we will not explain here any further. The final result is

$$\langle A(t)B(0) \rangle = \text{Tr}_{\text{B}}\left\{A\left[\vec{\Pi}(t, 0)B\vec{\rho}(0)\right]\right\}, \quad (5.47)$$

where the components of the density operators in the vector are now

$$\vec{\rho}(t) = \left[\rho(t), \phi^+(\omega, t), \phi^-(\omega, t)\right]^T. \quad (5.48)$$

The matrices  $\phi^+(\omega, t)$  and  $\phi^-(\omega, t)$  are auxiliary density matrices used to take care of the non-Markovianity of the system (see Ref. [IV] and [99] for details). The initial state at  $t = 0$  is given by

$$B\vec{\rho}(0) = \{B\rho(0), B\phi^+(\omega, 0), B\phi^-(\omega, 0)\}, \quad (5.49)$$

where  $\rho(0)$  is the density matrix being time evolved from a initial time  $t_0 \rightarrow -\infty$ . Thus,  $\rho(0) = \rho_{\text{eq}}$  is the equilibrium reduced density matrix. The new object  $\vec{\Pi}(t, 0)$  is time-translational invariant and the quantum regression theorem is restored. In the derivation of the non-Markovian quantum regression theorem a full non-Markovian calculation, i.e., to all orders in the Markov expansion, with Born approximation was done. Because terms of the Markov expansion are of the same order as terms in the Born expansion as shown in Sec. 5.1.2, the range of validity of the solution needs to be checked.

To connect the two-time correlator with our theory, we sketch its derivation in the diagrammatic way. We assume that we can write the density matrix for  $t_0$  as a direct product of the reduced density matrices of the system and the bath, which is valid for the limit  $t_0 \rightarrow -\infty$ ,

$$\rho_{\text{SB}}(t_0) = \rho_{\text{B}}(t_0) \otimes \sum_{nn'} \rho_{nn'}(t_0) |n\rangle \langle n'|, \quad (5.50)$$

$$\langle A(t)B(0) \rangle = \text{Tr} \left[ \rho_{\text{B}}(t_0) \otimes \sum_{nn'} \rho_{nn'}(t_0) |n\rangle \langle n'| \right. \\ \left. U(t_0, t)AU(t, 0)BU(0, t_0) \right] \quad (5.51)$$



## 5.4 Two-Time Correlator

---

$$\begin{aligned}
 &= \sum_{n,n'} \rho_{nn'}(t_0) \\
 &\quad \langle n' | \text{Tr}_B \left\{ \rho_B(t_0) U(t_0, t) A U(t, 0) \hat{B} U(0, t_0) \right\} | n \rangle, \quad (5.52)
 \end{aligned}$$

where  $|n\rangle$  is a basis set for the system. By changing to the interaction picture the equation can be further simplified. The exponential functions  $U_I(t, t')$  expanded in the coupling strength between bath and system yields

$$\begin{aligned}
 U_I(t_0, t) A_I(t) U_I(t, 0) B_I(0) U_I(0, t_0) &= A_I(t) B_I(0) \\
 &+ \int_0^t dt_1 \int_0^{t_1} dt_2 H_{C,I}(t_1) A_I(t) H_{C,I}(t_2) B_I(0) \\
 &- \int_0^t dt_1 \int_0^{t_1} dt_2 H_{C,I}(t_2) H_{C,I}(t_1) A_I(t) B_I(0) + \dots, \quad (5.53)
 \end{aligned}$$

$$\begin{aligned}
 \langle A(t) B(0) \rangle &= \text{Diagram 1} + \text{Diagram 2} \\
 &+ \text{Diagram 3} + \text{Diagram 4} + \dots \quad (5.54)
 \end{aligned}$$

The diagrams represent terms in the expansion of the correlator. Each diagram shows a horizontal line representing the bath, with a vertical line representing the system operator. The bath line starts at  $B_I(0)$  and ends at  $A_I(t)$ . The system operator is represented by a vertical line with a dot at the top. The diagrams show different ways the system operator can interact with the bath through the coupling Hamiltonian  $H_C$ .

This leads to

$$\langle \hat{A}(t) \hat{B}(0) \rangle = \sum_{n,n'} \rho_{nn'}(t_0) \prod_{nn'}(t_0, A_I(t), B_I(0)). \quad (5.55)$$

Each dot in a diagram denotes a coupling Hamiltonian  $H_C$ . The superoperator  $\prod_{nn'}(t_0, A_I(t), B_I(0))$  is the full time evolution of the density matrix including the two operators  $A$  and  $B$ . By using Wicks theorem the trace over the bath decays into two point functions rep-

resented by a contraction between the dots resulting in

$$\underbrace{\Pi}_{B_I(0)} \bullet A_I(t) = \underbrace{\Pi \mid \Pi}_{B_I(0)} \bullet A_I(t) + \underbrace{\Pi \mid \Sigma_B \mid \Pi}_{B_I(0)} \bullet A_I(t). \quad (5.56)$$

Here,  $\Sigma_B$  is the self-energy of the vertex correction including the operator  $B$  and contains all the inseparable diagrams. Eq. 5.56 is still exact. The first diagram corresponds to the Markov approximation, i.e., the possibility to cut the propagator  $\Pi$  at time  $t = 0$  while the second diagram contains contractions over the vertex  $B$ . This equation rewritten in algebraic form is

$$\begin{aligned} \langle A(t)B(0) \rangle &= \text{Tr} \{ A_I(t) \Pi(t, 0) B_I(0) \Pi(0, t_0) \rho(t_0) \\ &+ \int_0^t dt_2 \int_{t_0}^0 dt_1 A_I(t) \Pi(t, t_2) \Sigma_B(t_2, t_1) \Pi(t_1, t_0) \rho(t_0) \}. \end{aligned} \quad (5.57)$$

In the following, we assume that  $t_0 \rightarrow -\infty$  and the reduced density matrix at  $t = 0^-$  is in equilibrium  $\rho_{\text{eq}}$ . This formalism can be used to discuss the range of validity of the non-Markovian correlation function. As shown in Sec. 5.1.2, non-Markovian effects are in general of the same order as higher order contractions in the self-energy. However, for this correlation function we have a well defined time scale and for short times scales, the combination of non-Markovian QME and lowest order self-energy can be valid.

We investigate the short time behavior of the two-time correlator and therefore have a closer look at the Taylor expansion of the time-derivative of the correlation function, i.e.,  $G(t) = \frac{d\langle A(t)B(0) \rangle}{dt}$  for small

$t = 0^+$ ,

$$G(t) = G(0) + \left. \frac{dG(t)}{dt} \right|_{t=0} t + \frac{1}{2} \left. \frac{d^2G(t)}{dt^2} \right|_{t=0} t^2 + \dots \quad (5.58)$$

For the first terms, this can be written in the explicit form

$$\begin{aligned} G(t) = & \text{Tr} \left[ A \int_0^\infty dt \Sigma_B(t) \rho_{\text{eq}} \right] + \text{Tr} \{ A [\Sigma(0)B + \Sigma_B(0)] \rho_{\text{eq}} \} t \\ & + \frac{1}{2} \text{Tr} \left\{ A [\dot{\Sigma}(0)B + \dot{\Sigma}_B(0)] \rho_{\text{eq}} \right\} t^2 + \dots \end{aligned} \quad (5.59)$$

Following the estimation of the order of magnitude of the self-energy from Sec. 5.1.2, we roughly get

$$\begin{aligned} G(t) \sim & \text{Tr} [A f_2(s_{i,I}, B, \rho_{\text{eq}})] \sum_l \frac{g_C^{2l}}{\gamma_{\min}^{2l-1}} \\ & + \text{Tr} \{ A [f_1(s_{i,I})B \rho_{\text{eq}} + f_2(s_{i,I}, B, \rho_{\text{eq}})] \} \sum_l \frac{g_C^{2l}}{\gamma_{\min}^{2l-2}} t \\ & + \frac{1}{2} \text{Tr} \{ A [f_1(s_{i,I})B \rho_{\text{eq}} + f_2(s_{i,I}, B, \rho_{\text{eq}})] \} \sum_l \frac{g_C^{2l}}{\gamma_{\min}^{2l-3}} t^2 \\ & + \dots, \end{aligned} \quad (5.60)$$

where  $\gamma_{\min}$  is the smallest decay rate of the correlation function of the bath (see Sec. 5.1.2),  $f_1(s_{i,I})$  and  $f_2(s_{i,I}, B, \rho_{\text{eq}})$  are the formal expressions, i.e., the matrix elements arising from  $\Sigma_B$  and  $\Sigma$ , respectively. We assume that the magnitudes of  $f_1(s_{i,I})B \rho_{\text{eq}}$  and  $f_2(s_{i,I}, B, \rho_{\text{eq}})$  have the same order of magnitude. Altogether, for times  $t \lesssim 1/\gamma_{\min}$  all the terms of the Markov expansion need to be taken into account,

but the sums can be truncated at the lowest order coupling  $l = 1$ , i.e., the Born approximation,

$$\begin{aligned} & \frac{g_C^2}{\gamma_{\min}} + g_C^2 \cdot t + g_C^2 \gamma_{\min} \cdot t^2 + \dots \\ & > \frac{g_C^4}{\gamma_{\min}^3} + \frac{g_C^4}{\gamma_{\min}^2} \cdot t + \frac{g_C^4}{\gamma_{\min}} \cdot t^2 + \dots > \dots, \text{ for } t < \frac{1}{\gamma_{\min}}. \end{aligned} \tag{5.61}$$

# 6 Chapter

---

## Conclusion

The field of nanoelectronics is rapidly growing and new technological devices are announced more and more frequently. This thesis contributes to this important field by giving new insights in the theoretical description of nanoelectronics by the quantum master equation (QME). On the one hand, we investigated two practical important systems, i.e., magnetic adatoms on metallic surfaces and double-quantum dot (DQD) lasing. On the other hand, we explored the foundation and basic properties of the QME.

In chapter 3, the dynamics of the total angular momentum states of holmium (Ho) atoms on platinum (Pt) with (111) surface configuration were analyzed with our computational tool which is able to simulate also complex QME. The work was previously reported in publication [III]. We identified an important regime of parameters where the system behaves deeply quantum mechanically. It cannot be described by rate equations for transitions between the eigenstates

---

of the crystal-field Hamiltonian  $H_{\text{CF}}$ , as it was done before for other magnetic adatom systems [34–38]. Instead, the system has to be treated by the full quantum master equation. In general, its steady-state basis differs from the  $H_{\text{CF}}$  eigenstates. This is an example of the *environment-induced superselection* principle [39, 60]. We analyzed how the relaxation time  $T_1$  depends on various parameters of the system. In ideal situations at low temperatures it should be extremely long. In contrast, the decoherence time  $T_2$  is always very short. We further described a method to initialize the system in one of the two ground states by suitable voltage pulses. By adjusting the parameters describing deviations from the ideal situation we could roughly fit the experiments, with their remarkably long lifetimes.

Our analysis showed that with more precise and improved parameter control, the system would acquire even longer lifetimes than observed already. The system therefore promises to be useful as a single-atom memory with the possibility to address the memory by short pulses of electric currents with high fidelity. On the other hand, at this stage, we have to conclude that there is too little experimental data available to determine the parameters independently. A further detailed investigation of the coupling parameter  $c_{\text{TB}}$  including the scattering strength of an electron tunneling between tip and bulk via the atom and the other parameters is required to identify the main perturbation limiting the lifetime of the Ho adatom in the experiment. The lifetime depends strongly on an applied magnetic field. Analysis of this effect would help to obtain the missing information of the parameters. One interesting extension of the presented work would be a classification of possible stable combinations of other

---

adatoms and symmetries of the adsorption site. Perhaps even better setups than Ho and Pt(111) with similar symmetry protection against scattering could be found.

The second system investigated in chapter 4 is a double quantum dot system coupled to a microwave oscillator. The results were published in Ref. [V] of the publication list. Electron transport through the system may lead to a lasing state (strictly speaking a “masing” state) with a narrow resonance peak in the photon number as a function of the detuning tending towards a Poisson distribution [40, 41]. It is interesting that this property of the photon field is reflected also in a peak in the transport current providing an alternative to study the lasing state. We extended earlier work on dots with one level each [41] to dots with multiple levels. As one could expect, we see several peaks similar to the situation with a single level in each dot but also qualitatively different ones. In particular, we observed a backward tunneling process in a cascade of transitions leading to a lasing peak in the photon number associated with a dip in the transport current.

These multi-level processes involve inelastic transitions, which may occur in the presence of phonons. We therefore analyzed the multi-level DQD-microwave oscillator system coupled to piezoelectric acoustic phonons. We used realistic parameters, taken from the experiments of Liu *et al.* [49], including the phonon spectrum as determined in this reference. The lasing peaks and the Fano factor are sensitive to the coupling strength as well as the spectrum and may provide a tool to analyze phonon properties in more detail. We extended earlier work with single levels in each dot to multiple levels and conducted a detailed analysis of the coupling to phonons. Both

investigations were covered by the QME. The description accounts for various quantum properties, such as lasing, but we also see the effect of two-photon transitions. Further physical properties of the system, e.g., spin-degrees of freedom leading to spin-blockade effects [100] or spin-photon coupling [101], could be implemented in this framework.

In chapter 5, we developed an exact expansion of the QME in the coupling strength to the environment and in the environment correlation time. This was presented before in publication [II]. The approach allows a physical interpretation of the different expansion terms, thus providing a better understanding of the QME as compared to the standard textbook derivation presented in chapter 2. In particular, the relation between the Born and Markov expansions become clear. Higher order terms in the Born expansion are of the same order of magnitude as higher order non-Markovian terms. This is remarkable since many investigations of non-Markovian effects use the Born approximation without specifying the time scales of the problem [85, 87, 88, 102].

The interest in non-Markovian models has grown, on the one hand, because of recent experiments [103, 104], and ,on the other hand, because of theoretical predictions of, e.g., noise cancellation [105] or improved decoherence times [106]. Therefore, an investigation of the system beyond the Markovian approximation also requires in general going beyond Born approximation, despite, e.g., short timescales. We demonstrated this in Sec. 5.2 with the spin-boson model. In addition, non-Markovianity is important for initial state correlations [25, 55, 107, 108], which can be quantified with our expansion (see Sec. 5.3). Specific terms can be identified as initial correlations by cutting the



---

exact time evolution and can be calculated in principle to all orders. This expansion also provides a convenient tool to estimate the validity of the common Born, Markov and initial state approximation and an approach to go beyond. As an example, we showed the non-Markovian effects on two-time correlators and estimated the range of the validity of the model in Sec. 5.4.



# A

Chapter

---

## Appendix

### A.1 Implementation of the QME

In this Appendix we want to present the general form of the implementation of the QME in program-code as it was done in all the simulations in this thesis [II, III, V] and is nicely reviewed in Ref. [109]. The general form of the master equation is given by Eq. (2.36)

$$\dot{\rho}(t) = i[\rho(t), H_S] + \int_{t_0}^t dt' \Sigma(t', t) \rho(t'). \quad (\text{A.1})$$

The self-energy  $\Sigma(t', t)$  contains system operators from the coupling between system and bath in combination with the reduced density matrix  $\rho(t')$ . With the help of our Born-Markov expansion from Sec. 5.1.2, we can simplify this part to terms which are combinations of the reduced density matrix  $\rho(t)$  at time  $t$  or derivatives of  $\rho(t)$ . In the simplest and most important case of the Born-Markov

approximation the QME can be written as

$$\begin{aligned} \dot{\rho}_I(t) = & - \sum_{ij} \int_{t_0}^t dt' [s_i(t)s_j(t')\rho_I(t) - s_j(t')\rho_I(t)s_i(t)] C_{ij}(t-t') \\ & + [\rho_I(t)s_j(t')s_i(t) - s_i(t)\rho_I(t)s_j(t')] C_{ji}(t'-t). \end{aligned} \quad (\text{A.2})$$

But also for higher order QME with several correlation functions the structure of the equation remains the same

$$\begin{aligned} \rho_{(1)}(t) = & i [\rho_{(0)}(t), H_S] - \sum_{\substack{ij \\ k=0}} [S_i S_j \rho_{(k)}(t) \Gamma_{ij}^{(k)} - S_j \rho_{(k)}(t) S_i \Gamma_{ij}^{(k)'}] \\ & + [\rho(t) S_j S_i \Gamma_{ji}^{(k)} - S_i \rho(t) S_j \Gamma_{ji}^{(k)'}]. \end{aligned} \quad (\text{A.3})$$

Here, again the index  $k$  at the reduced density matrix labels the derivative of  $\rho(t)$ . The operators  $S_i$  can be arbitrary multiplications of system operators  $s_i$  depending on the number of contractions and the order in the diagram. The rate  $\Gamma_{ij}^{(k)}$  is defined via the in general multiple correlation functions and the evaluation of the time integrals. For simplicity we will consider only  $k = 0$ , but the generalization is straightforward. This equation written in the basis  $\{|n\rangle\}_{n=1,2,\dots,d}$ , e.g., the system eigenbasis with dimension  $d$ , is just a system of coupled ordinary differential equations [109] of the matrix elements  $\rho_{nm}(t) = \langle n|\rho(t)|m\rangle$

$$\dot{\rho}_{nm}(t) = \sum_{l=1}^d i (\rho(t)_{nl} H_{Slm} - H_{Snl} \rho(t)_{lm})$$

## A.1 Implementation of the QME

---

$$\begin{aligned}
 & - \sum_{\substack{ij \\ vu=1}} \left[ S_{inu} S_{juv} \rho_{vm}(t) \Gamma_{ij} - S_{jnu} \rho_{uv}(t) S_{ivm} \Gamma'_{ij} \right] \\
 & + \left[ \rho_{nu}(t) S_{juv} S_{ivm} \Gamma_{ji} - S_{inu} \rho_{uv}(t) S_{jvm} \Gamma'_{ji} \right]. \quad (\text{A.4})
 \end{aligned}$$

By introducing the vectorization of a matrix  $\text{vec}\{\cdot\}$  meaning the rewriting of a matrix row by row as a vector the equation can be simplified to the form [109]

$$\text{vec}\{\rho(t)\} = \vec{\rho}(t) = (\rho_{11}, \rho_{12}, \dots, \rho_{d1}, \rho_{d2}, \dots, \rho_{dd})^T \quad (\text{A.5})$$

$$\dot{\vec{\rho}}(t) = \mathcal{M} \vec{\rho}(t). \quad (\text{A.6})$$

The superoperator  $\mathcal{M}$  is derived with the relation

$$\text{vec}\{AXB\} = (A \otimes B^T) \text{vec}\{X\}, \quad (\text{A.7})$$

where  $A$ ,  $X$  and  $B$  are matrices and the symbol  $\otimes$  is the Kronecker defined as

$$A \otimes B = \begin{bmatrix} a_{11}B & \cdots & a_{1n}B \\ \vdots & \ddots & \vdots \\ a_{m1}B & \cdots & a_{mn}B \end{bmatrix}. \quad (\text{A.8})$$

In our case, we can transform the different terms of the QME by inserting identity matrices, e.g.,

$$\text{vec}\{\rho(t)H_S\} = \text{vec}\{\mathbf{1}\rho(t)H_S\} = (\mathbf{1} \otimes [H_S]^T) \vec{\rho}(t), \quad (\text{A.9})$$

$$\text{vec}\{S_j \rho(t) S_i\} = (S_j \otimes S_i^T) \vec{\rho}(t). \quad (\text{A.10})$$

Eventually, the superoperator  $\mathcal{M}$  is given by

$$\mathcal{M} = \mathcal{M}_C + \mathcal{M}_D \quad (\text{A.11})$$

$$\mathcal{M}_C = i \left( \mathbf{1} \otimes H_S^T - H_S \otimes \mathbf{1} \right) \quad (\text{A.12})$$

$$\begin{aligned} \mathcal{M}_D = & - \sum_{ij} \left[ (S_i S_j \otimes \mathbf{1}) \Gamma_{ij} - (S_j \otimes S_i^T) \Gamma'_{ij} \right. \\ & \left. + \left( \mathbf{1} \otimes [S_j S_i]^T \right) \Gamma_{ji} - (S_i \otimes S_j^T) \Gamma'_{ji} \right], \end{aligned} \quad (\text{A.13})$$

with  $\mathcal{M}_C$  the coherent and  $\mathcal{M}_D$  the dissipative part of the QME. The Eq. (A.6) is solved by the matrix exponential of  $\mathcal{M}$

$$\vec{\rho}(t) = e^{\mathcal{M}t} \vec{\rho}(0). \quad (\text{A.14})$$

It is possible to expand the solution for the reduced density matrix  $\vec{\rho}(t)$  in eigenvectors and exponentials of the eigenvalues of  $\mathcal{M}$

$$\mathcal{M} \vec{\rho}_n = m_n \vec{\rho}_n \quad (\text{A.15})$$

$$\vec{\rho}(t) = \sum_{n=0}^{d^2} c_n \vec{\rho}_n e^{m_n t} \quad (\text{A.16})$$

The eigenvalues  $m_n$  have the property that  $m_0 = 0$  and all other  $n > 0$  are negative  $m_n < 0$ . The prefactors  $c_n$  are fixed by the initial condition

$$\vec{\rho}(0) = \sum_{n=0}^{d^2} c_n \vec{\rho}_n. \quad (\text{A.17})$$

## A.1 Implementation of the QME

---

From the construction of this expansion it is clear that the steady state solution  $t \rightarrow \infty$  corresponds to the eigenvector with zero eigenvalue  $m_0$ , i.e.,  $\vec{\rho}_0 = \vec{\rho}_{\text{St}}$ . All other contributions of the other eigenvectors are exponentially suppressed. In addition, further properties of the eigenvectors can be extracted from Eq. (A.16). Because the reduced density matrix  $\rho(t)$  and the steady state density matrix  $\rho_{\text{St}}$  have to fulfill the properties of a density matrix, in particular that their traces are one, all the other eigenvectors of  $\mathcal{M}$  with  $n > 0$  can not change the trace. This implies that they (rewritten as matrices) have trace zero and are no density matrices. In fact, they can be interpreted as transitions channels. Thus, a spectral decomposition of the superoperator  $\mathcal{M}$  like in Eq. (A.15) gives access to the steady state and all the transition rates between the steady state basis states [75].

We want to give a small example how to implement the Eqs. (A.13) and (A.15) in Mathematica with the simple  $S_i = S_j = J_z$  coupling term.

```
1 CorP=Table[0, {k, 1, d}, {1, 1, d}];
2 CorM=Table[0, {k, 1, d}, {1, 1, d}];
3 {EigVal, EigVec} = Eigensystem[Hs];
4 EigVec = Transpose[EigVec];
5 JzNew=Inverse[EigVec].Jz.EigVec;
6 For[k = 1, k < (d+1), k++,
7   For[l = 1, l < (d+1), l++,
8     CorP[[k, l]] = CorFunc[EigVal[[l]] - EigVal[[k]]];
9     CorM[[k, l]] = CorFunc[EigVal[[k]] - EigVal[[l]]];
10  ];
```

```

11 ];
12 MCoherent= -I ( KroneckerProduct [Hs,
      IdentityMatrix [d]] - KroneckerProduct [
      IdentityMatrix [d], Transpose [Hs]]) /hbar ;
13 MDiss= - ( KroneckerProduct [JzNew . (JzNew*CorP),
      IdentityMatrix [d]] - KroneckerProduct [(JzNew*
      CorP), Transpose [JzNew]] + KroneckerProduct [
      IdentityMatrix [d], Transpose [(JzNew*CorM) .
      JzNew]] - KroneckerProduct [JzNew, Transpose [
      JzNew*CorM]]) ;
14 MTot=MCoherent+MDiss ;
15 {MVal, MVec}=Eigensystem [MTot];
16 rhoSteady=MVec[[ -1]];
17 scaling=Tr [ArrayReshape [rhoSteady, {d, d}]];
18 rhoSteady=(1/scaling)*rhoSteady ;

```

Here,  $H_s$  can be an arbitrary system Hamiltonian with dimension  $d$ .

## A.2 Higher Order Diagrams in the Spin-Boson Model

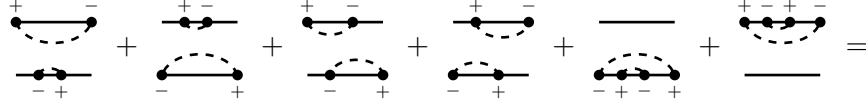
As an example, we show the diagrams of the spin-boson model investigated in Sec. 5.2 for  $k = 0$  (Markov approximation) and two contractions  $n_c$  which couple the reduced density matrix element  $\rho_{\uparrow\uparrow}$



## A.2 Higher Order Diagrams in the Spin-Boson Model

---

to itself



$$\begin{aligned}
 & \int_{\omega_1^<} \int_{\omega_2^<} \left[ \left( \pi \delta(\omega_1 - \Delta E) + \text{P} \frac{i}{\omega_1 - \Delta E} \right) \right. \\
 & \cdot \left( \pi \delta(\Delta E - \omega_2) + \text{P} \frac{i}{\Delta E - \omega_2} \right) \left( \pi \delta(\omega_1 - \omega_2) + \text{P} \frac{i}{\omega_1 - \omega_2} \right) \\
 & + \left( \pi \delta(\omega_1 - \Delta E) - \text{P} \frac{i}{\omega_1 - \Delta E} \right) \left( \pi \delta(\Delta E - \omega_2) - \text{P} \frac{i}{\Delta E - \omega_2} \right) \\
 & \cdot \left( \pi \delta(\omega_1 - \omega_2) - \text{P} \frac{i}{\omega_1 - \omega_2} \right) \\
 & + \left( \pi \delta(\Delta E - \omega_1) + \text{P} \frac{i}{\Delta E - \omega_1} \right)^2 \left( \pi \delta(\omega_2 - \omega_1) + \text{P} \frac{i}{\omega_2 - \omega_1} \right) \\
 & + \left( \pi \delta(\Delta E - \omega_1) - \text{P} \frac{i}{\Delta E - \omega_1} \right)^2 \left( \pi \delta(\omega_2 - \omega_1) - \text{P} \frac{i}{\omega_2 - \omega_1} \right) \\
 & + \left( \pi \delta(\Delta E - \omega_1) + \text{P} \frac{i}{\Delta E - \omega_1} \right) \left( \pi \delta(\omega_2 - \Delta E) + \text{P} \frac{i}{\omega_2 - \Delta E} \right) \\
 & \cdot \left( \pi \delta(\omega_2 - \omega_1) + \text{P} \frac{i}{\omega_2 - \omega_1} \right) + \left( \pi \delta(\Delta E - \omega_1) - \text{P} \frac{i}{\Delta E - \omega_1} \right) \\
 & \cdot \left. \left( \pi \delta(\omega_2 - \Delta E) - \text{P} \frac{i}{\omega_2 - \Delta E} \right) \left( \pi \delta(\omega_2 - \omega_1) - \text{P} \frac{i}{\omega_2 - \omega_1} \right) \right] \\
 & = \int_{\omega_1^<} \int_{\omega_2^<} 6\pi^3 \delta(\dots)^3 + \int_{\omega_1^<} \int_{\omega_2^<} 3\pi \left( \underbrace{-\frac{\text{P}\delta(\omega_1 - \omega_2)}{(\omega_1 - \Delta E)^2} + \frac{\text{P}\delta(\omega_1 - \omega_2)}{(\omega_1 - \Delta E)(\omega_2 - \Delta E)}}_{=0} \right. \\
 & \left. - \underbrace{\frac{\text{P}2\delta(\omega_1 - \Delta E)}{(\omega_1 - \Delta E)(\omega_1 - \omega_2)}}_{=0(\text{PV})} - \underbrace{\frac{\text{P}\delta(\Delta E - \omega_2)}{(\omega_1 - \Delta E)(\omega_1 - \omega_2)} + \frac{\text{P}\delta(\omega_1 - \Delta E)}{(\omega_2 - \Delta E)(\omega_1 - \omega_2)}}_{=0} \right) \quad (\text{A.18})
 \end{aligned}$$

The parts which contain the principal values cancel.



## References

- [1] G. E. Moore, *Cramming More Components onto Integrated Circuits*, Proc. IEEE, **86**, 82 (1998).
- [2] NASA, <http://www.hq.nasa.gov/office/pao/History/computers/Ch2-5.html> (20.01.2016).
- [3] IBM, <http://www-03.ibm.com/press/us/en/pressrelease/47301.wss> (20.01.2016).
- [4] M. Waldrop, *The chips are down for Moore's law*, Nature **530**, 144 (2016).
- [5] Storaenewsletter, <http://www.storaenewsletter.com/rubriques/market-reportsresearch/ihs-isuppli-storage-space/> (20.01.2016).
- [6] A. Einstein, *Zur Quantentheorie der Strahlung*, Phys. Z. **18**, 121 (1917).
- [7] J. McKeever, A. Boca, A. D. Boozer, J. R. Buck, and H. J. Kimble, *Experimental realization of a one-atom laser in the regime of strong coupling*, Nature **425**, 268 (2003).
- [8] O. Astafiev, K. Inomata, A. O. Niskanen, T. Yamamoto, Y. A. Pashkin, Y. Nakamura, and J. S. Tsai, *Single artificial-atom lasing*, Nature **449**, 588 (2007).
- [9] S. André, P.-Q. Jin, V. Brosco, J. H. Cole, A. Romito, A. Shnirman, and G. Schön, *Single-qubit lasing in the strong-coupling regime*, Phys. Rev. A **82**, 053802 (2010).

- 
- [10] Y.-X. Liu, L. F. Wei, and F. Nori, *Generation of nonclassical photon states using a superconducting qubit in a microcavity*, Europhys. Lett. **67**, 941 (2004).
- [11] R. J. Schoelkopf and S. M. Girvin, *Wiring up quantum systems*, Nature **451**, 664 (2008).
- [12] J. Majer, J. M. Chow, J. M. Gambetta, J. Koch, B. R. Johnson, J. A. Schreier, L. Frunzio, D. I. Schuster, A. A. Houck, A. Wallraff, A. Blais, M. H. Devoret, S. M. Girvin, and R. J. Schoelkopf, *Coupling superconducting qubits via a cavity bus*, Nature **449**, 443 (2007).
- [13] I. Chiorescu, P. Bertet, K. Semba, Y. Nakamura, C. J. P. M. Harmans, and J. E. Mooij, *Coherent dynamics of a flux qubit coupled to a harmonic oscillator*, Nature **431**, 159 (2004).
- [14] A. Wallraff, D. I. Schuster, A. Blais, L. Frunzio, R.-S. Huang, J. Majer, S. Kumar, S. M. Girvin, and R. J. Schoelkopf, *Strong coupling of a single photon to a superconducting qubit using circuit quantum electrodynamics*, Nature **431**, 162 (2004).
- [15] A. Blais, R.-S. Huang, A. Wallraff, S. Girvin, and R. J. Schoelkopf, *Cavity quantum electrodynamics for superconducting electrical circuits: An architecture for quantum computation*, Phys. Rev. A **69**, 062320 (2004).
- [16] M. Devoret and C. Glattli, *Single-electron transistors*, Phys. World **11**, 29 (1998).
- [17] J. P. Pekola, O.-P. Saira, V. F. Maisi, A. Kemppinen, M. Mötönen, Y. A. Pashkin, and D. V. Averin, *Single-electron current sources: Toward a refined definition of the ampere*, Rev. Mod. Phys. **85**, 1421–1472 (2013).

## References

---

- [18] D. V. Averin and K. K. Likharev, *Coulomb Blockade of Single-Electron Tunneling, and Coherent Oscillations in Small Tunnel Junctions*, J. Low Temp. Phys. **62**, 345 (1986).
- [19] L. L. Sohn, L. P. Kouwenhoven, and G. Schön, *Mesoscopic Electron Transport* (Kluwer, Dordrecht, 1997).
- [20] L. P. Kouwenhoven, A. T. Johnson, N. C. van der Vaart, C. J. P. M. Harmans, and C. T. Foxon, *Quantized current in a quantum-dot turnstile using oscillating tunnel barriers*, Phys. Rev. Lett. **67**, 1626 (1991).
- [21] P. Shor, *Polynomial-Time Algorithms for Prime Factorization and Discrete Logarithms on a Quantum Computer*, SIAM J. Sci. Statist. Comput. **26**, 1484 (1996).
- [22] L. K. Groover, *A fast quantum mechanical algorithm for database search*, Proceedings, STOC p. 212 (1996).
- [23] A. Fert, P. Grunberg, A. Barthelemy, F. Petroff, and W. Zinn, *Layered magnetic structures: interlayer exchange coupling and giant magnetoresistance*, J. Magn. Magn. Mater. **140**, 1 (1995).
- [24] M. Hilbert and P. Lopez, *The World's Technological Capacity to Store, Communicate, and Compute Information*, Science Exp. **1**, 1 (2011).
- [25] H.-P. Breuer and F. Petruccione, *The theory of open quantum systems* (Oxford Univ. Press, Oxford, 2003), 1st ed.
- [26] H. J. Carmichael, *Statistical Methods in Quantum Optics 1* (Springer-Verlag Berlin Heidelberg New York, 2002).
- [27] S. Datta, *Electronic Transport in Mesoscopic Systems* (Cambridge University Press (Cambridge), 1997).

- 
- [28] P. Gambardella, S. Rusponi, M. Veronese, S. S. Dhesi, C. Grazioli, A. Dallmeyer, I. Cabria, R. Zeller, P. H. Dederichs, K. Kern, C. Carbone, and H. Brune, *Giant Magnetic Anisotropy of Single Cobalt Atoms and Nanoparticles*, *Science* **300**, 1130 (2003).
- [29] A. A. Khajetoorians, S. Lounis, B. Chilian, A. T. Costa, L. Zhou, D. L. Mills, J. Wiebe, and R. Wiesendanger, *Itinerant Nature of Atom-Magnetization Excitation by Tunneling Electrons*, *Phys. Rev. Lett.* **106**, 037205 (2011).
- [30] T. Balashov, T. Schuh, A. Takacs, A. Ernst, S. Ostanin, J. Henk, I. Mertig, P. Bruno, T. Miyamachi, S. Suga, and W. Wulfhekel, *Magnetic Anisotropy and Magnetization Dynamics of Individual Atoms and Clusters of Fe and Co on Pt(111)*, *Phys. Rev. Lett.* **102**, 257203 (2009).
- [31] A. Kubetzka, M. Bode, O. Pietzsch, and R. Wiesendanger, *Spin-Polarized Scanning Tunneling Microscopy with Antiferromagnetic Probe Tips*, *Phys. Rev. Lett.* **88**, 057201 (2002).
- [32] A. A. Khajetoorians, B. Baxevanis, C. Hubner, T. Schlenk, S. Krause, T. O. Wehling, S. Lounis, A. Lichtenstein, D. Pfannkuche, J. Wiebe, and R. Wiesendanger, *Current-Driven Spin Dynamics of Artificially Constructed Quantum Magnets*, *Science* **339**, 55 (2013).
- [33] M. Steinbrecher, A. Sonntag, M. d. S. Dias, M. Bouhassoune, S. Lounis, J. Wiebe, R. Wiesendanger, and A. A. Khajetoorians, *Absence of a spin-signature from a single Ho adatom as probed by spin-sensitive tunneling*, *Nat. Comms.* **7**, 10454 (2016).
- [34] F. Delgado, J. J. Palacios, and J. Fernandez-Rossier, *Spin-Transfer Torque on a Single Magnetic Adatom*, *Phys. Rev. Lett.* **104**, 026601 (2010).

## References

---

- [35] C. F. Hirjibehedin, C.-Y. Lin, A. F. Otte, M. Ternes, C. P. Lutz, B. A. Jones, and A. J. Heinrich, *Large Magnetic Anisotropy of a Single Atomic Spin Embedded in a Surface Molecular Network*, *Science* **317**, 1199 (2007).
- [36] J. Fransson, *Spin Inelastic Electron Tunneling Spectroscopy on Local Spin Adsorbed on Surface*, *Nano Lett.* **9**, 2414 (2009).
- [37] C. Hübner, B. Baxevanis, A. A. Khajetoorians, and D. Pfannkuche, *Symmetry effects on the spin switching of adatoms*, *Phys. Rev. B* **90**, 155134 (2014).
- [38] S. Loth, K. von Bergmann, M. Ternes, A. F. Otte, C. P. Lutz, and A. J. Heinrich, *Controlling the state of quantum spins with electric currents*, *Nat. Phys.* **6**, 340 (2010).
- [39] W. H. Zurek, *Preferred States, Predictability, Classicality and the Environment-Induced Decoherence*, *Prog. Theo. Phys.* **89**, 281 (1993).
- [40] L. Childress, A. S. Sørensen, and M. D. Lukin, *Mesoscopic cavity quantum electrodynamics with quantum dots*, *Phys. Rev. A* **69** (2004).
- [41] P.-Q. Jin, M. Marthaler, J. H. Cole, A. Shnirman, and G. Schön, *Lasing and transport in a quantum-dot resonator circuit*, *Phys. Rev. B* **84**, 035322 (2011).
- [42] J. Jin, M. Marthaler, P.-Q. Jin, D. Golubev, and G. Schön, *Noise spectrum of a quantum dot–resonator lasing circuit*, *New J. Phys.* **15**, 025044 (2013).
- [43] S. Vorojtsov, E. R. Mucciolo, and H. U. Baranger, *Phonon decoherence of a double quantum dot charge qubit*, *Phys. Rev. B* **71**, 205322 (2005).

- 
- [44] M. J. Gullans, Y.-Y. Liu, J. Stehlik, J. R. Petta, and J. M. Taylor, *Phonon-Assisted Gain in a Semiconductor Double Quantum Dot Maser*, Phys. Rev. Lett. **114**, 196802 (2015).
- [45] M. Marthaler, Y. Utsumi, and D. S. Golubev, *Lasing in circuit quantum electrodynamics with strong noise*, Phys. Rev. B **91**, 184515 (2015).
- [46] T. Frey, P. J. Leek, M. Beck, A. Blais, T. Ihn, K. Ensslin, and A. Wallraff, *Dipole Coupling of a Double Quantum Dot to a Microwave Resonator*, Phys. Rev. Lett. **108**, 046807 (2012).
- [47] J. Basset, D.-D. Jarausch, A. Stockklauser, T. Frey, C. Reichl, W. Wegscheider, T. M. Ihn, K. Ensslin, and A. Wallraff, *Single-electron double quantum dot dipole-coupled to a single photonic mode*, Phys. Rev. B **88**, 125312 (2013).
- [48] Y.-Y. Liu, J. Stehlik, C. Eichler, M. J. Gullans, J. M. Taylor, and J. R. Petta, *Semiconductor double quantum dot micro-maser*, Science **347**, 285 (2015).
- [49] Y.-Y. Liu, K. D. Petersson, J. Stehlik, J. M. Taylor, and J. R. Petta, *Photon Emission from a Cavity-Coupled Double Quantum Dot*, Phys. Rev. Lett. **113**, 036801 (2014).
- [50] A. Stockklauser, V. F. Maisi, J. Basset, K. Cujia, C. Reichl, W. Wegscheider, T. Ihn, A. Wallraff, and K. Ensslin, *Microwave Emission from Hybridized States in a Semiconductor Charge Qubit*, Phys. Rev. Lett. **115**, 046802 (2015).
- [51] J. Colless, X. Croot, T. Stace, A. Doherty, S. Barrett, H. Lu, A. Gossard, and D. Reilly, *Raman phonon emission in a driven double quantum dot*, Nat. Comms. **5**, 1 (2014).



- [52] J. J. Viennot, M. R. Delbecq, M. C. Dartiailh, A. Cottet, and T. Kontos, *Out-of-equilibrium charge dynamics in a hybrid circuit quantum electrodynamics architecture*, Phys. Rev. B **89** (2014).
- [53] H.-P. Breuer, B. Kappler, and F. Petruccione, *The Time-Convolutionless Projection Operator Technique in the Quantum Theory of Dissipation and Decoherence*, Ann. Phys. **291**, 36 (2001).
- [54] G. Clos and H.-P. Breuer, *Quantification of memory effects in the spin-boson model*, Phys. Rev. A **86**, 012115 (2012).
- [55] H. Breuer, E. Laine, J. Piilo, and B. Vacchini, *Non-Markovian dynamics in open quantum systems*, ArXiv e-prints (2015).
- [56] M. Lax, *Formal Theory of Quantum Fluctuations from a Driven State*, Phys. Rev. **129**, 2342 (1963).
- [57] H. Schoeller and G. Schön, *Mesoscopic quantum transport: Resonant tunneling in the presence of a strong Coulomb interaction*, Phys. Rev. B **50**, 18436 (1994).
- [58] J. König, H. Schoeller, and G. Schön, *Resonant Tunneling and Coulomb Oscillations*, Europhys. Lett. **31**, 31 (1995).
- [59] M. Marthaler and J. Leppäkangas, *Diagrammatic description of a quantum system coupled to strong noise*, ArXiv e-prints (2015).
- [60] W. H. Zurek, *Decoherence, einselection, and the quantum origins of the classical*, Rev. Mod. Phys. **75**, 715 (2003).
- [61] S. Loth, M. Etzkorn, C. P. Lutz, D. M. Eigler, and A. J. Heinrich, *Measurement of Fast Electron Spin Relaxation Times with Atomic Resolution*, Science **329**, 1628 (2010).

- 
- [62] F. Delgado and J. Fernandez-Rossier, *Spin dynamics of current-driven single magnetic adatoms and molecules*, Phys. Rev. B **82** (2010).
- [63] B. Bleaney and K. W. H. Stevens, *Paramagnetic resonance*, Rep. Prog. Phys. **16**, 108 (1953).
- [64] R. J. Elliott and K. W. H. Stevens, *The Theory of Magnetic Resonance Experiments on Salts of the Rare Earths*, Proc. Royal Soc. A **218**, 553 (1953).
- [65] R. Gross and A. Marx, *Festkörperphysik* (Oldenbourg Verlag, 2012).
- [66] C. Bresch, Master's thesis, Karlsruhe Institute of Technology (2013).
- [67] M. Hutchings, *Point-Charge Calculations of Energy Levels of Magnetic Ions in Crystalline Electric Fields*, Solid State Phys. **16**, 227 (1964).
- [68] T. Balashov, T. Miyamachi, T. Schuh, T. Märkl, C. Bresch, and W. Wulfhekel, *Dynamic magnetic excitations in 3d and 4f atoms and clusters*, Surf. Sci. **630**, 331 (2014).
- [69] F. Donati, A. Singha, S. Stepanow, C. Wäckerlin, J. Dreiser, P. Gambardella, S. Rusponi, and H. Brune, *Magnetism of Ho and Er Atoms on Close-Packed Metal Surfaces*, Phys. Rev. Lett. **113**, 237201 (2014).
- [70] R. Skomski and D. Sellmyer, *Anisotropy of rare-earth magnets*, J. Rare Earth **27**, 675 (2009).
- [71] B. Wybourne, *Spectroscopic properties of rare earths* (Wiley, 1965).

## References

---

- [72] C. Hübner, Ph.D. thesis, Universität Hamburg, Von-Melle-Park 3, 20146 Hamburg (2015).
- [73] S. Barnett, *Matrices: Methods and Applications* (Oxford University Press, 1990).
- [74] N. Vogt, J. H. Cole, M. Marthaler, and G. Schön, *Influence of two-level fluctuators on adiabatic passage techniques*, Phys. Rev. B **85**, 174515 (2012).
- [75] A. Donabidowicz-Kolkowska and C. Timm, *Spectroscopy of the transition-rate matrix for molecular junctions: dynamics in the Franck-Condon regime*, New J. Phys. **14**, 103050 (2012).
- [76] W. H. Zurek, *Quantum Darwinism, classical reality, and the randomness of quantum jumps*, Phys. Today **67**, 44 (2014).
- [77] J. Jin, M. Marthaler, and G. Schön, *Electroluminescence and multi-photon effects in a resonator driven by a tunnel junction*, Phys. Rev. B **91**, 085421 (2015).
- [78] J. Klein, A. Leger, M. Belin, and D. Defourneau, *Inelastic-Electron-Tunneling Spectroscopy of Metal-Insulator-Metal Junctions*, Phys. Rev. B **7**, 2336 (1973).
- [79] S. Al'tshuler and B. Kozyrev, *Electron Paramagnetic Resonance in Compounds of Transition Elements* (Wiley, 1974).
- [80] U. Fano, *Description of States in Quantum Mechanics by Density Matrix and Operator Techniques*, Rev. Mod. Phys. **29**, 74 (1957).
- [81] T. Brandes, *Coherent and collective quantum optical effects in mesoscopic systems*, Phys. Rep. **408**, 315 (2005).

- 
- [82] A. Megrant, C. Neill, R. Barends, B. Chiaro, Y. Chen, L. Feigl, J. Kelly, E. Lucero, M. Mariantoni, P. J. J. O'Malley, D. Sank, A. Vainsencher, J. Wenner, T. C. White, Y. Yin, J. Zhao, C. J. Palmstrøm, J. M. Martinis, and A. N. Cleland, *Planar superconducting resonators with internal quality factors above one million*, App. Phys. Lett. **100**, 113510 (2012).
- [83] T. Tawara, H. Kamada, Y.-H. Zhang, T. Tanabe, N. I. Cade, D. Ding, S. R. Johnson, H. Gotoh, E. Kuramochi, M. Notomi, and T. Sogawa, *Quality factor control and lasing characteristics of InAs/InGaAs quantum dots embedded in photonic-crystal nanocavities*, Opt. Exp. **16**, 5199 (2008).
- [84] S. Rojek, M. Governale, and J. König, *Spin pumping through quantum dots*, Physica Status Solidi B **251**, 1912 (2013).
- [85] D. DiVincenzo and D. Loss, *Rigorous Born approximation and beyond for the spin-boson model*, Phys. Rev. B **71**, 035318 (2005).
- [86] T. M. Stace, A. C. Doherty, and D. J. Reilly, *Dynamical Steady States in Driven Quantum Systems*, Phys. Rev. Lett. **111**, 180602 (2013).
- [87] A. Pomyalov, C. Meier, and D. Tannor, *The importance of initial correlations in rate dynamics: A consistent non-Markovian master equation approach*, Chem. Phys. **370**, 98 (2010).
- [88] A. Kofman and G. Kurizki, *Unified Theory of Dynamically Suppressed Qubit Decoherence in Thermal Baths*, Phys. Rev. Lett. **93**, 130406 (2004).
- [89] M. Thorwart, E. Paladino, and M. Grifoni, *Dynamics of the spin-boson model with a structured environment*, Chem. Phys. **296**, 333 (2004).

## References

---

- [90] P. P. Orth, A. Imambekov, and K. Le Hur, *Nonperturbative stochastic method for driven spin-boson model*, Phys. Rev. B **87**, 014305 (2013).
- [91] M. Merkli, G. P. Berman, and R. Sayre, *Electron transfer reactions: generalized spin-boson approach*, J. Math. Chem. **51**, 890 (2013).
- [92] A. Garg, J. N. Onuchic, and V. Ambegaokar, *Effect of friction on electron transfer in biomolecules*, J. Chem. Phys. **83**, 4491 (1985).
- [93] I. Wilson-Rae and A. Imamoglu, *Quantum Dot Cavity-QED in the Presence of Strong Electron-Phonon Interactions*, Phys. Rev. B **65**, 235311 (2002).
- [94] M. Marthaler, J. Leppäkangas, and J. Cole, *Circuit-QED analogue of a single-atom injection maser: Lasing, trapping states and multistability*, Phys. Rev. B **83** (2011).
- [95] O. Kashuba, D. M. Kennes, M. Pletyukhov, V. Meden, and H. Schoeller, *Quench dynamics of a dissipative quantum system: A renormalization group study*, Phys. Rev. B **88**, 165133 (2013).
- [96] G. Burkard, *Non-Markovian qubit dynamics in the presence of  $1/f$  noise*, Phys. Rev. B **79**, 125317 (2009).
- [97] F. Nesi, E. Paladino, M. Thorwart, and M. Grifoni, *Spin-boson dynamics beyond conventional perturbation theories*, Phys. Rev. B **76**, 155323 (2007).
- [98] H.-P. Breuer, E.-M. Laine, and J. Piilo, *Measure for the Degree of Non-Markovian Behavior of Quantum Processes in Open Systems*, Phys. Rev. Lett. **103**, 210401 (2009).

- 
- [99] J. Jin, X. Zheng, and Y. Yan, *Exact dynamics of dissipative electronic systems and quantum transport: Hierarchical equations of motion approach*, J. Chem. Phys. **129**, 184112 (2008).
- [100] K. D. Petersson, L. W. McFaul, M. D. Schroer, M. Jung, J. M. Taylor, A. A. Houck, and J. R. Petta, *Circuit quantum electrodynamics with a spin qubit*, Nature **490**, 380 (2012).
- [101] J. J. Viennot, M. C. Dartiailh, A. Cottet, and T. Kontos, *Coherent coupling of a single spin to microwave cavity photons*, Science **349**, 408 (2015).
- [102] J. Thingna, J.-S. Wang, and P. Hänggi, *Reduced density matrix for nonequilibrium steady states: A modified Redfield solution approach*, Phys. Rev. E **88**, 052127 (2013).
- [103] J.-S. Xu, C.-F. Li, C.-J. Zhang, X.-Y. Xu, Y.-S. Zhang, and G.-C. Guo, *Experimental investigation of the non-Markovian dynamics of classical and quantum correlations*, Phys. Rev. A **82**, 042328 (2010).
- [104] B.-H. Liu, L. Li, Y.-F. Huang, C.-F. Li, G.-C. Guo, E.-M. Laine, H.-P. Breuer, and J. Piilo, *Experimental control of the transition from Markovian to non-Markovian dynamics of open quantum systems*, Nature Phys. **7**, 931 (2011).
- [105] M. Hell, M. Wegewijs, and D. DiVincenzo, *Qubit quantum-dot sensors: noise cancellation by coherent backaction, initial slips, and elliptical precession*, Phys. Rev. B **93**, 045418 (2016).
- [106] H.-B. Chen, J.-Y. Lien, C.-C. Hwang, and Y.-N. Chen, *Long-lived quantum coherence and non-Markovianity of photosynthetic complexes*, Phys. Rev. E **89**, 042147 (2014).
- [107] S. Vinjanampathy and K. Modi, *Entropy bounds for quantum processes with initial correlations*, Phys. Rev. A **92** (2015).

## References

---

- [108] A. Smirne, H.-P. Breuer, J. Piilo, and B. Vacchini, *Initial correlations in open-systems dynamics: The Jaynes-Cummings model*, Phys. Rev. A **82**, 062114 (2010).
- [109] C. Navarrete-Benlloch, *Open systems dynamics: Simulating master equations in the computer*, ArXiv e-prints (2015).